

Reaction Selectivity Studies on Nanolithographically-Fabricated
Platinum Model Catalyst Arrays

by

Jeffrey Benjamin Grunes

B.S. (Trinity University) 2000

A dissertation submitted in partial satisfaction of the

requirements for the degree of

Doctor of Philosophy

in

Chemistry

in the

GRADUATE DIVISION

of the

UNIVERSITY OF CALIFORNIA, BERKELEY

Committee in charge:

Professor Gabor A. Somorjai (Chair)

Professor Norman E. Phillips

Professor David T. Attwood

Spring 2004

This dissertation of Jeffrey Benjamin Grunes is approved:

Chair

Date

Date

Date

University of California, Berkeley

Spring 2004

Reaction Selectivity Studies on Nanolithographically-Fabricated
Platinum Model Catalyst Arrays

Copyright (2004)

by

Jeffrey Benjamin Grunes

Abstract

Reaction Selectivity Studies on Nanolithographically-Fabricated
Platinum Model Catalyst Arrays

by

Jeffrey Benjamin Grunes

Doctor of Philosophy in Chemistry

University of California, Berkeley

Professor Gabor A. Somorjai (Chair)

In an effort to understand the molecular ingredients of catalytic activity and selectivity toward the end of tuning a catalyst for 100% selectivity, advanced nanolithography techniques were developed and utilized to fabricate well-ordered two-dimensional model catalyst arrays of metal nanostructures on an oxide support for the investigation of reaction selectivity. *In-situ* and *ex-situ* surface science techniques were coupled with catalytic reaction data to characterize the molecular structure of the catalyst systems and gain insight into hydrocarbon conversion in heterogeneous catalysis. Through systematic variation of catalyst parameters (size, spacing, structure, and oxide support) and catalytic reaction conditions (hydrocarbon chain length, temperature, pressures, and gas composition), the data presented in this dissertation demonstrate the ability to direct a reaction by rationally adjusting, through precise control, the design of the catalyst system.

Electron beam lithography (EBL) was employed to create platinum nanoparticles on an alumina (Al_2O_3) support. The Pt nanoparticle spacing (100-150-nm interparticle

distance) was varied in these samples, and they were characterized using x-ray photoelectron spectroscopy (XPS), transmission electron microscopy (TEM), scanning electron microscopy (SEM), and atomic force microscopy (AFM), both before and after reactions. The TEM studies showed the 28-nm Pt nanoparticles with 100 and 150-nm interparticle spacing on alumina to be polycrystalline in nature, with crystalline sizes of 3-5 nm. The nanoparticle crystallites increased significantly after heat treatment. The nanoparticles were still mostly polycrystalline in nature, with 2-3 domains. The 28-nm Pt nanoparticles deposited on alumina were removed by the AFM tip in contact mode with a normal force of approximately 30 nN. After heat treatment at 500°C in vacuum for 3 hours, the AFM tip, even at 4000 nN, could not remove the platinum nanoparticles. The increase of adhesion upon heat treatment indicates stronger bonding between the Pt and the support at the metal-oxide interface.

A novel cleaning procedure that was safe and reproducible to the oxide-supported nanoparticle array was developed for cleaning the catalyst surface. The cleaning procedure involved using low dosages of the strong oxidizer NO₂ (1×10^{-6} Torr), which left molecular oxygen on the surface. This contaminant was removed by dosing 10 L of CO in order to produce CO₂, which was removed by flashing the temperature above the desorption temperature of CO. This cleaning procedure was necessary for catalyst activation before running reactions on the catalyst system. This method proved an ideal alternative to ion sputtering, which served to damage the Pt nanoparticles and induce Pt-silicide formation.

Kinetic studies of ethylene hydrogenation were performed on the Pt nanoparticle arrays and compared with kinetic data from a Pt(111) single crystal. The reaction was

carried out in UHV chamber (10^{-10} Torr), coupled with a high-pressure reaction cell (1 atm). The reaction rate was monitored via gas chromatography with a flame ionization detector. The reactivity of the Pt/Al₂O₃ arrays was compared to a Pt(111) single crystal for the structure-insensitive ethylene hydrogenation reaction. The apparent activation energy and the pressure dependence of the H₂ and C₂H₄ on the nanoparticle array were in excellent agreement with the kinetic data on the Pt(111) single crystal model catalyst. The calculated turnover frequency based on a rate equation for a Pt(111) single crystal led to a calculated active metal surface area that compared very well with an active metal surface area estimated from sample geometry. It was determined that this reaction can be used to determine the active metal surface area of the Pt nanoparticle array model catalysts. Similar results were obtained for Pt nanoparticle arrays with different interparticle spacing (100 vs. 150-nm spacing).

A typical catalyst poison, CO, was then introduced into the reaction gas mixture. Gas chromatography (GC) results for Pt(111) show that CO adsorption reduces the turnover rate from 10^1 to 10^{-2} molecules/Pt atom/s at 413 K, and the activation energy for hydrogenation on the poisoned surface becomes (20.2 ± 0.1) kcal/mol. The activation energy for ethylene hydrogenation over Pt(111) in the absence of CO is 10.8 kcal/mol. The poisoning effect of CO on ethylene hydrogenation on the Pt(111) surface was also studied by sum frequency generation vibrational spectroscopy (SFG). It was found that a monolayer of CO prevented the adsorption of ethylene on the Pt(111) surface in the presence of high-pressure ethylene (up to 35 Torr). In contrast, CO can adsorb on the ethylene-pretreated Pt(111) surface with increasing the CO pressure (10^{-7} -400 Torr). However, the co-adsorbed ethylidyne molecules weakened CO bonding, which was

evidenced by the red shift in the vibrational frequency. In the presence of high-pressure CO (> 0.1 Torr), the catalytic ethylene hydrogenation was poisoned due to the site blocking effects of CO adsorption. No catalytic reactivity was observed at temperatures lower than the CO desorption temperature (400 K). The measured apparent activation energy of the CO-poisoned ethylene hydrogenation reaction was 20.5 kcal/mol. The Pt nanoparticle system shows the same rate for the reaction as over Pt(111) in the absence of CO. When CO is adsorbed on the Pt nanoparticle array, the rate of the reaction is reduced from 10^2 to 10^1 molecules/Pt atom/s at 413 K. However, the activation energy remains largely unchanged. The Pt nanoparticles show an apparent activation energy for ethylene hydrogenation of (10.2 ± 0.2) kcal/mol in the absence of CO and (11.4 ± 0.6) kcal/mol on the CO-poisoned nanoparticle array. It is proposed that the active sites at the oxide-metal interface are responsible for the difference in activation energies for the hydrogenation reaction over the two model platinum catalysts.

Due to the high cost and low throughput (mm^2) of electron beam lithography, as it is a serial process, another fabrication technique was developed to produce a 2nd generation model catalyst system. Size reduction lithography (SRL) is a new photolithographic process whereby through sacrificial layer depositions and selective etching, wafer-scale silicon nanowire molds with 7-nm features can be produced. When coupled with nanoimprint lithography (NIL), a polymer stamping technology, the pattern is transferred into an oxide-coated (silica or alumina) Si(100) wafer that will ultimately become Pt nanowire or nanodot model catalyst arrays. This low-cost, high-throughput parallel process yields the necessary metal surface area (cm^2) to study those industrially

significant reactions that have low turnover ($\leq 10^{-2} \text{ s}^{-1}$). The SRL and NIL processes, along with the final catalyst system was characterized via SEM, XPS, and AFM.

As a test reaction, ethylene hydrogenation was catalyzed over the alumina-supported Pt nanowires. The Pt nanowire sample had a measured activation energy of $(13.6 \pm 0.2) \text{ kcal/mol}$. The Pt nanowire showed the production of methane in addition to ethane, even at low temperatures. The results indicate the presence of carbon fragments on the surface that hydrogenate to methane by secondary reactions. The presence of carbon blocks sites and restricts mobility; therefore, increasing the activation energy for ethylene to hydrogenate on the nanowire catalyst surface. Similar results were seen with Pt nanowires on a silica support as well as nanowires with different diameters (25 and 64-nm linewidths).

The poisoned reaction showed a distinct difference between the model catalyst systems. While the Pt(111) single crystal and Pt nanowires had measured activation energies around 20 kcal/mol—typical value for the desorption energy of CO—the Pt nanoparticles did not show a doubling of the activation energy. While the rate was dramatically decreased, the energy barrier indicates that some sites remain active for the reaction. The key factor appears to be the ratio of metal sites to oxide-metal interface sites. By controlling this ratio, which is accomplished during the fabrication process, a catalyst can be tuned for a reaction.

Professor Gabor A. Somorjai
Dissertation Committee Chair

Table of Contents

Acknowledgments.....	vi
Chapter 1: Introduction.....	1
Chapter 2: Experimental Techniques	
2.1 Characterization Techniques: Ultrahigh Vacuum and Surface Science Tools	10
2.1.1 Auger Electron Spectroscopy (AES).....	14
2.1.2 X-Ray Photoelectron Spectroscopy (XPS).....	16
2.2 Characterization Techniques: Surface Science Microscopy and Spectroscopy Tools.....	20
2.2.1 Atomic Force Microscopy (AFM).....	20
2.2.2 Scanning Electron Microscopy (SEM).....	24
2.2.3 Transmission Electron Microscopy (TEM).....	27
2.2.4 Sum Frequency Generation Vibrational Spectroscopy (SFG).....	28
2.3 Fabrication Techniques.....	31
2.3.1 Electron Beam Lithography (EBL).....	34
2.3.2 Size Reduction Lithography (SRL).....	38
2.3.3 Nanoimprint Lithography (NIL).....	41
Chapter 3: Atomic Force Microscopy (AFM) and Transmission Electron Microscopy (TEM) Studies of Alumina-Supported Pt Nanoparticle Array Model Catalysts Prepared by Electron Beam Lithography	
3.1 Introduction.....	68
3.2 Experimental	71

3.2.1 Electron Beam Lithography (EBL).....	71
3.2.2 Transmission Electron Microscopy (TEM).....	72
3.2.3 Atomic Force Microscopy (AFM).....	73
3.3 Results and Discussion.....	73
3.3.1 Characterization.....	73
3.3.2 Adhesion.....	74
3.4 Conclusion.....	77
Chapter 4: Ethylene Hydrogenation over Platinum Nanoparticle Array	
Model Catalysts Fabricated by Electron Beam Lithography:	
Determination of Active Metal Surface Area	
4.1 Introduction.....	86
4.2 Experimental	88
4.2.1 Fabrication and Characterization.....	88
4.2.2 NO ₂ Cleaning.....	88
4.2.3 UHV Chamber with High-Pressure Reaction Cell.....	89
4.3 Results and Discussion.....	90
4.3.1 Characterization of the Pt Nanoparticle Arrays.....	90
4.3.2 Ethylene Hydrogenation Reaction Rate Studies.....	91
4.3.3 Active Metal Surface Area Determination.....	92
4.4 Conclusion	94

Chapter 5: CO Poisoning of Ethylene Hydrogenation over Pt Catalysts:

A Comparison of Pt(111) Single Crystal and Pt Nanoparticle

Activities

5.1 Introduction.....	105
5.2 Experimental.....	106
5.2.1 Pt(111) Single Crystal Model Catalysts: Characterization and Reaction Rate Studies.....	106
5.2.2 Pt Nanoparticles on Alumina: Fabrication, Characterization, and Reaction Rate Studies.....	107
5.3 Results and Discussion.....	108
5.3.1 CO-Poisoned Ethylene Hydrogenation Reaction Rate Studies on Pt(111): Effects of Temperature.....	108
5.3.2 CO-Poisoned Ethylene Hydrogenation Reaction Rate Studies on Pt Nanoparticles Supported on Alumina: Effects of Temperature.....	109
5.3.3 CO-Poisoned Ethylene Hydrogenation Reaction Rate Studies on Pt Nanoparticles Supported on Alumina: Effects of Pressure.....	112
5.4 Conclusion.....	112

Chapter 6: CO Poisoning of Catalytic Ethylene Hydrogenation on the

Pt(111) Surface and CO Adsorption on Platinum Nanoparticle

Arrays Studied by Sum Frequency Generation Vibration

Spectroscopy (SFG)

6.1 Introduction.....	119
6.2 Experimental.....	123
6.2.1 SFG Configuration for Pt(111) and Pt Nanoparticles.....	123
6.2.2 Alumina-Supported Pt Nanoparticle Arrays Fabricated by Electron Beam Lithography (EBL).....	124
6.3 Results and Discussion.....	124
6.3.1 CO/Ethylene Co-Adsorption Study on Pt(111).....	124
6.3.2 CO-Poisoning of Ethylene Hydrogenation on the Pt(111) Surface.....	131
6.3.3 CO on Pt Nanoparticles.....	132
6.4 Conclusion.....	134
Chapter 7: Ethylene Hydrogenation and CO-Poisoned Ethylene Hydrogenation on Alumina-Supported Pt Nanowire Array Model Catalysts Fabricated by Size Reduction Lithography and Nanoimprint Lithography	
7.1 Introduction.....	149
7.2 Experimental.....	152
7.2.1 Size Reduction Lithography (SRL).....	152
7.2.2 Nanoimprint Lithography (NIL).....	155
7.2.3 Reaction Rate Studies for Poisoned and Unpoisoned Ethylene Hydrogenation over Alumina-Supported Pt Nanowires.....	159
7.3 Results and Discussion.....	160
7.3.1 Characterization of Alumina-Supported Pt Nanowires	

Fabricated by SRL and NIL.....	160
7.3.2 Reaction Rate Studies for Poisoned and Unpoisoned	
Ethylene Hydrogenation on the Alumina-Supported	
Pt Nanowires.....	160
7.4 Conclusion.....	164

Acknowledgments

I remember that the decision to come to graduate school four years ago was not a black and white issue with me. I told myself to complete the necessary forms and apply to a list of schools and then wait for a response, as perhaps a school's interest in me would help me establish my interest in graduate school. When the responses were favorable, I decided to take the chance. I packed up my New Orleans Saints gear, loaded up the '72 Mustang convertible, said goodbye to the land of crawfish pie, and headed West to sunny California (a description that I quickly learned did not always apply to the Bay Area). In the summer of 2000, I embarked on my graduate career. As I rest on the edge of the summer of 2004 and look back at my time at Cal and in Berkeley, I now see that I gained much more than a Ph.D. in chemistry.

First and foremost, I would like to thank Prof. Gabor Somorjai. He gave me the creative freedom to approach science on my own terms. His enthusiasm and passion for chemistry are unmatched, and one can't help but get excited in return. His daring leaps into brand new areas taught me that it is easy to stay in one's comfort zone, but much more rewarding to take on and overcome a seemingly impossible challenge. It is because of this that I found myself breaking the traditional boundaries of physical chemistry in order to address fundamental science issues. Even though he is a 49'ers fan, I am eternally thankful for the opportunity he provided me and the wisdom he imparted to me.

I must also acknowledge the many postdocs and graduate students within the Somorjai group whom I interacted with during my career. In particular, I want to thank Dr. Ji Zhu, who was my mentor and teacher on the "nano" side of the group. I could not have reached this point in my graduate studies without his influence. I must give

recognition to Anthony Contreras who will continue, expand, and create new projects with nanocatalysts. I hope that whatever help I gave you that you will one day give to someone else. Your science and dedication are strong, your foosball game is weak, but most importantly, you are a good person. Alongside Anthony, I have also worked with Dr. Xiaoming Yan. He will undoubtedly bring an expertise to the projects that will aid the success of present and future ventures. I thank the entire Somorjai group for the science support inside the lab as well as the non-science support outside of lab. I have been fortunate to have some collaborative projects, for which I thank the following people for their time, scientific discussions, and patience: Prof. Jeff Bokor, Dr. Yang-Kyu Choi, Dr. Alex Liddle, Dr. Jeff Beeman, Dr. Frank Ogletree, and Dr. Eric Anderson. I am indebted to the hard-working staff and users of the Microfabrication Laboratory on campus and the National Center for Electron Microscopy at LBNL. I could not do my research from day to day without the efforts of the machine, electronics, pump, and other facilities shops at UC Berkeley and LBNL. I am grateful to the many administrative assistants on campus and up on the hill, with special thanks to Inger Coble who made my life as a graduate student researcher as unoffending as possible. Whether I need to buy a piece of equipment or hear a good story, she has always provided me with both.

I must also say something of the amazing group of people I met here at Cal whom I am proud to call my friends. At the very least I must say thank you to Harsha Vaswani, who started as a friend, and I'm happy and lucky to say, became more than a friend. I don't know what I would have done without you while I was here, and I'm glad I didn't have to figure that out. Don't lose your way in a year when it is time to move. Telly Koffas is a good friend who I saw in my circle of friends as well as the Somorjai group.

Every time I needed someone to listen to my rants about the group, the school, sports, politics, or anything else, he was always there. Last one to Portland has to buy the Guinness. It will be hard to leave the others in my close circle of friends: Tony Dutoi, Matt Nee, Kim Pierce, and Alex Sodt. You all mean something special and different to me. Don't forget to go toward the pansy-colored neon lights of the Hotsy Totsy every so often. All of you are friends that come once in a lifetime, and I don't think distance will ever change that.

There is also the support of friends and family who do not call California home. To my friends from Shreveport: Drew, Hoss, Roche, and Saye—time marches on and lives continue to change, but we're always there for each other. This will never change. To my Phat House residents and honorary residents: Haagis, Hummel, Lauren, and Niko—could there possibly be a more different group of people who get along so well? We're all going after what we want, and I know we will all get there. Continued success to everyone. To Orange and her family, I say a heart-felt thank you. You all became my new family in every sense of the word. May you all have health and happiness. To my mother, father, brother, and grandfather, whom I don't see or talk with as much as I probably should, I just say thank you. I appreciate the fact that good or bad, right or wrong, family is family. You have not always understood the decisions I have made in life or even what exactly it is I do, but you never let that affect your undying support. Good thing, because now comes the chemistry.....

Chapter 1

Introduction

Heterogeneous catalysts continue to be our most useful agents of chemical change and the workhorse of the modern chemical industry. Heterogeneous catalysts with increased activities and selectivities are in demand in areas critical to energy conversion, commodity production (petroleum, plastics, pharmaceuticals, chemicals), and green chemical synthesis processes that are driven by the sense of pollution prevention and abatement as well as waste management. The focus of the catalysis community has changed with time—catalysts with higher activities in the 20th Century and catalysts with higher selectivities in the 21st Century—but the overall goal of understanding the fundamental mechanisms of catalysts and catalytic reactions at the molecular level has remained constant. By elucidating the molecular ingredients of catalysis and systematic investigations of reactions, we can rationally

tune the properties of a catalyst to yield the desired activity and selectivity that would benefit both the economy and the environment.

As the 21st century begins, the challenge of catalytic scientists, both academic and industrial, is to develop a catalyst that is capable of 100% selectivity for the desired product.¹ At the end of the 20th century, our understanding of the molecular details of a catalyst that control activity was well developed. Understanding the catalyst features, which are intrinsically molecular in nature, that control selectivity is an extremely difficult endeavor. Like activity, selectivity is a kinetic consequence that is determined by the difference in the free energy barriers of the two competing reactions.² The relative heights of these barriers, the parameter that determines catalytic activity, can be altered by changing properties of the catalyst, which in turn can influence selectivity if one barrier is altered more than the other is. There are only two multi-path catalytic reactions studied by catalysis science using the surface science approach to explore selectivity. These are CO hydrogenation³ and the conversion of *n*-hexane or *n*-heptane to branched isomers, aromatics, and other products (reforming).⁴

Catalysts are usually highly dispersed metal nanoparticles on a high surface area support (oxides, zeolites, etc.), with particle size varying between 1-100 nm. Modern surface science studies indicate that, during chemisorption and catalytic reactions, these particles restructure, and the adsorbed molecules also possess a high degree of surface mobility. The adsorbate-induced restructuring facilitates the breaking of surface chemical bonds and the rearrangement of adsorbates as the cluster assumes a thermodynamically most-stable configuration. The exothermic heat of chemisorption offsets the energy expenditure involved in weakening metal-metal bonds as the particles

restructure. Since the atoms in the nanoparticles have low coordination, such adsorbate-induced restructuring is facile.

For typical catalysts, the metal particles are introduced to the support from solution by methods such as impregnation, adsorption, ion-exchange, and co-precipitation.⁵ These techniques give an intricate network of randomly distributed nanoparticles inside the pores of the support. To get a molecular understanding of this intricate network and elucidate the underlying kinetic processes they achieve, great care must be given to understand the identifiable features that influence both catalyst activity and selectivity. There are six known molecular ingredients of catalyst activity and selectivity. These are 1) metal surface structure^{6, 7, 8, 9} and particle size¹⁰; 2) bonding modifier additives¹¹; 3) mobility of the metal clusters to restructure as well as the mobility of adsorbates on these clusters^{12, 13, 14, 15, 16}; 4) selective site-blocking^{17, 18, 19, 20, 21}; 5) bifunctional catalysis (oxide support)^{22, 23, 24, 25}; and 6) metal-oxide interface sites and interactions.^{26, 27, 28, 29}

To probe the properties of catalytic behavior, academic science has made use of single crystalline metals as a model system. Single crystals have inherent properties that make them a perfect fit for surface science and catalysis. The single crystal is flat, conducting, and are structurally well defined. Because of these attributes, surface science can employ its electron and photon to characterize the surface of the catalyst. Single crystals are easy to clean and maintain in ultra-high vacuum, as defined by Auger electron spectroscopy. The single crystal is thermodynamically stable in reducing and oxidizing environments, and it can sustain repeated cycles of sputtering and annealing in ultra-high vacuum without losing structural integrity. The single crystal also provides the

necessary active metal surface area ($\sim\text{cm}^2$) to study all industrially significant catalytic reactions, from the most facile turnover reactions ($> 10^{-2} \text{ s}^{-1}$) to the most complicated and demanding reaction with low turnover ($\leq 10^{-2} \text{ s}^{-1}$). The extensive data that has been collected since the 1970's on single crystalline metals has built the foundation of surface science and catalysis. The insight gained into the molecular ingredients of catalytic activity and selectivity mentioned earlier is the result of decades of studies performed on single crystals.

As a model catalyst system, however, single crystals do not truly mirror the typical industrial catalyst. This system lacks features such as metal nanoparticles and the presence of an oxide support, both of which are important components of catalytic activity and selectivity. The single crystal cannot exhibit the changes of electronic structure and quantum effects associated with a metal nanoparticle with a diameter of less than 2 nm.³⁰ The need to develop a new 2-dimensional model catalyst system that retains the advantages of the single crystalline metal and yet better resembles the industrial catalyst is a present aim of academic research. The geometry of the 2-D system is to incorporate the tools of surface science in an effort to understand the heterogeneous catalytic process.³¹ Nanoparticle systems have been fabricated via laser ablation³², calcination of metal salts on an oxide³³, evaporation of metal onto an oxide^{34, 35, 36}, soft landing of size-selected clusters on a planar support^{37, 38}, laser interference nanolithography³⁹, photolithography⁴⁰, colloidal lithography⁴¹, and decomposition of metal carbonyls⁴², to name a few. Each family of techniques has its own limitations. The lithography methods previously utilized could not achieve the necessary size regime for nanoparticles. The non-lithographic techniques cannot precisely control the structure of

the model catalyst nor independently alter the other variables of the system. Classical methods, such as incipient wetness and ion exchange, lack the control necessary to develop a catalyst capable of 100% selectivity. The particles produced from these methods have broad particle size distributions (1-20 nm), are not positionally controlled within the support architecture, and cannot be systematically and easily varied. Perfect reaction selectivity requires careful catalyst design, where the influence of a number of parameters can be rationally tuned and studied systematically.

In order to obtain high selectivity toward the ultimate goal of 100% selectivity, which is a road map for obtaining selective and green catalysts for chemical processes, one has to assert molecular control over the size, location, structure, and promoters of the catalysts. The work presented in this dissertation is an attempt to address these issues through advanced lithography techniques. Chapter 2 will detail the chamber where surface science and catalytic studies were performed. Chapter 2 will also outline the various characterization and fabrication techniques. Adhesion studies on Pt/Al₂O₃ nanoparticle arrays fabricated by EBL are presented in Chapter 3. The results of ethylene hydrogenation over the alumina-supported Pt nanoparticles are discussed in Chapter 4. Also included in Chapter 4 will be a description of the novel cleaning method developed specifically for the Pt nanoparticles. Chapter 5 will show the results of CO-poisoned ethylene hydrogenation on the Pt nanoparticle model catalyst array supported on alumina. Chapter 6 will present CO-poisoned ethylene hydrogenation data as well as CO adsorption and CO/ethylene co-adsorption on two model catalyst systems (Pt single crystal and Pt nanoparticles) as probed by sum frequency generation vibrational

spectroscopy. Chapter 7 will report the results of poisoned and unpoisoned ethylene hydrogenation over the Pt nanowires on alumina that were fabricated with SRL and NIL.

References

-
- ¹ (workshop), *Catal. Lett.* **2001**, 76, 111.
- ² Zaera, F., *J. Phys. Chem. B.* **2002**, 106, 4043.
- ³ Borodko, Y.; Somorjai, G.A., *Appl. Catal. A-Gen.* **1999**, 186, 355.
- ⁴ Ramos, A.L.D.; Kim, S.H.; Chen, P.L.; Song, J.H.; Somorjai, G.A., *Catal. Lett.* **2000**, 66, 5.
- ⁵ Anderson, J.R. *Structure of Metallic Catalysts*. Academic Press, London, 1975.
- ⁶ Bernasek, S.L.; Somorjai, G.A., *J. Chem. Phys.* **1975**, 62, 3149.
- ⁷ Spencer, N.D.; Schoonmaker, R.C.; Somorjai, G.A., *J. Catal.* **1982**, 74, 129.
- ⁸ Boudart, M., *J. Mol. Catal.* **1985**, 30, 27.
- ⁹ Dumesic, J. A.; Topsoe, H.; Kammouma, S.; Boudart, M., *J. Catal.* **1975**, 37, 503.
- ¹⁰ Bond, G.C. *Surf. Sci.* **1985**, 156, 966.
- ¹¹ Strongin, D.R.; Somorjai, G.A., *J. Catal.* **1988**, 109, 51.
- ¹² Cremer, P.S.; Somorjai, G.A., *J. Chem. Soc.-Far. Trans.* **1995**, 91, 3671.
- ¹³ Hwang, K. S.; Yang, M. C.; Zhu, J.; Grunes, J.; Somorjai, G. A., *J. Mol. Catal. A Chem.* **2003**, 204, 499.
- ¹⁴ Somorjai, G. A. *Introduction to Surface Chemistry and Catalysis*. John Wiley & Sons Inc., New York, 1994.
- ¹⁵ Starke, U.; Barbieri, A.; Materer, N.; Van Hove, M.A.; Somorjai, G.A., *Surf. Sci.* **1993**, 286, 1.
- ¹⁶ Cremer, P.S.; Su, X.C.; Shen, Y.R.; Somorjai, G.A., *J. Am. Chem. Soc.* **1996**, 118, 2942.
- ¹⁷ Herz, R. K.; Gilliespie, W. D.; Petersen, E. E.; Somorjai, G. A., *J. Catal.* **1981**, 67,

371.

- ¹⁸ Zaera, F.; Somorjai, G. A., *Langmuir* **1986**, 2, 686.
- ¹⁹ Hagen, J. *Industrial Catalysis: A Practical Approach*. Wiley VCH, New York, 1999.
- ²⁰ Weisz, P. B., *Pure Appl. Chem.* **1980**, 52, 2091.
- ²¹ Frillette, V.J.; Weisz, P.B.; Golden, R.L., *J. Catal.* **1962**, 1, 301.
- ²² Taylor, W.F.; Yates, D.J.C.; Sinfelt, J.H., *J. Phys. Chem.* **1964**, 68, 2962.
- ²³ Boudart, M.; Djéga-Mariadassou, G. *Kinetics of Heterogeneous Catalytic Reactions*. Princeton University Press, Princeton, NJ, 1984.
- ²⁴ Vera, C.R.; Pieck, C.L.; Shimizu, K.; Yori, J.C.; Parera, J.M., *Appl. Catal. A-Gen.* **2002**, 232, 169.
- ²⁵ Tanabe, K.; Holderich, W.F., *Appl. Catal. A-Gen.* **1999**, 181, 399.
- ²⁶ Pajonk, G.M., *Appl. Catal.* **2000**, 202, 157.
- ²⁷ Boffa, A.; Lin, C.; Bell, A.T.; Somorjai, G.A., *J. Catal.* **1994**, 149, 149.
- ²⁸ Bartholomew, C.H.; Pannell, R.B.; Butler, J.L., *J. Catal.* **1980**, 65, 335.
- ²⁹ Vannice, M. A., *Top. Catal.* **1997**, 4, 241.
- ³⁰ Kubo, R. *J. Phys. Soc. Japan* **1962**, 17, 975.
- ³¹ Gates, B.C. *Topics Catal.* **2001**, 14, 173.
- ³² Paszti, Z.; Peto, G.; Horvath, Z.E.; Karacs, A.; Guczi, L., *J. Phys. Chem. B*, **1997**, 101, 2109.
- ³³ Van Hardeveld, R.M.; Gunter, P.L.J.; Van Uzendoorn, L.J.; Wieldraaijer, W.; Kuipers, E.W.; Niemantsverdriet, J.W., *Appl. Surf. Sci.* **1995**, 84, 339.
- ³⁴ Lai, X.; St. Clair, T.P.; Valden M.; Goodman, D.W., *Prog. Surf. Sci.* **1998**, 59, 25.
- ³⁵ Hoffmann, J.; Schauermaun, S.; Hartmann, J.; Zhdanov, V.P.; Kasemo, B.; Libuda, J.;

-
- Freund, H.-J., *Chem. Phys. Lett.* **2002**, *354*, 403.
- ³⁶ Libuda, J.; Freund, H.-J., *J. Phys. Chem. B* **2002**, *106*, 4901.
- ³⁷ Heiz, U.; Sanchez, A.; Abbet, S.; Schneider, W.D., *J. Am. Chem. Soc.* **1999**, *121*, 3214.
- ³⁸ Roy, H.V.; Fayet, P.; Patthey, F.; Schneider, W.D.; Delly, B.; Massobrio, C., *Phys. Rev. B* **1994**, *49*, 5611.
- ³⁹ Schildenberger, M.; Bonetti, Y.; Aeschlimann, M.; Scandella, L.; Gobrecht, J.; Prins, R., *Catal. Lett.* **1998**, *56*, 1.
- ⁴⁰ Krauth, A.C.; Lee, K.H.; Bernstein, G.H.; Wolf, E.E., *Catal. Lett.* **1994**, *27*, 43.
- ⁴¹ Werdinius, C.; Osterlund, L.; Kasemo, B., *Langmuir* **2003**, *19*, 458.
- ⁴² Argo, A.M.; Odzak, J.; Lai, F.S.; Gates, B.C., *Nature* **2002**, *415*, 623.

Chapter 2

Experimental Techniques

2.1 Characterization Techniques: Ultrahigh Vacuum and Surface

Science Tools

Ultrahigh vacuum (UHV) is generally defined to be a pressure of 10^{-8} Torr or less.^{1, 2, 3, 4, 5} Surface science has the daunting task of distinguishing the surface (10^{15} atoms/cm²) from the bulk (10^{23} atoms/cm³), with surface sensitivity being defined as less than 1% of a monolayer (10^{13} atoms/cm²) over an area less than 1 mm². Modern surface science techniques are dependent on UHV for two main reasons. First, most techniques

monitor the interaction (diffraction, scattering, and/or emission) between incident electrons of low energy (20-1000 eV) and surface atoms in order to determine surface composition, structure, and oxidation state. These electrons are surface sensitive, as they strongly interact with metal atoms and are able to escape from only the first few atomic layers near the surface, based on the mean free path of electrons in solids.⁶ The background pressure must be low enough so that a significant fraction of the charged particles are not altered by collisions with gas phase molecules while traveling to or from the surface. The mean free path of an electron (λ) in vacuum is estimated as:

$$\lambda = \frac{k_b T}{2^{1/2} P d^2 \pi}$$

where λ is the mean free path in Å, k_b is Boltzmann's constant in J/K, T is the temperature in Kelvin, P is the pressure in Torr, and d is the diameter of the molecule in Å that composes the residue gas in the vacuum. The dependence of electron inelastic mean free path as a function of kinetic energy is defined as the universal curve. The broad minimum in mean free path from 4-20 Å occurs in the 10-500 eV energy range and is the basis for most surface science characterization techniques (Figure 2.1). Secondly, there is a stringent requirement to minimize contamination of the surface of the sample during the course of an experiment. It is desirable to prepare and maintain an atomically clean surface. The surface of a sample is quickly covered in a thick layer of carbonaceous deposit from the hydrocarbons contained in the atmosphere. The surface can also become contaminated from bulk impurities diffusing to the surface during heat treatments. It is possible to clean the surface of contaminants via chemical reaction and physical ion sputtering. But these clean metal surfaces are extremely reactive with oxygen and carbon-containing compounds (atmosphere). Therefore it is crucial to do

such cleaning procedures in UHV. Using the kinetic theory of gases, one can calculate the time needed for a surface to adsorb one monolayer of gas.⁷ The flux (F) of molecules striking the surface of unit area at a given ambient pressure (P) is:

$$F = 3.51 \times 10^{22} P / \sqrt{MT}$$

where P is in Torr, M is the average molar weight of the gas in g/mol and T is the temperature in Kelvin. This yields a flux in atoms/cm²·s. Assuming unity for the sticking coefficient, this establishes the unit of monolayer coverage of the Langmuir (L): 1 L = 10⁻⁶ Torr·s.

Monolayer adsorption time increases dramatically with decreasing pressure. In order to maintain an atomically clean surface over the timescale of an experiment (10³-10⁴ s), a chamber pressure of 10⁻⁹ to 10⁻¹⁰ Torr must be available.

To achieve this base pressure, the studies reported in this dissertation were performed in a stainless steel UHV chamber that was coupled with a high-pressure reaction cell (HPRC). THE HPRC consisted of a stainless steel hollow tube that is part of a standard bellows that can be hydraulically raised to form a metal gasket seal with the top portion of the HPRC. The clearance of the tube just allows for the heater and sample assembly to fit inside the HPRC, thus minimizing the volume of the reaction loop. The HPRC can be pressurized to ~2500 psi. The UHV chamber achieved a base pressure of 5×10⁻¹⁰ Torr and a working pressure of 1×10⁻⁹ Torr; the HPRC could be sealed off from the outer UHV chamber and flow ~1 atm of reaction gases. The base pressure was achieved through use of mechanical pumps, a 330 Liter/s turbomolecular pump (Balzers TPU 330), and a 400 L/s ion pump (Varian) (Figure 2.2). The sample was attached to a gold-plated rotatable manipulator; it was Au-coated to reduce charging effects and

eliminate background reactions. The samples were heated through use of a boraelectric ceramic heater (Advanced Ceramics, HT-01), attached with tantalum clips (Figure 2.3). The temperature was measured at the surface of the catalyst with 0.010-inch diameter chromel/alumel thermocouple wire, which was clamped between the Ta clip and the sample. Alumina spacers were added to avoid electrical contact between the thermocouple wire and the heater. The chamber was equipped with a double-pass cylindrical mirror analyzer (Physical Electronics, 15-255G) for AES, a mass spectrometer (UTI 100C) for temperature programmed desorption (TPD) and analyzing gas mixtures in the chamber, and an ion gun (Physical Electronics, 20-045) for sputtering clean single crystalline metals. Cleaning gases were controllably introduced into the main UHV chamber through leak valves. Reaction gases are pre-mixed in a gas manifold (275 mL) before being introduced into the HPRC. The reaction loop is 209 mL, and gases are circulated at a rate of 13 mL/min via a recirculation pump (Metal Bellows Division, Senior Flexonics). Gases are sent to a gas chromatograph (Hewlett-Packard, 5890 Series II) equipped with a 6-way valve for sampling in a batch reactor mode of operation. The gases are analyzed by a flame ionization detector and a capillary column (J&W Scientific, alumina 30 m \times 0.530 mm).

The next few sections will outline the two main UHV surface-sensitive techniques utilized for the work contained in this dissertation: Auger electron spectroscopy (AES) and x-ray photoelectron spectroscopy (XPS).

2.1.1 Auger Electron Spectroscopy (AES)

Auger electron spectroscopy (AES) yields surface compositional information by utilizing the principle that all atoms, except H and He, eject Auger electrons with specific kinetic energies that can be related to the identity of the atom based on the energy levels of the atom and its ionized states.^{8, 9, 10, 11, 12, 13, 14} Auger transitions are autoionization processes that come about due to the electrostatic interaction between two electrons in an atom after the creation of a hole (ionized atom). An outer shell electron relaxes to fill the core level (inner shell) vacancy, transferring its energy to a secondary electron (Auger electron) that is then ejected (Figure 2.4). The ejected electron has a characteristic kinetic energy specific to an element that can be calculated from the equation:

$$E_{ijk}(z) = E_i(z) - E_j(z) - E_k(z - \Delta) - e \bullet \Phi_{sp}$$

where i, j, and k represent the electronic energy levels involved in the process, z is the atomic number of the atom, Δ is the effective charge after the initial ionization, and Φ_{sp} is the work function of the spectrometer referred to vacuum. $E_k(z - \Delta)$ also includes a correction due to electronic relaxation of the environment surrounding the ionized atom. The kinetic energy of the Auger electron is independent of the excitation method of the ion. This is mainly an issue of time, as the initial ionization process occurs in less than 10^{-16} s, whereas the lifetime of the excited state ion is typically an order of magnitude longer. With a kinetic energy of 0-1000 eV for the Auger electron, their mean free path in a solid is on the order of 3-10 Å. From the raw data that records electron current vs. kinetic energy, it is better to differentiate $N(E)$ vs. E to distinguish the small Auger electron signal from the large and slow-varying background of secondary electrons. The intensity of the Auger electron current (i_A) can be expressed as¹⁵:

$$i_A = i_p(1 + R)QY \int_0^{\infty} n(z) e^{-z/\lambda \cos \theta} dz$$

where i_A is the Auger electron current, i_p is the primary electron current, R is the backscattering factor, Q is the ionization probability, Y is the probability of Auger decay (vs. X-ray fluorescence), $n(z)$ is the concentration of the element at depth z , λ is the inelastic mean free path of the Auger electron, and θ is the take-off angle of the Auger electron measured from the surface normal. For a homogeneous sample with the detector perpendicular to the sample surface, the formula simplifies to:

$$i_A = i_p(1 + R)QY\lambda n(z)$$

While most Auger spectra were used qualitatively to monitor the cleanliness of the sample surface, quantitative analysis of Auger spectra is possible. The calculation is more complicated because R and λ are sample specific and thus difficult to obtain. Calibration of the Auger signal against independent techniques—low energy electron diffraction (LEED), microbalances, radioactive tracers, evaporation of films of known thickness, and ellipsometry—are routinely used to obtain quantitative information. Since the spectra are generally taken in the derivative mode, the calibration is usually made using the peak-to-peak height ratio rather than the area under the $N(E)$ trace. If a Gaussian peak is assumed, both of these quantities are proportional.¹⁶

The Auger spectra were taken with a double pass CMA coupled with an electron gun. The electron beam came in perpendicular to the sample and had a kinetic energy of 3 keV. Ejected electrons with a specific kinetic energy were allowed to pass through the negatively charged outer and grounded inner cylinders of the CMA on their way to the electron multiplier (Physical Electronics, 20-075). The electrons emitted from the sample

pass through an annular slot in the inner cylinder and are then deflected by V_{out} . For electrons to pass through the exit slot, their kinetic energy must equal the pass energy of the CMA. Electrons with a greater kinetic energy than the CMA pass energy will strike the outer cylinder, while electrons with smaller kinetic energies will strike the inner cylinder. By ramping V_{out} , one can obtain the electron energy distribution, $N(E)$ vs. E . The energy resolution of the CMA (ΔE) depends linearly on the kinetic energy of the electron. A lock-in amplifier, acting as a phase sensitive detector, selects only the component of the signal with the same frequency as the original modulation (ω), since its amplitude is proportional $dN(E)/dE$.

2.1.2 X-Ray Photoelectron Spectroscopy (XPS)

X-ray photoelectron spectroscopy (XPS)^{17, 18, 19, 20, 21} is based on the photoelectric effect (photoionization, photoemission) outlined by Albert Einstein in 1905.²² The principle behind XPS is that a sample is irradiated with a nearly monochromatic x-rays and then the kinetic energy of the emitted core electrons is monitored (Figure 2.5). Soft x-rays of 1-2 keV ionize the atoms in a solid. The kinetic energy of the emitted electrons leaving the solid and entering the vacuum (10-1000 eV) depends on the energy of the x-ray photon and the binding energy of the electron. The binding energy of the core and valence electrons is a function of the chemical environment and oxidation state of the surface atom. The position of the peaks in the energy spectrum thus identifies different elements, and the shifts in the binding energies of core electrons dictate the different oxidation state of the same element. Chemical shifts are typically on the order of 0-3 eV from known standards. The withdrawal of electron density from an element, as is the

case in oxidation, changes the electronic potential at the valence shell and usually increases the binding energy of the core electrons in relation to the neutral atom. Upon further analysis, however, it is also important to take into account the relaxation of the remaining electrons in the ionized solid as well as the electrons in the neighboring atoms. These factors tend to lower the total energy of the final ionized state and increase the kinetic energy of the photoelectron; thus, shifting the binding energy to lower energy. The chemical shift is truly dependent on both the initial oxidation state and the final ionized state. XPS can distinguish these different oxidation states by primarily interpreting the binding energy shifts in terms of the initial state and referencing known standards. This technique essentially produces a fingerprint for the composition and nature of the surface of the sample. Qualitatively, the compositional analysis of a mixed sample may be performed by comparing the peak area or height of each element present in the spectrum. Quantitatively, the integrated intensity of the XPS peaks is proportional to the surface concentration of the element. Quantitative compositional analysis requires the use of sensitivity factors for each peak, which accounts for the photoelectric cross section of the atomic orbital, the mean free path of the photoelectron, and the detection efficiency for electrons emitted from the sample. XPS is surface sensitive to the short range (first few atomic layers or 10-30 Å) of the photoelectrons that are excited out of the solid. Much like AES, XPS is not sensitive to H or He.

The binding energy, BE, is related to the kinetic energy, KE_{measured} , of the core electron through the relationship:

$$KE_{\text{measured}} = h\nu - BE_{\text{electron}} - \Phi_{\text{spectrometer}}$$

where KE_{measured} is the measured kinetic energy of the outgoing electron, $h\nu$ is the energy of the monochromatic photons, BE_{electron} is the ionization energy or binding energy of the core-level electron, and $\Phi_{\text{spectrometer}}$ is the work function of the spectrometer introduced to correct for the contact potential between the grounded sample and the spectrometer. A photoelectron spectrum is obtained by measuring the outgoing electron flux ($N(E)$) as a function of binding energy (E). The expression for the intensity of an XPS peak is:

$$I = F_x S(E_k) \sigma(E_k) \int_0^{\infty} n(z) e^{-z/\lambda(E_k) \cos(\theta)} dz$$

where I is the intensity of the XPS peak (area), F_x is the flux of electromagnetic radiation or x-rays on the sample, $S(E_k)$ is the detector efficiency for measuring electrons with kinetic energy E_k , $\sigma(E_k)$ is the cross section for photoemission, $n(z)$ is the atomic density, z is the depth penetrated into the sample, $\lambda(E_k)$ is the mean free path of an electron with kinetic energy E_k in the sample, and θ is the take-off angle (angle between the direction in which the photoelectron is emitted and the surface normal). In practice, the sensitivity factor (S) for each element is introduced by the relationship:

$$I_j = n_j S_j$$

where I_j is the intensity of the XPS peak (area) and n_j is the atomic number density of element j . The concentration of species j (C_j) can then be calculated as such:

$$C_j = \frac{\frac{I_j}{S_j}}{\sum_{i=1}^t \frac{A_i}{S_i}}$$

The summation is over all species present and sensitivity factors have been tabulated.²⁰

In the XPS process, Auger peaks are also generated from the decay of ionized atoms and detected. Auger electrons, unlike photoelectrons, have kinetic energies that are independent of the photon energy and hence appear to have different binding energies with different x-ray sources. Because the x-ray sources—Al $K\alpha$ (1486.6 eV) and Mg $K\alpha$ (1253.6 eV)—do not produce truly monochromatic x-rays, additional peaks from satellite transitions are also generated. These plasmon excitations or shake-up lines are final state effects. They arise when the photoelectric process leaves an ion in an excited state a few eV above the ground level. The kinetic energy of the photoelectron is then reduced by this relaxation energy of the ion. When the energy of the photoelectron is transferred to the plasmon excitation in a metallic sample, multiple smaller peaks may appear at specific higher binding energy distances from the main photoelectron peak that are characteristic of the anode material used. If the additional excitation is a second stage of ionization, thus ejecting 2 photoelectrons, it is called a shake-off line. The spectra may show multiplet splitting, energy loss lines, and valence lines and bands as a result of all of these side processes. Secondary electrons are emitted from cascade effects produced by the ejected photoelectrons.

XPS experiments were performed with a Physical Electronics ESCA (PHI 5400) system. The system was pumped with a turbomolecular pump and an ion pump. Both Al $K\alpha$ (1486.6 eV) and Mg $K\alpha$ (1253.6 eV) were available as excitation sources. The Mg source was generally used since its x-ray intensity is higher and its linewidth is narrower than the Al source. The Mg source was operated at 400 W power (15 kV). Pass energies were selected as necessary. Most studies were performed with the angle between the surface normal and the analyzer being 45°. The x-rays were not filtered and were not

monochromatic, resulting in satellite peaks that were eliminated through spectrum processing. Electrons were detected with a hemispheric energy analyzer. The samples were grounded through metallic sample holders, which was moved from the sample stage part of the chamber to the detector through the use of a transfer arm. Survey and multiplex data was collected in the energy range of interest. Carbon and oxygen peaks from contaminations were used as internal calibration peaks.

2.2 Characterization Techniques: Surface Science Microscopy and Spectroscopy Tools

Microscopy and spectroscopy methods are invaluable in studying nanoscale objects. They can provide crucial insight into the nature of the system by imaging the physical dimensions of the object and reporting interactions of these nanosized objects with their environment. This section will overview three microscopy techniques that were used to characterize the nanocatalysts—atomic force microscopy (AFM), scanning electron microscopy (SEM), and transmission electron microscopy (TEM)—as well as an *in-situ* spectroscopic method, sum frequency generation vibration spectroscopy (SFG), whose initial results hold promise for this tool to become a standard surface science tool for probing the surface and interface of nanoscale objects.

2.2.1 Atomic Force Microscopy (AFM)

Atomic force microscopy came into being from its parent technique of scanning tunneling microscopy.^{23, 24} Since the mid 1980's, AFM has become one of the most powerful tools of the surface scientist.^{25, 26} The principle of AFM works in the following

manner. An extremely sharp tip—radius of curvature of ~ 20 nm with an appropriate force constant—is attached to a flexible cantilever and brought into contact or near-contact with the sample, depending on the mode of operation. The approach of the tip to the sample is first accomplished with the aid of a micron-scale stepper motor followed by the more precise movements (nanometer-scale) of a piezoelectric actuator. This piezoelectric material alters its solid state structure in response to an applied voltage. This distortion creates a change in length of this ceramic material on the order of Å-nm. The tip then interacts with the surface through various intrinsic and induced potentials and maps out the physical dimensions of the sample (topography) as well as probes the mechanical behavior of the surface. Some of these potentials or forces include attractive van der Waal forces²⁷, adhesive forces, capillary forces, electrostatic forces, and contact forces. Van der Waal forces arise from the interactions of all atoms due to instantaneous fluctuating dipoles in the atoms. This potential between all of the atoms, w , can be expressed as:

$$w = -\frac{A}{d^6}$$

where A is a constant and d is the separation distance between two atoms. Another consideration is the interaction between the atoms on the surface with the atoms that make up the AFM tip. Following Hamaker's assumption²⁸ that this interaction is additive and nonretarded with a continuous medium and uniform material properties, the total force between two objects can be integrated according to the following expression:

$$w_{sphere-plane} = -\frac{HR}{6d}$$

where H is the Hamaker constant, R is the radius of the tip that is modeled as a sphere, and d is the distance between the sphere and the surface that is modeled as a flat plane.

The Hamaker constant is defined as:

$$H = \pi^2 A \rho_1 \rho_2$$

where A is the constant of the pair potential and ρ_1 and ρ_2 are the atomic number densities of the two interacting bodies. Differentiating this formula then gives the following van der Waal force expression:

$$F_{\text{sphere-plane}} = -\frac{HR}{6d^2}$$

Adhesion forces are needed to separate the tip from the surface once they are in contact.

Following the same assumptions, the adhesive force (F_A) can be approximated as:

$$F_A = 4\pi R\gamma$$

where γ is the interfacial energy. Capillary forces can play a factor in AFM data collection when studies are performed in a humidified environment, as water can condense between the tip and the sample surface. The magnitude of the capillary forces (F_C) is approximated as:

$$F_C = 4\pi R\gamma \cos \theta$$

where γ is the water surface tension and θ is the contact angle. Long-range electrostatic forces (F_E) arise when a bias voltage is applied between the tip and the surface. This force, in Newtons, can be approximated as:

$$F_E \cong \frac{3RV^2}{d}$$

where R is the radius of curvature of the tip, d is the distance between the tip and the sample, V is the voltage applied between the two surfaces, and the assumption that $R > d$

must hold true. Lastly, there is the issue of contact or mechanics forces. There are three popular models that describe the physical contact of the tip and the surface. They are the Hertz model²⁹, the JKR model³⁰, and the DMT model³¹. The details of these models will not be explained here; original publications should be consulted wherever necessary.

Experimentally, the cantilever deflections are monitored with a photodiode (Figure 2.6). A laser beam hits the reflective coating of the top of the cantilever and is directed into a position-sensitive photodiode, which measures the intensity of the laser beam and outputs voltages in each of four areas. By comparing the voltages in each quadrant, the tip movement and therefore the topography of the surface can be measured (Figure 2.7). A feedback loop is utilized that holds the deflection of the cantilever constant as it rasters across the surface of the sample. As the tip encounters a feature on the surface, the piezoelectric actuator adjusts to maintain the constant deflection. By spatially recording the movements of the piezoelectric, the topographic detail of the sample is generated.

The AFM studies were performed on two different instruments: Park Scientific Instrument Autoprobe M5 and Molecular Imaging Pico SPM 100. The systems consisted of a detachable scan head, force detection system, feedback electronics, and noise damping components. The feedback electronics could be manipulated depending on the mode of operation for the AFM. When the feedback circuit is switched on, the tip-sample distance was kept constant, resulting in a constant force between the tip and the sample. When the feedback circuit is switched off, the tip scans across the sample surface at constant height. This mode of operation is used to generate a spatial map of the interaction force (topography). Noise damping components are incorporated into the

system to improve the signal-to-noise ratio. For the images presented in this dissertation, the AFM was operated under constant force mode.

2.2.2 Scanning Electron Microscopy (SEM)

The general steps of how an electron microscope^{32, 33, 34} creates an image and provides structural and compositional information is as follows: 1) a stream of electrons is formed and accelerated toward the sample (cm range thickness) using a positive electrical potential; 2) this stream of electrons is focused using metal apertures and magnetic lenses into a thin, focused electron beam with a diameter that is less than 10 nm; 3) the beam is focused onto the sample using a magnetic lens; and 4) the interactions that occur inside the irradiated sample that affect the electron beam are monitored and used to create an image (Figure 2.8).

For a thermionic electron gun, a positive electrical potential is applied to the anode. The filament (cathode) is then heated until a stream of electrons is produced. These electrons are then accelerated by the positive potential down the column. In general, the electron gun provides a large, stable current in a small electron beam and then accelerates the electrons towards the sample. The first condenser lens forms the beam and limits the amount of current in the beam. It works in conjunction with the condenser aperture that further constricts the beam and eliminates high-angle electrons from the beam. The electron beam is demagnified in regard to its diameter from 10-50 μm out of the electron gun to the final spot size of 1-1000 nm on the sample. A second condenser lens forms the electrons in a thin, tight, coherent beam, with an objective

aperture reducing more of the high-angle electrons in the beam. A set of coils then scan or sweep the beam in a grid-like fashion, dwelling on points for a period of time determined by the scan speed (μs range). The final lens in the column, called the objective lens, focuses the scanning beam onto the desired area of the sample. This lens is the most critical lens in controlling the resolution of the microscope. It focuses the image by controlling the movement of the probe along the optical axis of the column and demagnifies the electron beam even more. The beam strikes the sample, resting in a spot for a few microseconds before moving to the next dwell point. The instrument that monitors the interactions that occur inside the sample counts these interactions and displays the pixels on a cathode-ray tube (CRT). The intensity is determined by the number of these interactions, with a brighter pixel equating more reactions/interactions. This process is repeated until the grid scan is finished; the entire pattern can be scanned 30 times/s. The resolution in SEM is determined by the size of the electron probe; therefore lens aberrations that can severely enlarge the final spot size must be carefully eliminated to ensure resolution. By having cryogenically cooled electron optics, the limits of resolution are being approached as set by the astigmatism of the optics. A higher acceleration voltage (~ 30 kV) helps to reduce the electron beam size by increasing the brightness of the electron source. With advanced field emission sources, the same electron beam size can be achieved with a lower acceleration voltage (1-10 kV). This can eliminate the problem of charging within the sample.

The aforementioned interaction between the highly energetic electrons and the sample can be divided into two categories: elastic and inelastic events. Elastic scattering produces backscattered electrons while inelastic scattering generates secondary electrons,

Auger electrons, and x-rays (characteristic and bremsstrahlung), cathodoluminescence. The energy distribution of all electrons emitted from a sample, measured from the incident electron beam energy (E_0) to 0 keV, yields a curve as displayed in (Figure 2.9).³⁵ Backscattered electrons dominate the distribution, except at much lower energies (< 50 eV), where the number of electrons emitted from the sample dramatically increases to a level much greater than the expected contribution from backscattered electrons; this contribution is the result of secondary electrons. These secondary electrons arise from the interactions between energetic electrons and the loosely bound conduction band electrons in metals or outer-shell valence electrons in semiconductors. The difference in energies of these two systems causes the energy transfer to be inefficient and thus lead to the small kinetic energy of the secondary electrons. The SEM image is formed from the secondary and backscattered electrons that are collected and processed. Secondary electrons are more sensitive for topographic variations on the surface of the sample as they are confined to a volume near the electron beam's impact area, permitting images to be obtained at relatively high resolution. The more energetic backscattered electrons are chemically sensitive and have a larger interaction volume. While these images have lower resolution, they give atomic number contrast between different elemental compositions.

The SEM images presented in this dissertation are taken with a Joel JSM-6340F field emission SEM. Typical conditions were an acceleration voltage of 5 keV, an emission current of 12 μ A, and a working distance of 6 mm.

2.2.3 Transmission Electron Microscopy (TEM)

Almost four decades after the discovery of the electron by J.J. Thompson in 1897, Max Knoll and Ernst Ruska discovered how to propel electrons through a sample to create an image, much like the process of optical microscopy.³⁶ This technique is the most powerful characterization tool for studying the morphology of flat objects^{32, 37, 38, 39}, especially on the nanoscale. TEM utilizes electrons that are accelerated in the 100-200 keV range from an electron source (thermionic or field emission gun). These electrons illuminate a sample that is typically 3 mm in diameter and ≤ 5000 Å thick. After the electrons pass through the sample, they are focused by an electromagnetic objective lens to form an image. Other lenses in the optical column are used to image the diffraction pattern at the back focal plane of the objective, magnifying the image up to 1 million times its original size (Figure 2.10). The resolution attained is in the 2-3 Å range. TEM is highly sensitive to changes in thickness. It can provide either diffraction contrast for thick specimens (≥ 1500 Å) or defocus contrast for thinner samples (≥ 500 Å). Both SEM and TEM use intense electron beams that can severely damage the surface of the sample, even with the small electron-atom cross sections at these very high energies. To reduce the destruction of the surface, both SEM and TEM have short dwell times in any given spot on the sample. In addition to the structural information provided through electron diffraction, TEM offers the possibility of studying the effects of individual atomic adsorbates including diffusion and pair-spacing distributions. Clusters can also be investigated, with the ability to probe phenomena such as nanoparticle sintering and migration. The details of the principle of transmission electron microscopy can be found elsewhere in the literature.^{40, 41, 42, 43, 44, 45, 46}

All TEM images were taken on a Philips CM 200 FEG/UT system. Samples were mounted to a glass slide with crystal bond, with the catalyst array facing the slide. A 3 mm diameter disk was cut from the sample using an ultrasonic disk cutter (Gatan). The sample was mechanically thinned using a polisher (Minimet) to 200- μ m thickness. The sample was made nearly optically transparent with the aid of a dimpler (VCR). The dimpler milled a convex hole on the backside of the sample, making the center of the sample the thinnest region. A hole was created in the center of the sample via ion milling with 1.5 kV Ar⁺ sputtering at an angle of 15°. The area directly around this hole was thin enough to be electron transparent.

2.2.4 Sum Frequency Generation Vibrational Spectroscopy (SFG)

A recent experimental technique that has been developed and is fast-proving to be a convincing tool of surface scientists with its ability to probe absorbates (composition and orientation) at interfaces in real time and *in situ* is sum frequency generation vibrational spectroscopy (SFG).^{47, 48, 49, 50, 51, 52, 53, 54, 55, 56, 57} The history of SFG⁵⁸ is based in non-linear optical phenomena and specifically frequency conversion. Second-harmonic generation (SHG) was first demonstrated in 1961 by Franken *et al.*⁵⁹ The foundations of the theory of SHG and SFG were reported by Bloembergen *et al.*^{60, 61} SHG and SFG vibrational spectroscopies entered the realm of the surface scientist in 1974⁶² and 1987⁶³, respectively. The principle behind SFG is the conversion of two photons with frequencies ω_{VIS} and ω_{IR} to a new photon, ω_{SFG} , of frequency (vector notation has been left out of all terms and equations for simplicity):

$$\omega_{SFG} = \omega_{VIS} + \omega_{IR}$$

In this three wave mixing process, the visible and infrared beams are incident on the surface and overlap in space and time in a common spot with a diameter on the order of a few hundred microns. Accordingly, the selection rules for both IR and Raman spectroscopy must be maintained. The intensity of the light generated at the sum frequency— $I(\omega_{\text{SFG}})$ —is proportional to the square of the third-rank tensor known as the surface non-linear susceptibility, $\chi^{(2)}$.

$$I(\omega_{\text{SFG}}) \propto |\chi^{(2)}|^2$$

The tensor is mathematically a 3×3×3 matrix, with 18 out of these 27 matrix elements being non-zero. Under the electric-dipole approximation, $\chi^{(2)}$ is zero for centrosymmetric materials. For surfaces that are rotationally isotropic around the surface normal, there are only three matrix elements. In SFG, the tunable IR beam (2000-4000 cm^{-1}) becomes resonant with at least one vibrational mode of species at an interface. The second visible beam (532-nm green light) further excites this vibrational mode to a virtual state, which then relaxes to a lower energy state and releases the blue photon at the sum frequency. The susceptibility has a resonant part due to IR transitions in the adsorbate and a non-resonant part, mainly due to the substrate, that produces a background to the vibrational peak.

$$\chi^{(2)} = \chi_{\text{NR}}^{(2)} + n_s \langle \alpha_R^{(2)} \rangle_f = \chi_{\text{NR}}^{(2)} + \sum_q \frac{A_q}{\omega_{\text{IR}} - \omega_q + i\Gamma_q}$$

where $n_s \langle \alpha_R^{(2)} \rangle_f$ is the vibrationally-resonant contribution to the susceptibility made up of the molecularly averaged number density (n_s) and the orientation-averaged non-linear polarizability ($\langle \alpha_R^{(2)} \rangle$) over some distribution function (f). This resonant term can be

further described in terms of an oscillator strength (A_q) and a damping term (Γ_q) associated with some vibrational mode (q). Detailed calculations and formulas can be found and derived from the expressions found in the aforementioned literature on SFG.

The experimental set-up of the SFG system is outlined in Figure 2.11. Briefly, a tunable IR source beam was generated from a 20 ps, 20 Hz Nd:YAG laser through optical parametric processes. IR in the 5-8 μm range was generated by a combination of optical parametric generation (OPG) and optical parametric amplification (OPA) in two BBO crystals and then difference frequency generation (DFG) in an AgGaS₂ crystal. IR in the 2-4 μm range was generated in the same OPG/OPA system, but a LiNbO₃ crystal was used in the DFG stage. The second harmonic output (532 nm visible beam) was generated by frequency doubling the YAG fundamental in a LBO crystal. All beams were *p*-polarized unless otherwise stated, and their pulse energies at the surface were 250 μJ for the visible (green) beam, 100 μJ for the 2-4 μm range IR beam, and 80 μJ for the 5-8 μm range IR beam. Their incident angles on the sample surface were 55° and 60°, respectively. Two pyroelectric energy meters were used to monitor the intensity of the IR beams. The detection system consisted of a 532-nm notch filter, an interference filter, a polarizer, a monochromator, and a photomultiplier tube. Wavelength calibration for the IR beams was accomplished with polystyrene for the C-H stretch region and gas phase CO and CO₂ for the CO stretch region. A mobile reaction cell to house the nanoparticle samples was aligned to the laser table. A different chamber was utilized for single crystal samples.

2.3 Fabrication Techniques

As much as the integrated circuitry is driven by Moore's Law⁶⁴, nanotechnologies⁶⁵ and nanosciences⁶⁶, as alluded to by Richard Feynman in his "There's Plenty of Room at the Bottom" speech given at Cal. Tech in 1959⁶⁷, are fast-becoming the driving forces within the hard sciences⁶⁸ to gain insight into the fundamentals of basic science. This emphasis on nanoscience and nanotechnology is largely due to the advances made in scanning probe microscopy^{23, 24, 25, 26} and the availability of microfabrication facilities.⁷² Borrowing knowledge from microfabricated devices, nanosystems of all kinds are concerned with the size regime of 1-100 nm.⁶⁹ These nanosystems have varied applications, including the next generation of electronics⁷⁰, magnetic storage devices^{71, 72}, optical devices⁷³, and biological devices^{74, 75, 76}. The ability to reproducibly and economically fabricate nanostructures with atomic precision is paramount to all of these fields. Great strides have been made in microfabrication and nanofabrication both in industry and academia, with the advances in new lithography techniques. However, there is yet to be a single technique that embodies every desired attribute in a production process. The development of nanofabrication is briefly detailed in the following sections.

The nanofabrication methods either utilize photons and charged particles^{77, 82} or other forms of lithography that utilize scanning probes⁷⁷, self-assembly^{78, 79}, soft lithography⁸⁰, etc. Methods that incorporate photons or charged particles include electron beam lithography (EBL), extreme ultraviolet (EUV), and focused ion beam lithography (FIB). These techniques are more mature technologies, as the microelectronic industry has focused their attention on developing them as the next generation lithographies. EBL

will be extensively described in a later section, so this discussion will only concern EUV and FIB.

EUV lithography employs photons with wavelengths of 11-14 nm in order to minimize the diffraction problems that plague the resolution of conventional UV photolithography. Despite the feature size attainable by this method (< 40 nm), it is not yet a robust and production-worthy technique for the fabrication of masks and optics.⁸¹ FIB is similar to EBL in principle and resolution (< 50 nm), except that it utilizes ions instead of electrons. Through the use of much heavier ions, the issue of backscattering is diminished greatly; however, radiation damage to the substrate becomes a concern.⁸³ For the most part, FIB is used as a repair service for EBL-fabricated masks, ion milling, and induced depositions.^{82, 83}

The other non-conventional lithography techniques have their foundations in research labs instead of in industry. Accordingly, these methodologies are more developmental; though, they are quickly becoming scaleable technologies. These include nanoimprint lithography (NIL)^{84, 85}, scanning probe lithography (SPL)⁸⁶, nanosphere lithography (NSL)⁸⁷, pattern formation using self-assembly⁸⁸, controlled deposition⁸⁹, to name a few. Some of these techniques are outlined below.

SPL manipulates single atom or molecule transfer via a small radius tip (< 50 nm) in the configuration of STM⁹⁰ and AFM⁹¹. In the STM configuration, a large electrical bias between the STM tip and the sample causes single atom transfer⁹² (transfer flow dependent on the polarity of the bias). This technique obviously yields the highest resolution (angstrom-level), with some practical applications already demonstrated.⁹³ In the AFM configuration, the sample is manipulated either mechanically—pushing each

component into place⁹⁴, scratching the surface with the tip under a large load—or chemically—transferring molecules to where the tip makes contact with the surface.⁸⁶ Sub-10 nm resolution has been demonstrated with this configuration. Other SPL methods include the use of near-field scanning optical microscopes to modify the sample chemically with photons.⁹⁵ While all of these techniques have excellent resolution, they are all serial processes due to pattern generation being dictated by contact between the tip and the sample. The slow nature of these methodologies limits their widespread use in industry.

NSL uses the self-assembly of colloidal nanospheres into close-packed monolayers or bilayers. This process is as follows. 1) drop-coat a sacrificial layer of colloidal nanospheres on a substrate and allow them to self-assemble to form a mask; 2) deposit metals via vapor deposition; 3) remove the mask by etching and sonication. This produces arrays of metal nanospheres on the substrate that occupy positions approximately corresponding to the void spaces from the colloidal nanosphere mask. The size, periodicity, and pattern of the array are dictated by the size of the nanosphere and the angle between the substrate and the deposition source. This technique is a high-throughput method, but the resolution (< 100 nm) and pattern are limited by defects during the self-assembly steps.

NIL or hot embossing lithography is a technique for pattern transfer, not pattern generation. This technique will be explained in detail in a later section. In general, a rigid mask is pressed into a thermoplastic polymer that has been softened with heat. It is a high-throughput process capable of sub-10 nm resolution.

For nanocatalyst fabrication, the issues of resolution and throughput were paramount. While NIL is best suited to address resolution and throughput, it does not produce the pattern. Considering the necessary size (sub-10 nm features) and surface area ($\sim\text{cm}^2$) regimes necessary for probing industrially significant reactions, new advanced lithography techniques had to be developed and utilized to create the samples to study catalytic reactions. The next section will outline the three main fabrication techniques that were developed and employed for the production of next-generation model catalyst arrays: electron beam lithography (EBL), size reduction lithography (SRL), and nanoimprint lithography (NIL).

2.3.1 Electron Beam Lithography (EBL)

Electron beam lithography (EBL)^{96, 97, 98, 99, 100, 101} is a mature technology utilized for high-resolution patterning via direct writing through the use of a focused and narrow beam of high energy electrons (10-100 keV) and electron-sensitive resists (Figure 2.12).¹⁰² An EBL system consists of an electron source that produces a small-diameter spot and a blinder that can turn the beam on and off (Figure 2.13). The exposure takes place in a vacuum to minimize air molecules from interfering with the electron beam. The exposure control system determines the electron dose and position of delivery on the sample surface. The beam passes through electrostatic plates capable of steering the beam in the x - y direction on the mask, reticle, or wafer. Position delivery is crucial, as feature placement precision must generally be on the order of 15% of the size of the feature. Issues such as beam drift due to charging, turbulence in the interferometric path, distortions of the interferometer mirrors, and the accuracy with which deflection

distortions can be corrected in a finite time must be addressed to ensure placement precision. The optics in SEM and TEM are very similar to those in an EBL system. The resolution in EBL is not limited by diffraction, as the quantum mechanical de Broglie wavelengths of high-energy electrons are extremely small (10^{-3} - 10^{-4} nm). But the resolution is also not solely dependent on the spot size of the focused beam. Resolution is also affected by scattering of the electron beam inside the resist and substrate and by backscattering from the substrate exposing the resist over a greater area than the beam spot size. This proximity effect^{103, 104, 105} is outlined in Figure 2.14. The smallest feature that a lithography system can print is¹⁰⁶:

$$R = \lambda / NA$$

where R is the resolution, λ is the wavelength of the radiation, and NA is the numerical aperture that is a measure of the angular range of incident radiation that can be collected by the system. To increase resolution, systems must either use shorter wavelengths or larger numerical apertures. The distance over which the image remains in focus decreases as λ / NA^2 . The sequential writing of the pattern delivers a certain amount of current and yields a fixed amount of energy deposited on the sample surface. The maximum dose delivered by the electron beam is given by⁷²:

$$D_{\max} = it / A$$

where D is the dose in coulombs/cm², I is the current that is limited primarily by the source brightness and column design, t is the flash time in seconds that is a measure of the speed at which the writing beam can be moved and modulated, and A is the pixel area

in cm^2 . The energy deposited on the sample surface is expressed in the following double Gaussian equation⁶⁹:

$$f(r) = \frac{1}{1 + \eta} \left\{ \frac{1}{\beta_f^2} \exp\left(-\frac{r^2}{\beta_f^2}\right) + \frac{\eta}{\beta_b^2} \exp\left(-\frac{r^2}{\beta_b^2}\right) \right\}$$

where r is the distance from the irradiation point, β_f is the forward-scattering range, β_b is the backward-scattering range, and η is the ratio of backward-scattering energy to forward-scattering energy. Both forward-scattering in the resist and backward-scattering from the substrate contributes to the proximity effect. The study of the resist material itself is of great importance. The resist has an inherent granularity that influences the minimum feature size possible. The other factor of the resist that can limit resolution is the inelastic scattering of the incident high-energy primary electrons that broaden the lateral exposure profile of the resist. To minimize this broadening, high-contrast formulation of a resist can be utilized. The selection of a resist must also incorporate the ability to react sufficiently fast at D_{max} . The electron resist sensitivity is measured in surface charge density, denoting the minimum charge density or dose required for proper resist development. The typical scission-based positive electron resist that gives the best resolution is polymethylmethacrylate (PMMA); however, it suffers from poor sensitivity to radiation and weak etch-resistance properties. The low atomic number of the resist and the long range of backward-scattering electrons means that these electrons contribute more to the exposure of resist outside of the impact area. Dose correction, shape correction, equalization of background dose, and multi-layer resist techniques have all been implemented to compensate for proximity effects. The resolution of the resist for dense and sparse features as well as the development and lift-off of the resist has been

addressed in the literature.^{107, 108, 109, 110, 111} Sub-10 nm resolution was demonstrated for isolated features by Vieu *et al.*, with practical resolution limited by the development of the resist after exposure.¹¹²

Electron beam lithography has its share of advantages and disadvantages. Aside from the high resolution that can be achieved with EBL, other advantages include precise control of the energy and dose delivered to the wafer, deflection and modulation of electron beams with speed and precision, imaging of electrons to form a small spot of <10 nm, no need for a physical mask, ability to register accurately over small areas of a wafer, lower defect densities, and large depth-of-focus. Disadvantages include the fast scattering of electrons in a solid that limit practical resolution, the requirement of a vacuum system, the slow exposure speed as it is a serial process that in turn affects the practical area that can be patterned, and the high cost of the system.⁷²

The EBL was performed with a Leica 100 EBL Nanowriter, equipped with a 100 keV thermal field emission electron gun and an optic column that can focus the beam to a width of 2.5–5 nm. The 4-inch wafer was coated with an oxide (SiO₂ or Al₂O₃), after which thermal oxidation at 800°C for 1 hr was performed to ensure thermodynamic stability. This wafer was first cleaned with isopropanol, acetone, and water. The resist used was 996K MW PMMA, which has a chemical structure of $-\text{[CH}_2\text{-C(CH}_3\text{)(COO(CH}_3\text{))}]_n\text{-}$, where n is $\sim 10,000$. A 2% PMMA in chlorobenzene solution was prepared and spin-coated onto the wafer at 4000 rpm for 45 s. The resist layer was then baked at 175°C for a minimum of 12 hr. After the square-periodicity pattern was generated in the computer, the wafer was then exposed. Typical conditions include a beam current of 600 pA, a dose of 2500 $\mu\text{C}/\text{cm}^2$, and a dwell time of ~ 6 μs at each

particle site Portions of the polymer backbone break when exposed to the electron beam radiation polymer; this makes the polymer more soluble in the developer solution that was 3:1 (volume ratio) isopropanol (IPA): methyl isobutyl ketone (MIBK). After the development of the PMMA, metal (platinum) was deposited uniformly and with complete coverage with the same electron-beam evaporator (Veeco) used to deposit the oxide layer on the wafer. This vacuum system was equipped with water-cooled crucibles with various metal and oxide sources, high-temperature filaments to create electrons, a magnet to direct the electrons into the source, and a sample holder at the top of the bell jar chamber to hold the wafer. Shutters and a quartz crystal monitor controlled the film thickness. The resist-undercut angle should be greater than the evaporation angle; the resist thickness should be greater than the metal thickness. The Pt deposition occurred at 5×10^{-6} Torr with a measured rate of ~ 1 Å/s. Care was taken to remain below the glass transition temperature of PMMA¹¹³ ($T_g = 120^\circ\text{C}$) during evaporation. After the metal deposition, standard liftoff procedures involving acetone and ultrasonication for 5 min were performed to remove the unwanted polymer. This entire procedure left metal nanoparticles on an oxide-supported Si(100) wafer.

2.3.2 Size Reduction Lithography (SRL)

The fabrication of nanoscale patterns with dimensions of 10 nm or less has been the goal of many researchers for potential applications as sensors¹¹⁴, soft x-ray optical device components, electronic circuit elements, or catalysts, to name a few. Electron beam lithography, with a finely focused electron beam, is the most commonly used technique for nanometer pattern generation by decomposing a polymer (usually PMMA)

in a desired pattern. However, the generation of secondary electrons during electron bombardment makes it difficult to achieve sub-10 nm patterning.⁸³ The maximum beam current that can be focused into a given area is fundamentally determined by the mutual repulsion of the electrons. This space-charge effect arises due to the electrons being forced closer together as the beam current is increased. The Coulomb forces eventually overwhelm the focusing action of the electron lenses, resulting in an increase in beam diameter and a blurring of the image. Electron beam lithography is also a sequential pattern-producing technique and is very time-consuming compared to photolithography-based processes that produce the whole pattern at once using a mask. This is also the case for other scanning probe based lithography techniques.¹¹⁵ One of the promising directions is to start with a pattern that is produced by photolithography that has spatial definition on the order of the wavelength of visible light (~600 nm) and then reduce the size of the elements that make up the through the use of a mask. There is a US patent that reports on a method of reducing the pitch of line and space dimensions from polysilicon (polycrystalline silicon) and a metal oxide by etching one of the materials that leaves the other material intact.¹¹⁶ Using similar techniques, the doubling of the frequency of lines in a grating made of silicon is reported to obtain a 100-nm pitch.¹¹⁷ Using siloxane self-assembled monolayers, edge transfer lithography was reported that managed size reduction of patterns to 100 nm¹¹⁸. Y.K. Choi *et al.* demonstrated spacer lithography to produce electronic devices in silicon with sub-40 nm structures starting from 600-nm structures produced by photolithography.^{119, 120, 121} The quality of their size-reduced structures were superior to those made by electron beam lithography. Using the techniques reported by Y.K. Choi *et al.*, the method of size reduction lithography

(SRL) was developed that produces 20-nm wide single-crystal silicon nanowire arrays, starting from a wire structure with a diameter (linewidth) of 600 nm. Further oxidation of the silicon nanowires and etching in HF reduced the dimensions to sub-10 nm (7 nm). Using SRL, 7×10^8 nanowires on a 4-inch Si(100) wafer were produced, yielding a total patterned surface area of $\sim 1 \text{ cm}^2$. As mentioned earlier, this surface area permits the study of all catalytic reactions, regardless of the magnitude of the turnover.

The scheme for SRL is provided in Figure 2.15. A thermal oxide is grown on the 4-inch Si(100) wafer. Polysilicon (poly-Si) is then deposited on top of the oxide by silane decomposition. Photoresist is spin-coated on the poly-Si film, and it is exposed to UV light through a mask that makes the exposed polymer soluble in a basic developer solution. The 600-nm wide wires are plasma-etched with Cl_2 and HBr in order to remove the exposed poly-Si. A layer of SiO_2 is then conformally deposited on top of the poly-Si structures, followed by a CF_4 plasma etch to expose the step edge of poly-Si and SiO_2 sidewalls. Using plasma etching (Cl_2 and HBr) again, the poly-Si is removed, leaving behind 200-nm wide SiO_2 wires. By employing CF_4 plasma etching again, SiO_2 protective layer is removed. The SiO_2 wires are then etched into the silicon wafer itself, via a Cl_2 and HBr plasma etch, until the desired height of the silicon wire is obtained. Finally, HF removes the remaining SiO_2 . This procedure reduces the size of the silicon nanowires by more than an order of magnitude (600 nm \rightarrow 20 nm). The initially-grown thermal oxide layer serves as the hard mask for Si etching; the poly-Si layer serves as a sacrificial layer; the low temperature oxide (LTO: SiO_2) sidewall deposition determines the final pattern size. The essence of the technique is based on the fact that material deposited during low-pressure chemical vapor deposition (LPCVD) covers the step edge

as well as the top of the step; this type of deposition is called conformal. In contrast, plasma etching is an anisotropic technique, removing materials preferentially in the direction perpendicular to the surface. Therefore, by depositing a material that has a different etching property than the sacrificial layer and directionally etching the material on the top of the step, the sacrificial layer can be removed selectively, leaving only the material deposited on the sacrificial structure sidewall. The feature size thus generated is determined by the thickness of the deposited material, not by the photolithography; the pattern pitch is determined by the minimum pattern obtainable with photolithography. Since the thickness of the deposited film can be controlled to 10 nm or less with high precision, this method is capable of generating nanopatterns that exceed the capabilities of optical lithography. The SRL process can be repeated multiple times by simply alternating the sidewall deposition material and the sacrificial layer material (poly-Si and SiO₂). The pitch of the nanowires is doubled with every cycle.

2.3.3 Nanoimprint Lithography (NIL)

SRL was utilized to overcome the feature size limitations of EBL. To address the problem of time, as EBL is a serial process, nanoimprint lithography (NIL) was incorporated to allow for parallel pattern transfer (Figure 2.16). After Chou *et al.* invented the process^{84, 85}, the development of NIL can be tracked in the literature.^{122, 123, 124, 125, 126, 127, 128} The principle behind NIL is simple. A hard mask bearing the nanopattern to be imprinted is brought into close contact with a flat substrate coated with a thermoplastic polymer. This imprinting resist is heated above its glass transition temperature in order for the polymer to become viscous and flow. Pressure is then

applied to force the features of some height into the thermally softened polymer. Upon cooling, the mask is manually separated from the polymer and substrate. This step essentially duplicates the pattern from the mold to the resist film (negative impression). There will be a residual layer of resist that must then be removed. The next step is to transfer the pattern through the removal of the residual polymer resist with an anisotropic etching process, such as reactive ion etching (RIE). This step transfers the thickness contrast pattern into the entire resist. NIL is a low-cost, high-throughput technology that does not have any of the drawbacks of conventional lithography methods that use an energetic beam. The commercialization of NIL is dependent on the ability to reproduce large patterned areas with dense and sparse features with a high degree of accuracy and precision. To this end, NIL is still in development and has not yet become a standard piece of equipment in research laboratories. Nanoimprint lithography is general and can be applied to a variety of metal and substrate combinations. The NIL process can be utilized for the mass production of nanostructures.

A home-built nanoimprint lithography press (Figure 2.17) was constructed that can achieve temperatures from 300-573 K, pressures from 10-300 atm, a vacuum to eliminate bubbles during the imprint process that can prevent uniform contact, and the ability to house a 2-inch wafer. After NIL, metal deposition, and liftoff procedures as described earlier, alumina-supported (and silica-supported) Pt nanowires remained. SRL and NIL together are capable of producing $\sim 1 \text{ cm}^2$ of Pt surface area—the necessary surface area for probing low turnover rate hydrocarbon conversion reactions.

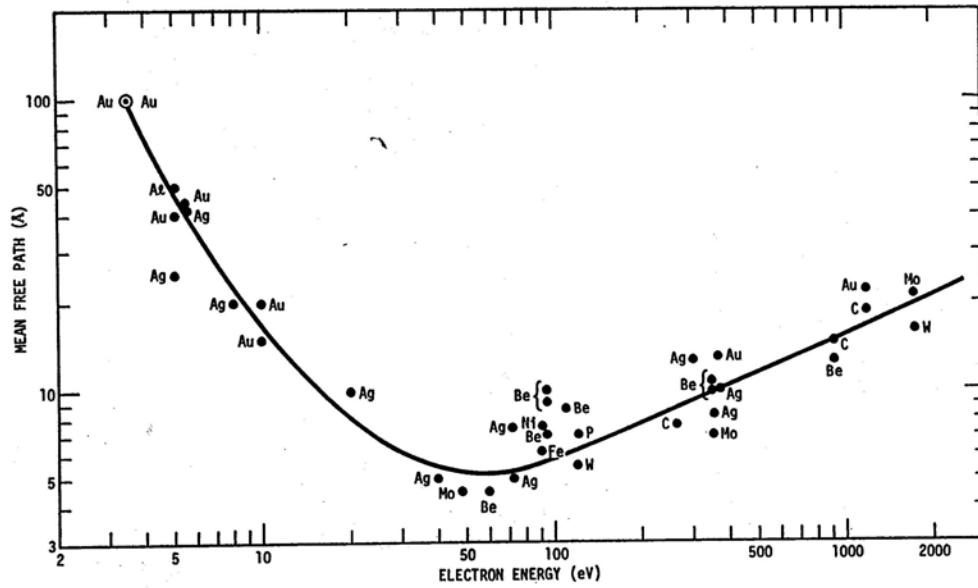


Figure 2.1. The Universal Curve that details the mean free path of electrons in solids as a function of their kinetic energy.

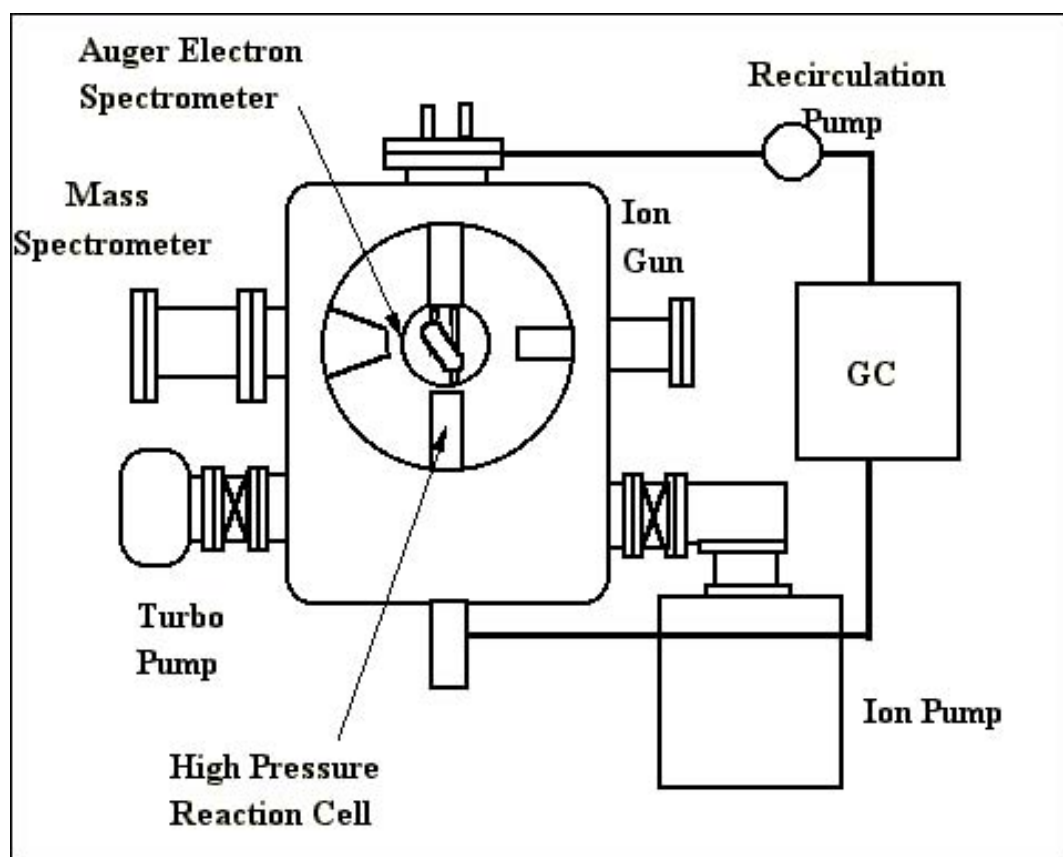


Figure 2.2. Schematic drawing of kinetics and surface science studies chamber.

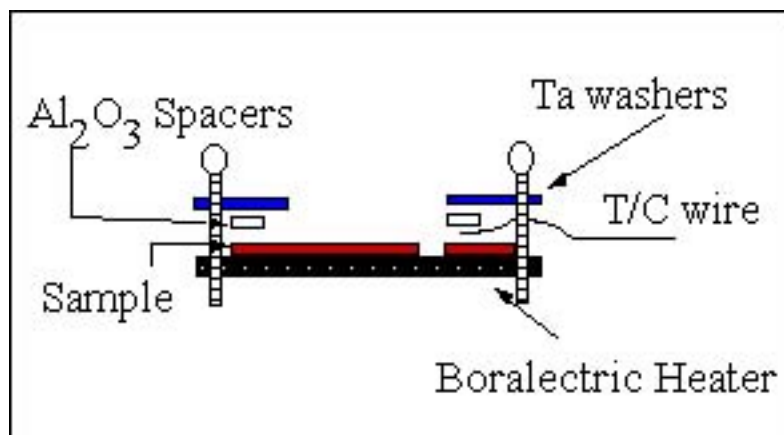


Figure 2.3. Schematic view of sample hole34, showing the catalyst, heater, and thermocouple assembly.

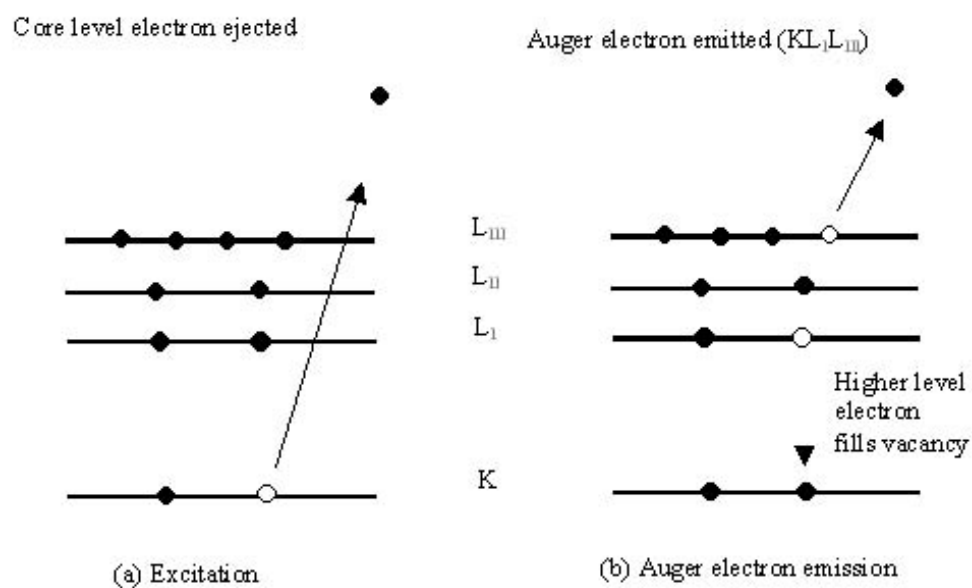


Figure 2.4. Schematic of the Auger electron emission process.

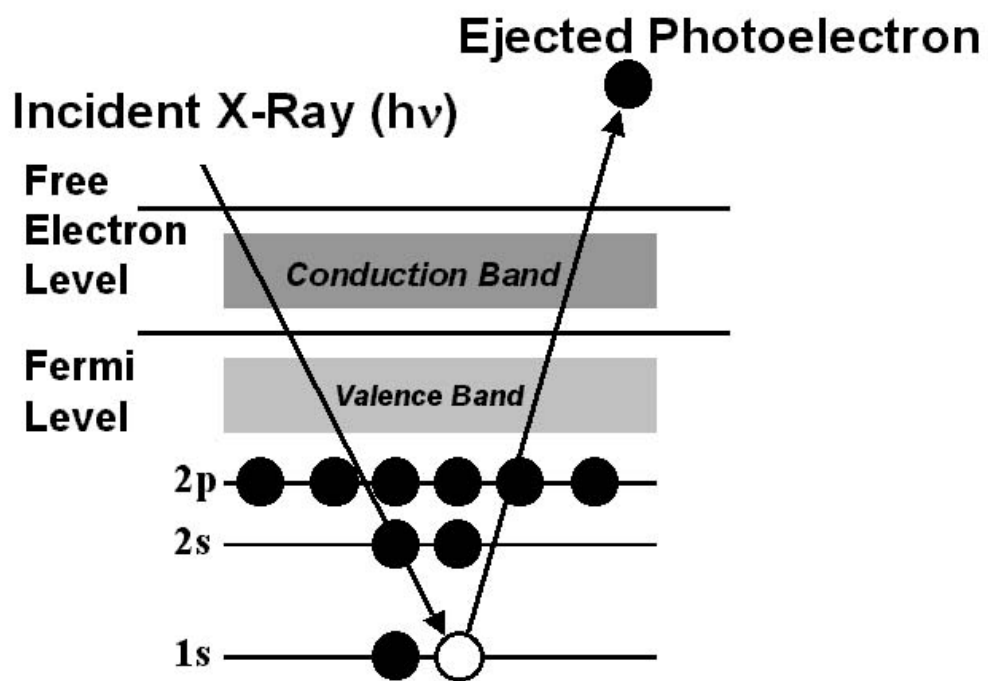


Figure 2.5. Schematic of x-ray photoemission process.

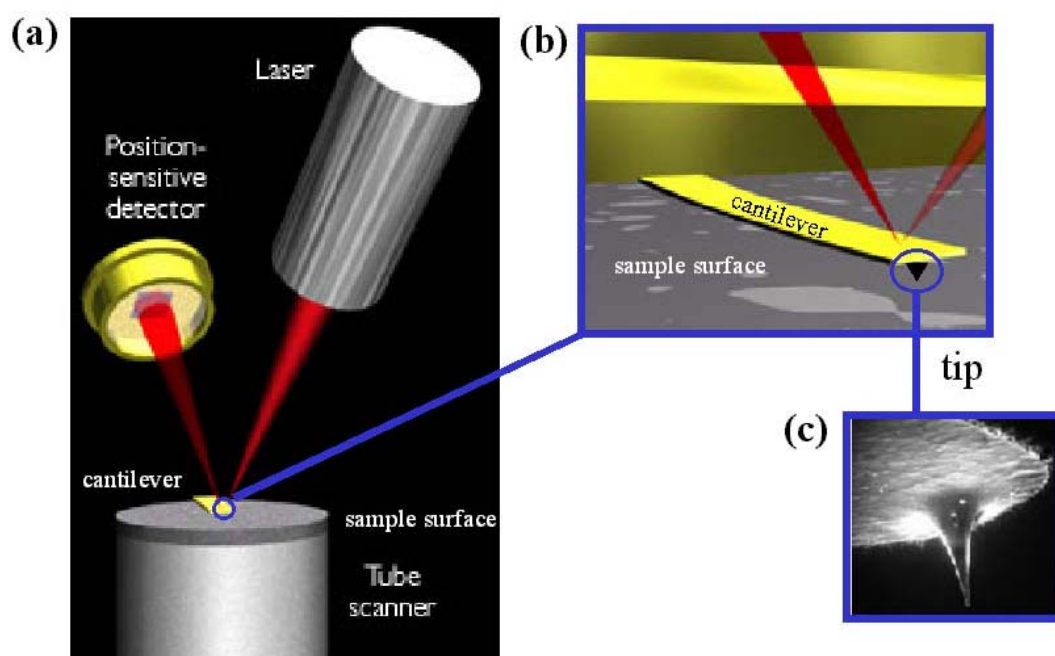


Figure 2.6. AFM set-up: a) complete configuration that shows laser, detector, cantilever, tip, sample surface, and tube scanner; b) detailed image of the cantilever, tip, and sample surface; c) detailed image of tip.

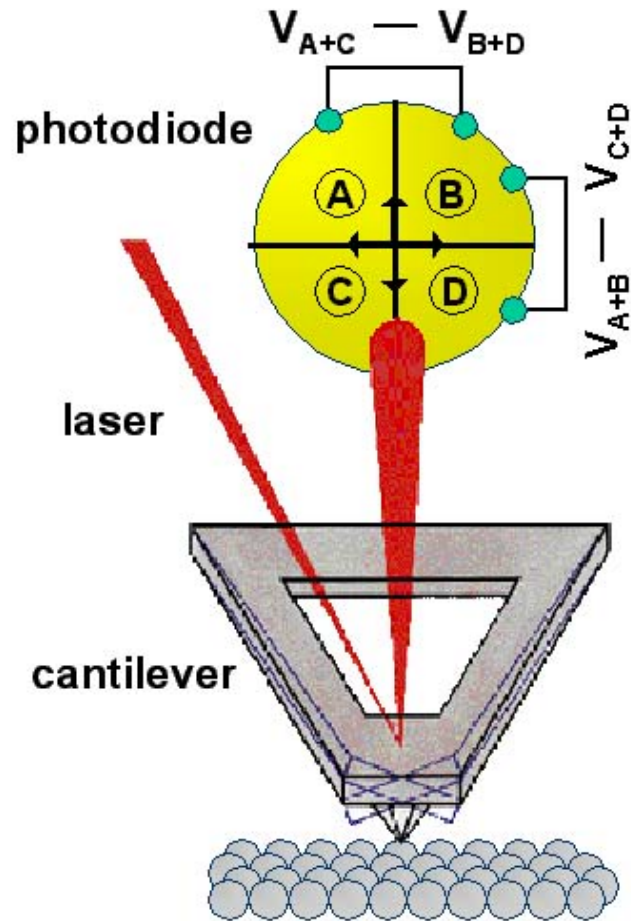


Figure 2.7. Tip movement (sample topography) is measured by mapping out the location of the reflected laser in the position-sensitive photodiode. Up-and-down motion is registered by comparing the voltages in the upper and lower quadrants. Left-and-right motion indicates the amount of torque on the cantilever (coefficients of friction).

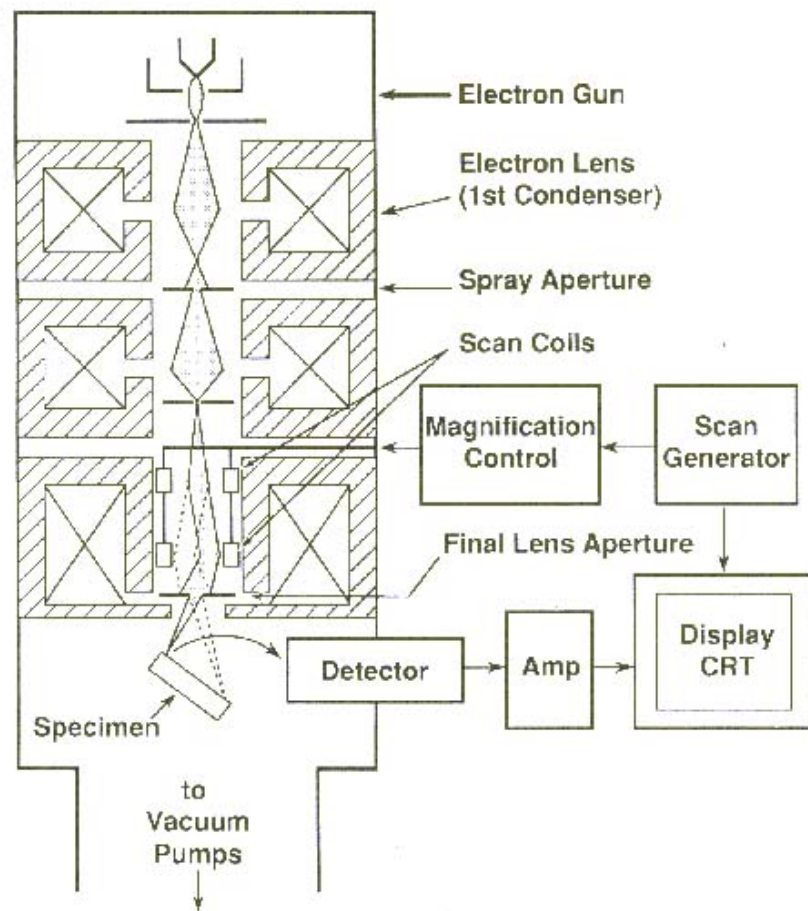


Figure 2.8. Schematic of scanning electron microscope, showing the electron column, deflection system, and detection system.

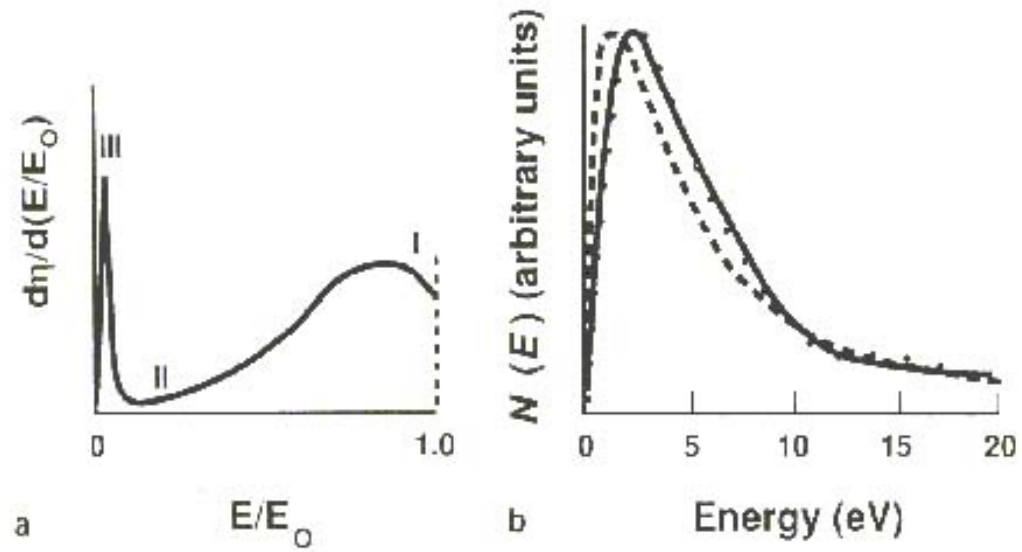


Figure 2.9. a) Energy distribution of electrons emitted from a target, including backscattered electrons (I, II) and secondary electrons (III). b) experimental (solid) and theoretical (dashed) secondary electron energy distribution.

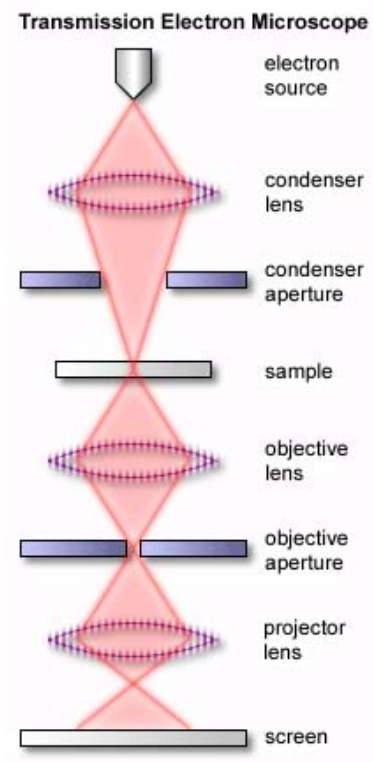


Figure 2.10. Schematic of transmission electron microscope, showing the electron column, deflection system, and imaging system.

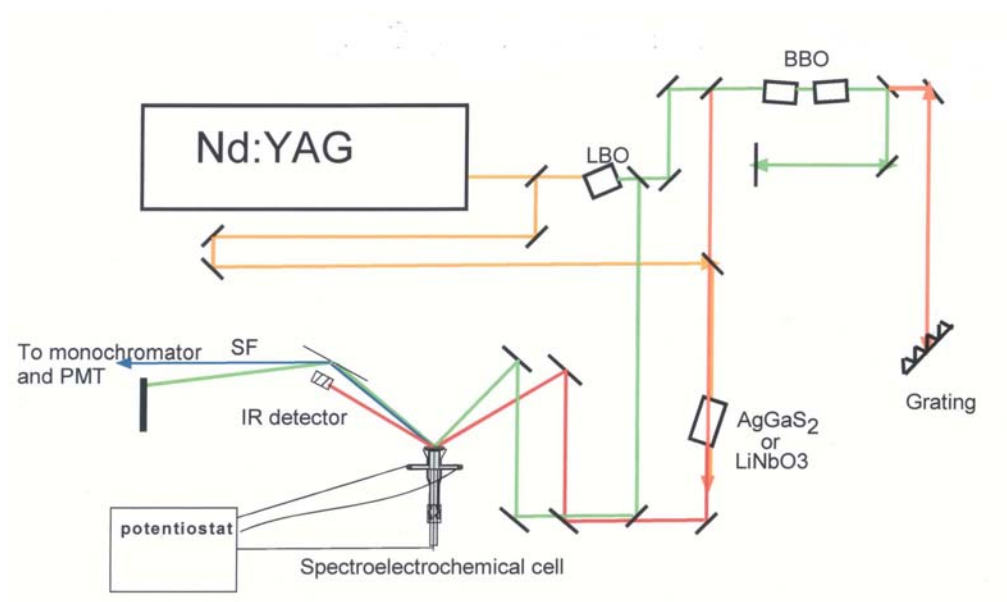


Figure 2.11. Schematic of sum frequency generation vibrational spectroscopy system, showing beam generation, amplification, mixing, and detection.

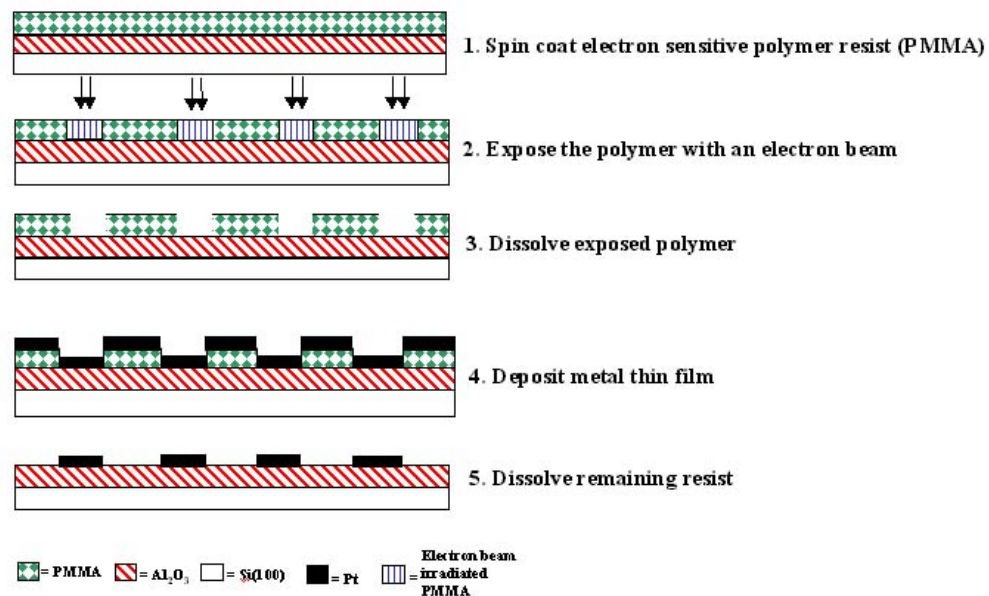


Figure 2.12. Electron beam lithography process for the production of oxide-supported metal nanoparticles.

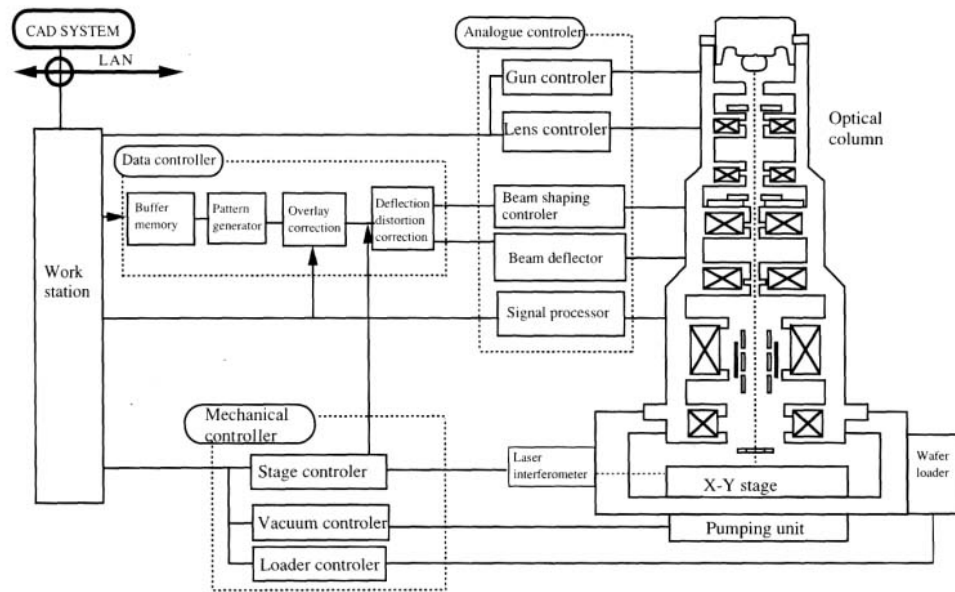


Figure 2.13. Schematic of electron beam lithography system. The optical column for EBL and SEM are identical.

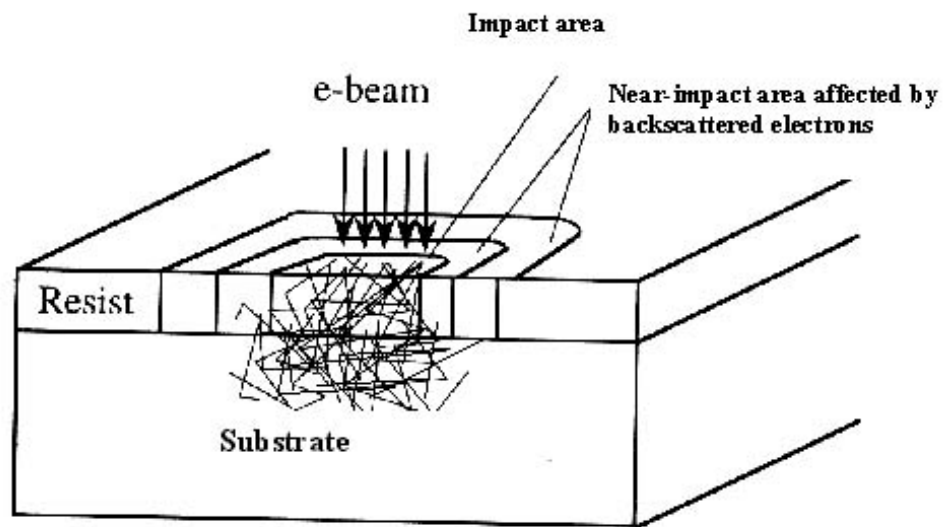


Figure 2.14. Proximity effect as seen in electron beam lithography.

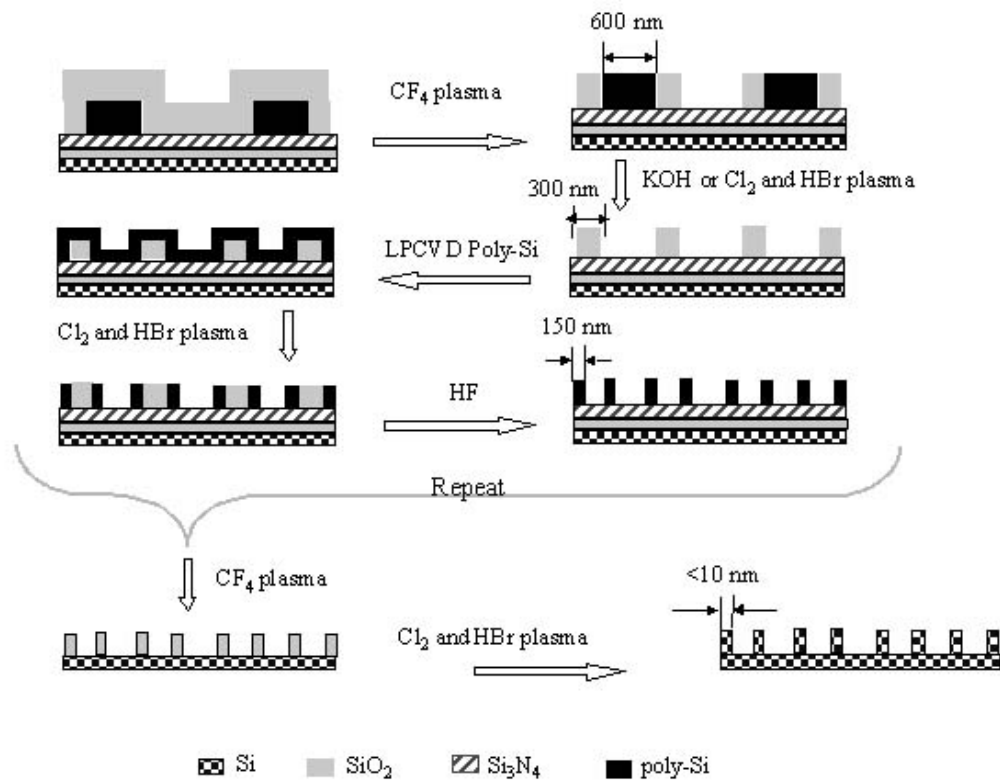


Figure 2.15. Size reduction lithography process. For an increase in pattern density, multiple size reduction lithography can be employed.

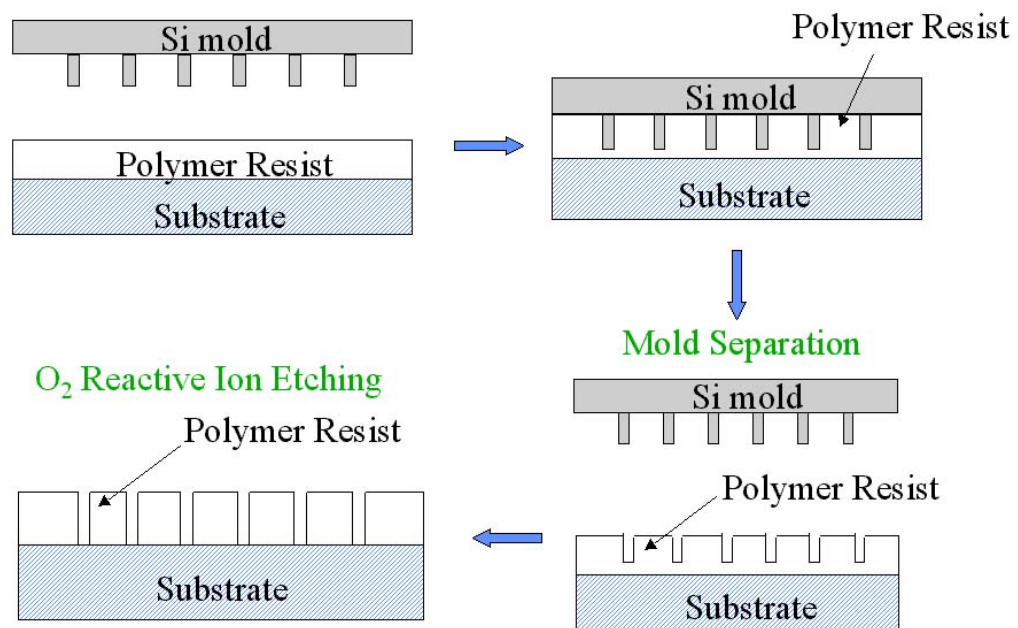


Figure 2.16. Principle steps of nanoimprint lithography.

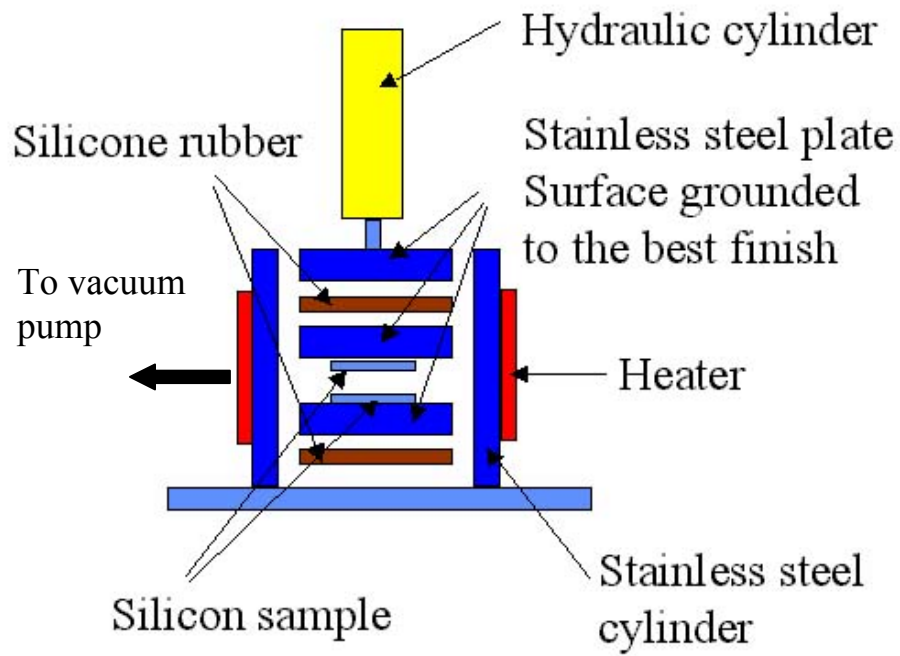


Figure 2.17. Schematic of home-built nanoimprint lithography press, showing the hydraulic cylinder, vacuum, heater, and pressing plates.

References

-
- ¹ Hoffman, D.M.; Singh, B.; Thoms, J.III, *Handbook of Vacuum Science and Technology*. Academic Press, San Diego, 1998.
- ² Roth, A. *Vacuum Technology*, 2nd edition, North-Holland, Amsterdam, 1982.
- ³ Redhead, P.A.; Hobson, J.P.; Kornelsen, E.V. *The Physical Basis of Ultrahigh Vacuum*. Chapman and Hall, London, 1968.
- ⁴ O'Hanlon, J.F. *A User's Guide to Vacuum Technology*. John Wiley & Sons, New York, 1980.
- ⁵ Roberts, R.W.; Vanderslice, T.A. *Ultrahigh Vacuum and its Applications*. Prentice Hall, New Jersey, 1963.
- ⁶ Somorjai, G.A. *Chemistry in Two Dimensions: Surfaces*, Cornell University Press, Ithaca, New York, 1981.
- ⁷ Somorjai, G.A. *Introduction to Surface Chemistry and Catalysis*. John Wiley & Sons, New York, 1994.
- ⁸ Thompson, M. *Auger Electron Spectroscopy*. John Wiley & Sons, New York, 1985.
- ⁹ Ertl, G.; Kuppers, J. *Low Energy Electrons and Surface Chemistry*. Verlag-Chemie, Germany, 1974.
- ¹⁰ Weissmann, R.; Muller, K. *Surf. Sci. Rep.* **1981**, 105, 251.
- ¹¹ Auger, P., *J. Phys. Radium* **1925**, 6, 205.
- ¹² Tharp, L.N.; Scheibner, E.J., *J. Appl. Phys.* **1967**, 38, 4355.
- ¹³ Davis, L.E.; MacDonald, N.C.; Palmberg, P.W.; Riach, G.E.; Weber, R.E., eds. *Handbook of Auger Electron Spectroscopy*, 2nd edition, Physical Electronics Inc., Eden Prairie, MN, 1976.

-
- ¹⁴ Somorjai, G.A., *Proc. Exxon Corp. Conf.*, Linden, New Jersey, 1980.
- ¹⁵ Niemantsverdriet, J.W. *Spectroscopy in Catalysis*. Wiley-VCH, Germany, 2000.
- ¹⁶ Needham, P.B.; Driscoll, T.J.; Rao, N.G. *Appl. Phys. Lett.* **1972**, *21*, 502.
- ¹⁷ Briggs, D.; Seah, M.P. *Practical Surface Analysis: Auger and X-ray Photoelectron Spectroscopy*. John Wiley & Sons, New York, 1996.
- ¹⁸ Carlson, T.A. *Photoelectron and Auger Spectroscopy*. Plenum Press, New York, 1975.
- ¹⁹ Feuerbacher, B.; Fitton, B.; Willis, R.F. *Photoemission and the Electronic Properties of Surfaces*. John Wiley & Sons, New York, 1978.
- ²⁰ Moulder, J.F.; Stickle, W.F.; Sobol, P.E.; Bomben, K.D. *Handbook of X-ray Photoelectron Spectroscopy*. Physical Electronics Inc., Eden Prairie, Minnesota, 1995.
- ²¹ Briggs, D., ed. *Handbook of X-Ray and Ultraviolet Photoelectron Spectroscopy*. Heyden, London, 1978.
- ²² Einstein, A. *Ann. Phys. (Leipzig)* **1905**, *17*, 132.
- ²³ Binnig, G.; Rohrer, H. *Helvetica Physica Acta* **1982**, *55*, 726.
- ²⁴ Binnig, G.; Quate, C.F.; Gerber, C. *Appl. Phys. Lett.* **1982**, *40*, 178.
- ²⁵ Binnig, G.; Quate, C.F.; Geber, C. *Phys. Rev. Letters* **1986**, *56*, 930.
- ²⁶ Dror, S. *Scanning Force Microscopy: With Application to Electric, Magnetic and Atomic Forces*. Oxford University Press, New York, 1994.
- ²⁷ Israelachvili, J. *Intermolecular & Surface Forces*. Academic Press, London, 1997.
- ²⁸ Hamaker, H.C. *Physica* **1937**, *4*, 1058.
- ²⁹ Hertz, H. *J. Reine Angew. Math.* **1881**, *92*, 156.
- ³⁰ Johnson, K.L.; Kendall, K.; Roberts, A.D. *Proc. R. Soc. Lond. A.* **1971**, *324*, 301.
- ³¹ Derjaguin, B.V.; Muller, V.M.; Toporov, Y.P. *J. Coll. Inter. Sci.* **1975**, *67*, 314.

-
- ³² Flegler, S.L.; Heckman, J.W.; Klomparens, K.L. *Scanning and Transmission Electron Microscopy: An Introduction*. Oxford University Press, New York, 1993.
- ³³ Hayat, M.A. *Principles and Techniques of Scanning Electron Microscopy*. Van Nostrand Reinhold, New York, 1974.
- ³⁴ Goldstein, J.I.; Newbury, D.E.; Echlin, P.; Joy, D.C.; Romig, A.D.; Lyman, C.E.; Fiori, C.; Lifshin, E. *Scanning Electron Microscopy and X-Ray Microanalysis: A Text for Biologists, Materials Scientists, and Geologists*. 2nd edition, Plenum Press, New York, 1992.
- ³⁵ Koshikawa, T.; Shimizu, R. *J. Phys. D.* **1974**, 7, 1303.
- ³⁶ Knoll, M.; Ruska, E. *Z. Physik* **1932**, 78, 318.
- ³⁷ Poppa, H. *Catal. Rev.-Sci. Eng.* **1993**, 35, 359.
- ³⁸ Davenas, J.; Rabette, P.M., eds. *Contributions of Clusters Physics to Materials Science and Technology: From Isolated Clusters to Aggregated Materials*. Kluwer, Dordrecht, Germany, 1986.
- ³⁹ Jose-Yacaman, M.; Avalos-Borja, M. *Catal. Rev.-Sci. Eng.* **1992**, 34, 55.
- ⁴⁰ Cowley, J.M. *Prog. Surf. Sci.* **1986**, 21, 209.
- ⁴¹ Thomas, G. *Ultramicroscopy*. **1986**, 20, 239.
- ⁴² Williams, D.B.; Carter, C.B. *Transmission Electron Microscopy: A Textbook for Materials Science*. Plenum Press, New York, 1996.
- ⁴³ Flegler, S.L.; Heckman, J.W.; Klomparens, K.L. *Scanning and Transmission Electron Microscopy: An Introduction*. Oxford University Press, New York, 1997.
- ⁴⁴ de Graef, M. *Introduction to Conventional Transmission Electron Microscopy*. Cambridge University Press, New York, 2003.

-
- ⁴⁵ Ashcroft, N.W.; Mermin, N.D.; Mermin, D. *Solid State Physics*. Holt, Rinehart and Winston, New York, 1976.
- ⁴⁶ Fultz, B.; Howe, J.; Caenepeel, S.M. *Transmission Electron Microscopy and Diffractometry of Materials*. 2nd edition, Springer Verlag, New York, 2002.
- ⁴⁷ Shen, Y. R., *Principles of Nonlinear Optics*, John Wiley & Sons, New York, 1984.
- ⁴⁸ Wei, X.; Hong, S. C.; Zhuang, X. W.; Goto, T.; Shen, Y. R. *Phys. Rev. E* **2000**, *62*, 5160.
- ⁴⁹ Shen, Y.R. *Nature* **1989**, *337*, 519.
- ⁵⁰ Corn, R.M. *Anal. Chem.* **1991**, *63*, 285.
- ⁵¹ Miranda, P. B.; Shen, Y. R. *J. Phys. Chem. B* **1999**, *103*, 3292.
- ⁵² Zhuang, X.; Miranda, P. B.; Kim, D.; Shen, Y. R. *Phys. Rev. B* **1999**, *59*, 12632.
- ⁵³ Hirose, C.; Akamatsu, N.; Domen, K. *Appl. Spect.* **1992**, *46*, 1051.
- ⁵⁴ Hirose, C.; Yamamoto, H.; Akamatsu, N.; Kazunari, D. *J. Phys. Chem.* **1993**, *97*, 10064.
- ⁵⁵ Akamatsu, N.; Domen, K.; Hirose, C. *J. Phys. Chem.* **1993**, *97*, 10070.
- ⁵⁶ Hirose, C.; Akamatsu, N.; Domen, K. *J. Chem. Phys.* **1992**, *96*, 997.
- ⁵⁷ Dick, B. *Chem. Physics* **1985**, *96*, 199.
- ⁵⁸ Bain, C.D. *J. Chem. Soc. Faraday Trans.* **1995**, *91*, 1281.
- ⁵⁹ Franken, P.A.; Hill, A.E.; Peters, C.W.; Weinreich, G. *Phys. Rev. Lett.* **1961**, *7*, 118.
- ⁶⁰ Armstrong, J.A.; Bloembergen, N.; Ducuing, J.; Pershan, P.S. *Phys. Rev.* **1962**, *127*, 1918.
- ⁶¹ Bloembergen, N.; Pershan, P.S. *Phys. Rev.* **1962**, *128*, 606.
- ⁶² Simon, H.J.; Mitchell, D.E.; Watson, J.G. *Phys. Rev. Lett.* **1974**, *33*, 1531.

-
- ⁶³ Zhu, X.D.; Suhr, H.; Shen, Y.R. *Phys. Rev. B* **1987**, *35*, 3047.
- ⁶⁴ Moore, G.E. *Electronics* **1965**, *38*, 114.
- ⁶⁵ Timp, G. *Nanotechnology*. Springer-Verlag, New York, 1999.
- ⁶⁶ Kolasinski, K. *Surface Science: Foundations of Catalysis and Nanoscience*. John Wiley & Sons, New York, 2002.
- ⁶⁷ Feynman, R.P.; *Engineering and Science*, February 1960, 22.
- ⁶⁸ Zhou, B.; Hermans, S.; Somorjai, G.A., eds. *Nanotechnology in Catalysis*. Kluwer Academic, New York, 2003.
- ⁶⁹ Xia, Y.; Rogers, J.A.; Paul, K.E.; Whitesides, G.M. *Chem. Rev.* **1999**, *99*, 1823.
- ⁷⁰ Liang, W.J.; Shores, M.P.; Bockrath, M.; Long, J.R.; Park, H.K. *Nature* **2002**, *417*, 725.
- ⁷¹ Puentes, V.F.; Krishnan, K.M.; Alivisatos, A.P. *Science* **2001**, *291*, 2115.
- ⁷² Sun, S.H.; Murray, C.B.; Weller, D.; Folks, L.; Moser, A. *Science* **2000**, *287*, 1989.
- ⁷³ Huang, M.H.; Mao, S.; Feick, H.; Yan, H.Q.; Wu, Y.Y.; Kind, H.; Weber, E.; Russo, R.; Yang, P.D. *Science* **2001**, *292*, 1897.
- ⁷⁴ Ingber, D.E. *Proc. Natl. Acad. Sci. U.S.A.* **1990**, *87*, 3579.
- ⁷⁵ Chen, C.S.; Mrksich, M.; Huang, S.; Whitesides, G.M.; Ingber, D.E. *Science* **1997**, *276*, 1425.
- ⁷⁶ Chen, C.S.; Mrksich, M.; Huang, S.; Whitesides, G.M.; Ingber, D.E. *Biotechnol. Prog.* **1998**, *14*, 356.
- ⁷⁷ Liu, G.Y.; Xu, S.; Qian, Y.L. *Acc. Chem. Res.* **2000**, *33*, 457.
- ⁷⁸ Douglas, K.; Clark, N.A.; Rothschild, K.J. *Appl. Phys. Lett.* **1990**, *56*, 692.
- ⁷⁹ Pileni, M.P. *Langmuir* **1997**, *13*, 3266.

-
- ⁸⁰ Xia, Y.; Whitesides, G.M. *Angew. Chem. Int. Ed.* **1998**, *37*, 550.
- ⁸¹ Goldberg, K.A.; Naulleau, P.; Bokor, J.; Chapman, H.N.; Barty, A. *J. Vac. Sci. Tech. B* **2002**, *20*, 2834.
- ⁸² Mitan, M.M.; Pivin, D.P.; Alford, T.L.; Mayer, J.W. *Thin Solid Films* **2002**, *411*, 219.
- ⁸³ Liang, T.; Stivers, A.; Livengood, R.; Yan P.Y.; Zhang, G.J.; Lo, F.C. *J. Vac. Sci. Tech. B* **2000**, *18*, 3216.
- ⁸⁴ Chou, S.Y.; Krauss, P.R.; Renstrom, P.J. *Appl. Phys. Lett.* **1995**, *67*, 3114.
- ⁸⁵ Chou, S.Y.; Krauss, P.R.; Renstrom, P.J. *Science* **1996**, *272*, 85.
- ⁸⁶ Liu, G.Y.; Xu, S.; Qian, Y.L. *Acc. Chem. Res.* **2000**, *33*, 457.
- ⁸⁷ Hulteen, J.C.; Van Duyne, R.P. *J. Vac. Sci. Tech. B* **1995**, *13*, 1553.
- ⁸⁸ Whitesides, G.M.; Mathias, J.P.; Seto, C.T. *Science* **1991**, *254*, 1312.
- ⁸⁹ Dolan, G.J. *Appl. Phys. Lett.* **1977**, *31*, 337.
- ⁹⁰ Kramer, N.; Birk, H.; Jorritsma, J.; Schonenberger, C. *Appl. Phys. Lett.* **1995**, *66*, 1325.
- ⁹¹ Dagata, J.A. *Science* **1995**, *270*, 1625.
- ⁹² Becker, R.S.; Golovchenko, J.A.; Swartzentruber, B.S. *Nature* **1987**, *325*, 419.
- ⁹³ Heinrich, A.J.; Lutz, C.P.; Gupta, J.A.; Eigler, D.M. *Science* **2002**, *298*, 1381.
- ⁹⁴ Sheehan, P.E.; Lieber, C.M. *Science* **1996**, *272*, 1158.
- ⁹⁵ Betzig, E.; Trautman, K. *Science* **1992**, *257*, 189.
- ⁹⁶ Campbell, S.A. *The Science and Engineering of Microelectronic Fabrication*. 2nd edition, Oxford University Press, New York, 2001.
- ⁹⁷ Brodie, I.; Muray, J.J. *The Physics of Micro/Nano-Fabrication*. Plenum Press, New York, 1992.
- ⁹⁸ Nishi, Y.; Doering, R. *Handbook of Semiconductor Manufacturing Technology*. Marcel

-
- Dekker, New York, 2000.
- ⁹⁹ Van Zant, P. *Microchip Fabrication: A Practical Guide to Semiconductor Processing*. 4th edition, McGraw-Hill, New York, 2000.
- ¹⁰⁰ Quirk, M.; Serda, J. *Semiconductor Manufacturing Technology*. Prentice Hall, New Jersey, 2001.
- ¹⁰¹ Madou, M.J. *Fundamentals of Microfabrication: The Science of Miniaturization*. 2nd edition, CRC Press, New York, 2002.
- ¹⁰² Haller, I.; Hatzakis, M.; Srinivasan, R. *IBM J. Res. Develop.* **1968**, 12, 251.
- ¹⁰³ Chang, T.H.P. *J. Vac. Sci. Technol.* **1975**, 12, 1271.
- ¹⁰⁴ Owen, G.; Chang, T.H.P. *J. Vac. Sci. Technol. B* **1990**, 8, 1889.
- ¹⁰⁵ Chang, T.H.P. *SPIE Proc.* **1993**, 1924, 114.
- ¹⁰⁶ Harriott, L.; Liddle, A. *Physics World*, April 1997, 41.
- ¹⁰⁷ Chen, W.; Ahmed, H. *Appl. Phys. Lett.* **1993**, 62, 1499,
- ¹⁰⁸ Craighead, H.G.; Howard, R.E.; Jackel, L.D.; Mankievich, P.M. *Appl. Phys. Lett.* **1983**, 42, 38.
- ¹⁰⁹ Dial, O.; Cheng, C.C.; Scherer, A. *J. Vac. Sci. Technol. B* **1998**, 16, 3887.
- ¹¹⁰ Chen, W.; Ahmed, H. *J. Vac. Sci. Technol. B* **1993**, 11, 2519.
- ¹¹¹ Cumming, D.R.S.; Thoms, S.; Beaumont, S.P.; Weaver, J.M.R. *Appl. Phys. Lett.* **1996**, 68, 322.
- ¹¹² Vieu, C.; Carcenac, F.; Pepin, A.; Chen, Y.; Mejias, M.; Lebib, A.; Manin-Ferlazzo, L.; Couraud, L.; Launois, H. *Appl. Surf. Sci.* **2000**, 164, 111.
- ¹¹³ Brandrup, J.; Immergut, E.H.; Grulke, E.A., eds. *Polymer Handbook*. John Wiley & Sons, New York, 1989.

-
- ¹¹⁴ Cui, C.Y.; Wei, Q.Q.; Park, H.K.; Lieber, C.M. *Science* **2001**, *293*, 1289.
- ¹¹⁵ Piner, R.D.; Zhu, J.; Xu, F.; Hong, S.H.; Mirkin, C.A. *Science* **1999**, *283*, 661.
- ¹¹⁶ Cronin, J.E.; Kaanta, C.W. US Patent 5,795,830.
- ¹¹⁷ Yu, Z.; Wu, W.; Chen, L.; Chou, S.Y. *J. Vac. Sci. Tech. B* **2001**, *19*, 2816.
- ¹¹⁸ Cherniavskaya, O.; Adzic, A.; Knutson, C.; Gross, B.J.; Zang, L.; Liu, R.; Adams, D.M. *Langmuir* **2002**, *18*, 7029.
- ¹¹⁹ Choi, Y.K.; King, T.J.; Hu, C. *IEEE Trans. Electron Devices* **2002**, *49*, 436.
- ¹²⁰ Choi, Y.K.; King, T.J.; Hu, C. *IEEE Electron Device Lett.* **2002**, *23*, 25.
- ¹²¹ Choi, Y.K.; King, T.J.; Hu, C. *Solid State Electronics* **2002**, *46*, 1595.
- ¹²² Wu, W.; Cui, B.; Sun, X.-Y.; Zhang, W.; Zhuang, L.; Kong, L.; Chou, S.Y. *J. Vac. Sci. Technol. B* **1998**, *16*, 3825.
- ¹²³ Chou, S.Y.; Krauss, P.R.; Renstrom, P.J. *J. Vac. Sci. Technol. B* **1996**, *14*, 4129.
- ¹²⁴ Zankovych, S.; Hoffmann, T.; Seekamp, J.; Bruch, J.-U.; Sotomayor Torres, C.M. *Nanotechnology* **2001**, *12*, 91.
- ¹²⁵ Chou, S.Y.; Krauss, P.R.; Zhang, W.; Guo, L.; Zhuang, L. *J. Vac. Sci. Technol. B* **1997**, *15*, 2897.
- ¹²⁶ Tan, H.; Gilbertson, A.; Chou, S.Y. *J. Vac. Sci. Technol. B* **1998**, *16*, 3926.
- ¹²⁷ Marrian, C.; Chou, S.Y., eds. *Proc. First International Conference on Nanoimprint Nanoprint Technology*, San Francisco, California, Dec. 11-13, 2002.
- ¹²⁸ Marrian, C.; Chou, S.Y., eds. *Proc. Second International Conference on Nanoimprint Nanoprint Technology*, Boston, Massachusetts, Dec. 3-5, 2003.

Chapter 3

Atomic Force Microscopy (AFM) and Transmission Electron Microscopy (TEM) Studies of Alumina-Supported Pt Nanoparticle Array Model Catalysts Prepared by Electron Beam Lithography

3.1 Introduction

Most heterogeneous industrial catalysts are made of highly dispersed metal nanoparticles (usually with diameters of 1-100 nm) supported on porous silica, alumina, zeolite, or other oxides. Metal is introduced on the support from solution by impregnation, adsorption, ion-exchange, or co-precipitation.¹ The resultant product is an

intricate 3-D network of randomly distributed metal particles with a range of particle size distribution inside the oxide pores. Catalytic properties often depend on particle size², oxide support³, and the interaction between the metal and the support⁴, etc. Metal single crystals have proven to be good models for correlating surface structure and catalysis due to several favorable characteristics. The metal single crystals are flat, conducting, and structurally well defined, making them accessible to the whole arsenal of surface science techniques, which primarily include electron and photon interactions with the surface and adsorbates. Secondly, it is relatively easy to produce atomically clean surfaces as defined by Auger electron spectroscopy. Thirdly, metal single crystals have high stability in the reducing ultrahigh vacuum environment and can sustain thousands of sputtering/annealing cleaning cycles. Lastly, single crystals with enough surface area (on the order of 1 cm²) can be prepared, which enables the study of a wide range of catalytic reactions with turnover frequencies ranging from 1 molecules/site/s for facile reactions to $\leq 10^{-4}$ molecule/site/s for demanding, more complex reactions.⁵ Decades of studies on single crystal surfaces have yielded crucial information concerning chemisorption, the relationship between surface structure and catalysis, and promoter-metal interactions, all of which greatly enhance our understanding and provide insights into the heterogeneous catalytic process.

However, metal single crystals as model catalysts have their own limitations: the oxide support is absent and they do not well-represent the metal nanoclusters that may exhibit changes in electronic structure associated with the reduced dimensions of metal particles with diameters of 2 nm or less.⁶ Therefore, there is an urgent need to develop a well-defined model catalyst system to elucidate the interplay between the parameters that

control catalytic properties. The planar geometry of a 2-D model system should make it more accessible for studies by surface science techniques.⁷ Several methods have been utilized to prepare 2-D model nanoparticle catalysts, including laser ablation⁸, spin-coating of a metal salt solution on an oxide support followed by calcinations⁹, evaporation of metal onto an oxide support¹⁰, soft landing of size-selected clusters on a planar support^{11, 12}, laser interference nanolithography¹³, photolithography¹⁴, and electron beam lithography^{15, 16, 17, 18}, to name a few. Compared with other methods, lithography methods have the advantage of precise control over particle size and interparticle spacing. In addition, the lithographic approach is not dependent on specific materials, which makes it possible to fabricate catalysts with a wide range of metals and support materials. Of all the available lithography methods, electron beam lithography has the highest resolution with a minimum diameter of 10 nm and interparticle distance of 50 nm. This makes EBL the best option for fabricating model catalysts that mimic the industrial catalyst. By changing the size of the particles in the relevant regime, size effects on catalytic activity can be investigated. The metal-support interaction can also be studied in a more controlled way by systematically varying the support materials. Electron beam lithography is a low throughput serial process, whose minimum feature size is limited by backscattered electrons. As stated in the previous chapter, the rapid advance of parallel lithography options such as nanoimprint lithography^{19, 20} and improved developing procedures for electron beam lithography²¹, it is possible to mass-produce regular, large-area, sub-10 nm nanoparticle arrays. However, the thermal, chemical, and mechanical stability of the supported nanoparticle arrays will determine their usefulness as model catalysts. Previous studies showed that Pt nanoparticle arrays supported on silica had

high thermal, chemical, and mechanical stability, and were therefore suited for catalysis studies.²² This work extended the studies to Pt nanoparticle arrays supported on alumina. The results showed increased bonding between the Pt nanoparticles supported on alumina upon heat treatment.

3.2 Experimental

3.2.1 Electron Beam Lithography (EBL)

The nanoparticle arrays were fabricated using electron beam lithography. The electron beam lithography is conducted on a Leica Nanowriter machine. A scheme of the process was shown in Chapter 2 (Figure 2.12). In short, a thin layer of 350K PMMA (polymethylmethacrylate) was spin-coated onto a Si(100) wafer that was coated with a 30-nm Al_2O_3 film on the surface using ion-assisted electron beam evaporation (Cascade Optical Inc). A computer-designed square pattern was then “written” into the polymer layer with a highly collimated electron beam generated by a field emission source. With a beam current of 600 pA and an accelerating voltage of 100 kV, the beam diameter was approximately 3 nm. A dose of $2500 \mu\text{C}/\text{cm}^2$ was used to expose the PMMA, resulting in a dwell time of $\sim 6 \mu\text{s}$ at each particle site. After dissolving the exposed polymer, a 15-nm Pt film was then vacuum deposited on the surface through the polymer mask by electron beam evaporation, using a quartz crystal thickness monitor. The wafer was kept at room temperature during the deposition by water-cooling the sample holder. Finally, the remaining resist was removed by dissolution in acetone, leaving the metal particles of the prescribed pattern on the substrate. Metal particle size can be changed by rastering

the electron beam to the desired size. The smallest particle size is produced by point exposure, which was 28 nm. This minimum feature size was due to back-scattering broadening. The interparticle distance is defined by the computer-designed pattern; the lower limit on the interparticle distance is determined by the proximity effect and is 50 nm under our conditions. With this high degree of spatial resolution, 36 mm² arrays with approximately 10⁹ particles were produced in the time period of several hours. The resulting Pt nanoparticle arrays were examined with a Philips CM200FEG/UT transmission electron microscope (TEM), JEOL 200 field emission scanning electron microscope (FESEM), and a Park Scientific Instrument M5 atomic force microscope (AFM).

Two different samples were prepared and used in the experiment. One sample had an interparticle distance of 100 nm and was heated in vacuum at 500°C for 3 hours; the other had an interparticle distance of 150 nm and was used as prepared. The diameter of the nanoparticles on both samples was (28 ± 2) nm. The difference in interparticle distance was not considered to affect the adhesion between the metal and oxide interface.

3.2.2 Transmission Electron Microscopy (TEM)

TEM samples were prepared following the procedures outlined in Figure 3.1. The EBL-fabricated sample was mounted to a glass slide with crystal bond, with the array facing the slide. A 3-mm diameter disk was cut from the sample using an ultrasonic disk cutter (Gatan). The sample was then thinned mechanically using a polisher (Minimet) to 200 µm thickness and then to near optical transparent with a dimpler (VCR). The dimpler milled a convex hole on the backside of the sample, making the center of the

sample the thinnest part. Finally, ion milling with 1.5 kV Ar⁺ sputtering at a 15° angle created a hole in the center of the sample, with the area around the hole thin enough to be electron transparent.

3.2.3 Atomic Force Microscopy (AFM)

The arrays were cleaned by flowing dry nitrogen before taking measurements with AFM in an ambient environment. Either changing the set point or using tips with different force constants varied the applied forces. Both contact and non-contact Si cantilevers purchased from Silicon-MDT Ltd. were used in contact mode. The contact cantilevers were SC12 Series Type C with a typical force constant of 0.6 N/m and a range between 0.15 N/m and 1.5 N/m; the non-contact cantilevers were SC11 Series Type B with a typical force constant of 48 N/m and a range between 23 N/m and 91 N/m. The maximum set point, determined by the data acquisition software (PSI ProScan v. 1.51), was around 30 nN for the contact cantilevers and around 4000 nN for the non-contact cantilevers. The force constants of the tips were not determined experimentally; typical values reported by the manufacturer were used.

3.3 Results and Discussion

3.3.1 Characterization

As shown in Figure 3.2, AFM images taken at low load (15 nN) showed few displaced particles. The height of the nanoparticles was 15 nm and the spacing was 150 nm. The particle size obtained on the AFM image was a result of convolution between

the Pt nanoparticle geometry and the AFM tip size and shape. Deconvolution techniques can be used to extract information about the particle size and the tip radius. Since particle sizes were measured more accurately by FESEM and TEM, deconvolution techniques were not applied here. FESEM examination of the Pt nanoparticle arrays showed that the nanoparticles have a diameter of (28 ± 2) nm and an interparticle spacing of 150 nm. TEM studies further confirmed the dimensions.

High-resolution TEM studies revealed the polycrystalline nature of as-prepared samples, with an average crystallite dimension of about 5 nm (Figure 3.3a). After heat treatment of 500°C for 3 hours in an UHV chamber with a base pressure of 5×10^{-10} torr, some of the nanoparticles annealed to single crystals; most of the nanoparticles maintained their polycrystalline morphology, but the number of crystal domains was reduced to 2-3 and the average crystallite domain increased significantly (Figure 3.3b). The results were similar to a previous study²² of Pt deposited on SiO₂, where the average crystalline domain size was 3-6 nm before any heat treatment and grew larger after heat treatment in a variety of gas environments. The crystalline domain increase was attributed to Pt self-diffusion.

3.3.2 Adhesion

On an as-prepared sample, the particles were displaced with a normal force of about 30 nN, as shown in Figure 3.4. Initial scans at a set point of 25 nN revealed a square array of Pt nanoparticles with a spacing of 150 nm (Figure 3.4a). Some particles were missing from the pattern; they were lost either during the liftoff procedure in the fabrication process or being displaced due to their weaker bonding to the alumina surface.

As the set point increased from 25 nN to 31 nN (Figures 3.4b-3.4e), more and more particles were gradually removed from the pattern. There were still some particles remaining on the surface after two consecutive scans at 31 nN, which was the highest set point prescribed by the software. In the last image, the scan area was enlarged to $2 \times 2 \mu\text{m}^2$ to show the area of displaced particles and the surrounding area, which was unaffected due to a lower set point. The displacement force depended on the scanning speed, and it increased from 12 nN to 30 nN as the scanning speed increased from $2 \mu\text{m/s}$ (1 Hz) to $3 \mu\text{m/s}$ (1.5 Hz). This may be attributed to the decreased interaction time between the tip and the particle at faster speeds. Upon heating in the UHV chamber at 500°C , the adhesion between the nanoparticles and the alumina surface had increased dramatically. The AFM image acquired by operating a non-contact cantilever in contact mode with a set point of 4000 nN showed no missing particles, as shown in Figure 3.5. The increased adhesion between the Pt nanoparticles and the oxide support indicated an increased interaction between the Pt nanoparticles and the oxide.

The actual forces acting on the nanoparticles were not quantified since this involved detailed characterization of the normal and lateral cantilever force constants for every tip, a thorough knowledge of its geometry, the deflection sensor response, the tip structure, and the composition at the tip-surface contact.²³ However, it is possible to put some reasonable limits on the adhesion between the Pt nanoparticles and the alumina support using the model put forth by Eppler *et al.*²² The lateral force can be shown to depend on the friction coefficient and the slope of the tip; the lateral force can be approximated by the normal load. Assuming the distance needed to break the metal-oxide bonding is 1 \AA , the interfacial energy for an as-prepared sample, whose particles

were displaced at 30 nN of normal load, is calculated to be 5 mJ/m². The lower limit of interfacial energy for the heat-treated sample is estimated to be 0.65 J/m², using the same assumption. The calculation above gave an order of magnitude estimation of the work of adhesion.

The adhesion between metal and oxide is of great technological importance, but difficult to quantify. The adhesion of bulk metal and oxide at near or above metal melting temperatures can be studied by sessile drop experiments.²⁴ At low temperatures, especially room temperature, the adhesion between thin metal films and an oxide can be qualitatively evaluated by a scotch tape test and scratch test. But a general method for investigating metal nanoparticle adhesion onto an oxide has yet to be found. Particle density at saturation²⁵ and particle shape^{25, 26} have been used to evaluate the work of adhesion of Au and Pd on alumina. However, these methods are not direct and are sensitive to initial assumptions. AFM offers the opportunity to study the adhesion directly, but most of the adhesion studies to-date are performed using pull-off forces applied in the normal direction.²⁷ This work is the first attempt to study adhesion in the lateral direction.

Work of adhesion between the metal and oxide depends on the environment in which the metal support interface is established, the cleanliness of the oxide surface, and the morphology of the metal particles. The adhesion energy between metal and oxide is generally on the order of 1 J/m². For example, the adhesion of Au²⁵ and Pd²⁶ nanoparticles on Al₂O₃ is 1.32–1.6 J/m² and 2.8 J/m², respectively; the adhesion between W and TiO₂ is 0.7–0.8 J/m².²⁷ Therefore, the adhesion energy, with a lower limit of 0.65 J/m² for the heat-treated sample, qualitatively agrees with the literature value; but, the

estimated value of 5 mJ/m^2 for Pt nanoparticles freshly deposited on Al_2O_3 is two orders of magnitude smaller. The discrepancy can be attributed to the condition under which the metal oxide interface interaction is established. There are two possible mechanisms based on the fact that the Pt nanoparticle are made by electron beam deposition of Pt into a mask pattern on an alumina-coated Si wafer in 1×10^{-5} torr vacuum. First, the alumina surface may contain a layer of adsorbed hydrocarbon molecules, which will adversely affect the adhesion between Pt and alumina. In fact, the surface energies of most organic liquids²⁸ are on the order of 20 mJ/m^2 , which agrees with our estimated value of 5 mJ/m^2 , given the uncertainties in the estimation. Upon heating to 500°C , the hydrocarbon molecules can decompose to carbonaceous deposits under the catalytic action of Pt. It is known that the interaction energy between the metal and carbon is greater than with the oxide support¹; therefore, the increased adhesion could be attributed to the decomposition of an adsorbed hydrocarbon layer, which acts as a carbon glue. Second, the deposited Pt may contain voids and grain boundaries, which will decrease the number of Pt atoms at the metal-oxide interface, thus decreasing the adhesion. Annealing at high temperatures caused Pt atom motion in the nanoparticles and helped establish an intimate metal-oxide interface, resulting in an increase in the adhesion. Both mechanisms are feasible and further experiments are needed to distinguish between them.

3.4 Conclusion

In summary, alumina-supported Pt nanoparticle arrays fabricated by electron beam lithography showed stronger bonding with the support and larger crystallite domains upon heating. This was in excellent agreement with previous studies on silica-

supported Pt nanoparticle arrays. The increased adhesion of Pt nanoparticle to the support signifies a stronger influence of the support on the Pt nanoparticle, which may show up as support dependence of catalytic properties. The activity and selectivity of these alumina-supported Pt nanoparticle arrays was probed via catalytic reactions and is presented in the next chapter.

TEM Sample Preparation

- I. Glue array, face down, to glass slide. Glue=crystal bond, 180 C.



- II. Cut 3 mm diameter disk from wafer with ultrasonic cutter



- III. Remelt crystal bond, remove disk and mount to another glass slide (also face down).

- IV. Grind back side to 200 μ m thickness with 30 μ m grit.

- V. "Dimple" - make convex hole in back side to 1 μ m in center.



- VI. Ion sputter at 15 degree angle as sample rotates (1.5 kV).

Electron transparent near center.

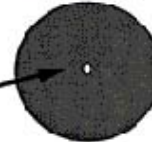


Figure 3.1. Schematic drawing of TEM sample preparation.

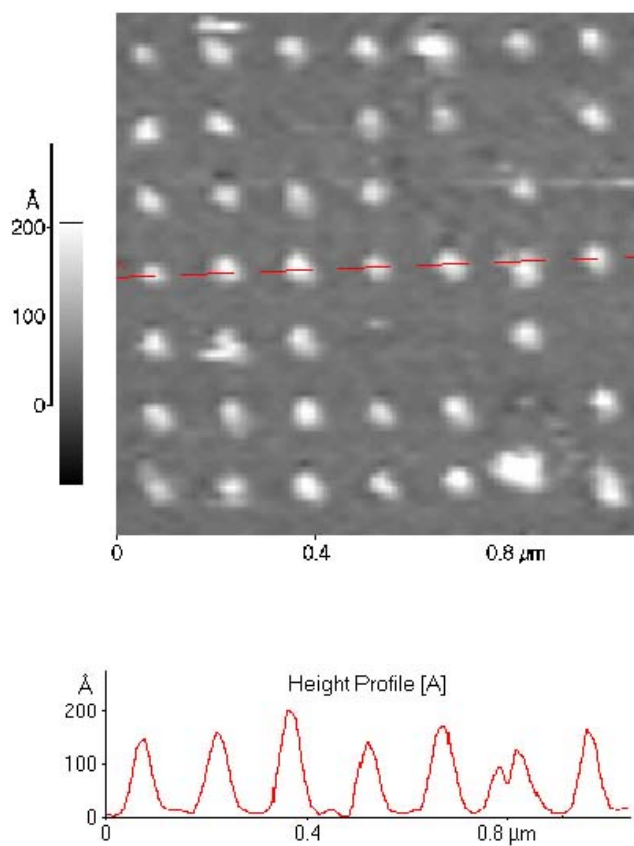


Figure 3.2. AFM image of Pt nanoparticle arrays. The height is 15 nm and the periodicity is 150 nm. The particle appears to be larger than 28 nm because of the convolution between the AFM tip and the nanoparticles.

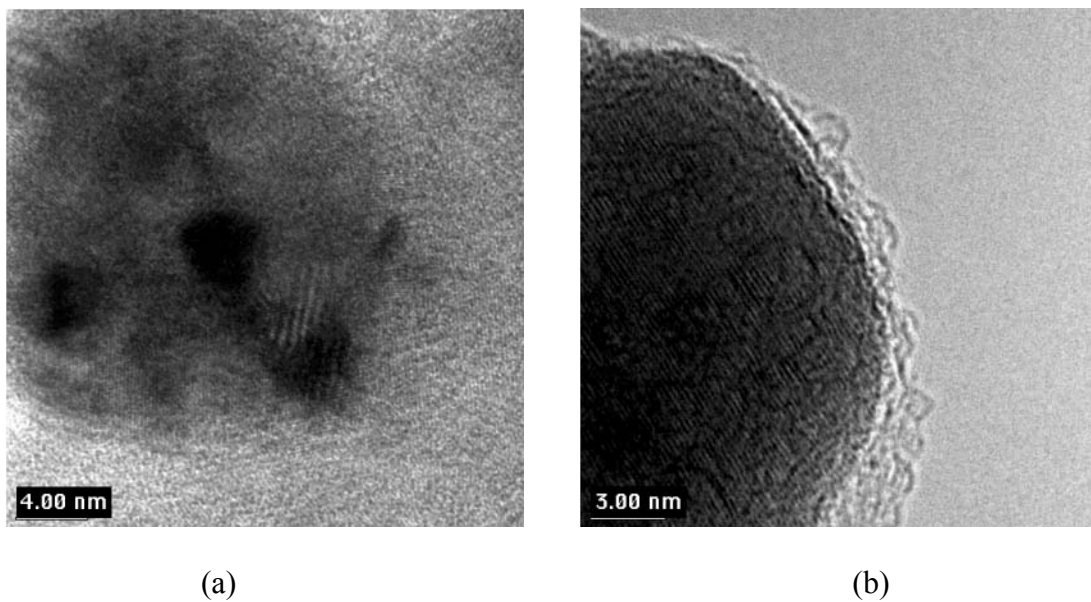


Figure 3.3. High-resolution TEM images of Pt nanoparticles. Particle diameter is 27 nm.
a) Before any treatment (as-prepared sample). b) After heating in vacuum at 500°C for 3 hours. The crystallinity improved after heating.

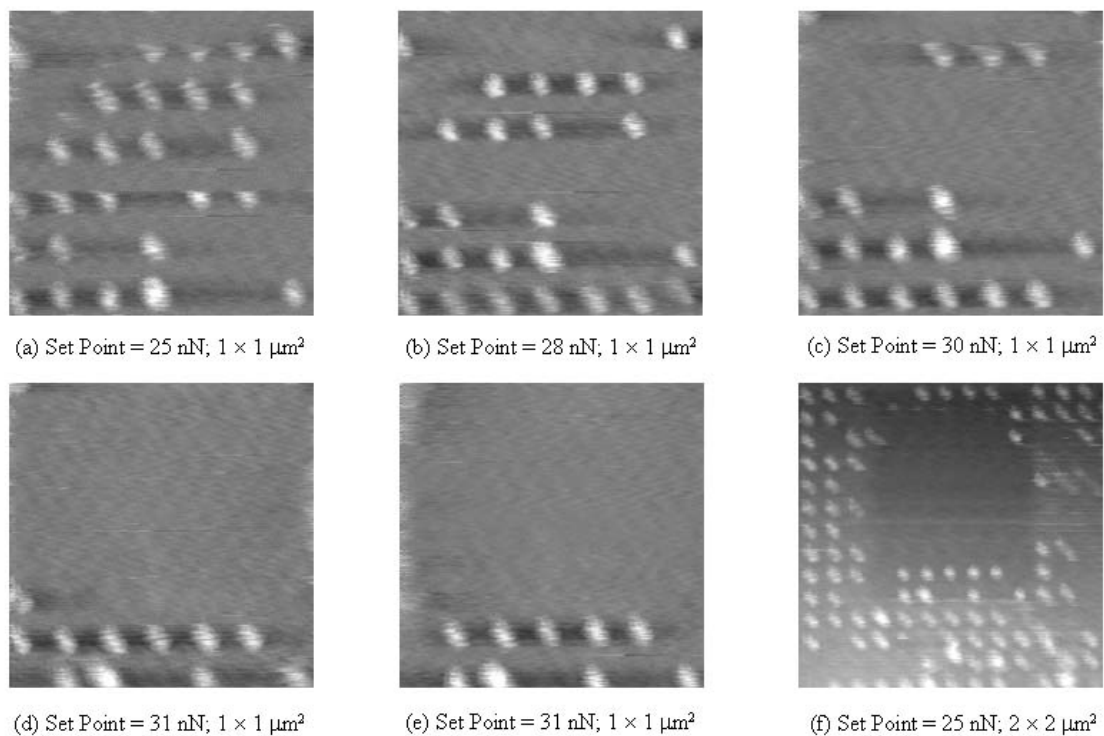


Figure 3.4. AFM images showing the nanoparticles being displaced by the tip. The nanoparticles were displaced at consecutively higher forces in Figures 3.4a-3.4e. In Figure 3.4f, the scanned area was enlarged to show the affected area. The scanning speed was $2.4 \mu\text{m/s}$ (1.2 Hz) for Figures 3.4a-3.4e and $4.8 \mu\text{m/s}$ (1.2 Hz) for Figure 3.4f.

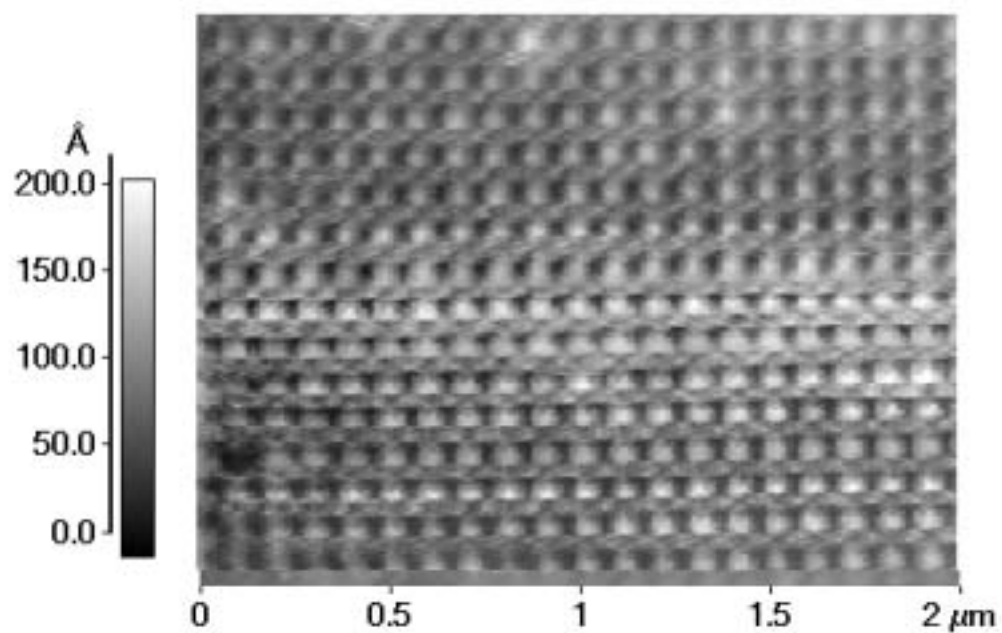


Figure 3.5. AFM images of Pt nanoparticle arrays after heat treatment taken with a non-contact cantilever. The set point was 4000 nN. The nanoparticles were not displaced and showed up as bright spots in the image. Scanning speed was 0.4 $\mu\text{m/s}$ (0.1 Hz).

References

-
- ¹ Anderson, J. R. *Structure of Metallic Catalysts*. Academic Press, London, 1975.
- ² Bond, G.C. *Surf. Sci.* **1985**, *156*, 966.
- ³ Taylor, W.F.; Yates, D.J.C.; Sinfelt, J.H. *J. Phys. Chem.* **1964**, *68*, 2962.
- ⁴ Pajonk, G.M. *Appl. Catal.* **2000**, *202*, 157.
- ⁵ Somorjai, G.A. *Introduction to Surface Chemistry and Catalysis*. Wiley, New York, 1994.
- ⁶ Kubo, R. *J. Phys. Soc. Japan* **1962**, *17*, 975.
- ⁷ Gates, B.C. *Top. Catal.* **2001**, *14*, 173.
- ⁸ Paszti, Z.; Peto, G.; Horvath, Z.E.; Karacs, A.; Gucci, L. *J. Phys. Chem. B* **1997**, *101*, 2109.
- ⁹ Van Hardeveld, R.M.; Gunter, P.L.J.; Van Uzendoorn, L.J.; Wieldraaijer, W.; Kuipers, E.W.; Niemantsverdriet, J.W. *Appl. Surf. Sci.* **1995**, *84*, 339.
- ¹⁰ Lai, X.; St. Clair, T.P.; Valden, M.; Goodman, D.W. *Prog. Surf. Sci.* **1998**, *59*, 25.
- ¹¹ Heiz, U.; Sanchez, A.; Abbet, S.; Schneider, W.-D. *J. Am. Chem. Soc.* **1999**, *121*, 3214.
- ¹² Roy, H.V.; Fayet, P.; Patthey, F.; Schneider, W.-D.; Delly, B.; Massobrio, C. *Phys. Rev. B* **1994**, *49*, 5611.
- ¹³ Schildenberger, M.; Bonetti, Y.; Aeschlimann, M.; Scandella, L.; Gobrecht, J.; Prins, R. *Catal. Lett.* **1998**, *56*, 1.
- ¹⁴ Krauth, A.C.; Lee, K.H.; Bernstein, G.H.; Wolf, E.E. *Catal. Lett.* **1994**, *27*, 43.
- ¹⁵ Johansson, S.; Osterlund, L.; Kasemo, B. *J. Catal.* **2001**, *201*, 275.
- ¹⁶ Johansson, S.; Fridell, E.; Kasemo, B. *J. Vac. Sci. Technol. A* **2000**, *18*, 1514.
- ¹⁷ Eppler, A.S.; Zhu, J.; Anderson, E.H.; Somorjai, G.A. *Top. Catal.* **2000**, *13*, 33.

-
- ¹⁸ Jacobs, P.W.; Wind, S.J.; Ribeiro, F.H.; Somorjai, G.A. *Surf. Sci.* **1997**, *372*, L249.
- ¹⁹ Chou, S.Y.; Krauss, P.R.; Renstrom, P.J. *Appl. Phys. Lett.* **1995**, *67*, 3114.
- ²⁰ Chou, S.Y.; Krauss, P.R.; Renstrom, P.J. *Science* **1996**, *272*, 85.
- ²¹ Vieu, C.; Carcenac, F.; Pepin, A.; Chen, Y.; Mejias, M.; Lebib, A.; Manin-Ferlazzo, L.; Couraud, L.; Launois, H. *Appl. Surf. Sci.* **2000**, *164*, 111.
- ²² Eppler, A.S.; Rupprechter, G.; Anderson, E.H.; Somorjai, G.A. *J. Phys. Chem. B* **2000**, *104*, 7286.
- ²³ Ogletree, D.F.; Carprick, R.W.; Salmeron, M. *Rev. Sci. Instrum.* **1996**, *67*, 3298.
- ²⁴ Merlin, V.; Eustathopoulos, N. *J. Mater. Sci.* **1995**, *30*, 3619.
- ²⁵ Chefi, C.; Mbarki, M.; Hila, F.; Gillet, M. *Surf. Sci.* **1996**, *352-354*, 883.
- ²⁶ Hojrup Hansen, K.; Worren, T.; Stempel, S.; Lasgaard, E.; Baumer, M.; Freund, H.-J.; Besenbacher, F.; Stensgaard, I. *Phys. Rev. Lett.* **1999**, *83*, 4120.
- ²⁷ Sounilhac, S.; Barthel, E.; Creuzet, F. *J. Appl. Phys.* **1999**, *85*, 222.
- ²⁸ Israelachvili, J. *Intermolecular & Surface Forces*. Academic Press, London, 1997.

Chapter 4

Ethylene Hydrogenation over Platinum Nanoparticle Array Model Catalysts Fabricated by Electron Beam Lithography: Determination of Active Metal Surface Area

4.1 Introduction

One important direction of heterogeneous catalysis research is to develop systems with high reaction selectivity, with 100% selectivity being the ultimate objective. In order to accomplish this, it is necessary to control the atomic-level catalyst ingredients that control selectivity as mentioned in Chapter 1. Knowing these criteria, a catalyst system that contains these properties can be synthesized.^{1, 2, 3, 4, 5} Chapter 3 showed that nanoparticle arrays can be fabricated by electron beam lithography and that these

nanoparticles have a high thermal stability, making them suitable for catalytic reaction studies. Catalytic reactions can be divided into two categories: structure-sensitive and structure-insensitive.⁶ A structure-sensitive reaction will show a dependence on the specific crystallographic face of a metal or the metal particle size⁷, while a structure-insensitive reaction does not have such a dependence. The metal particle size can affect the electronic structure of a metal particle for sizes less than 50 Å. Structure sensitivity has been seen in the partial oxidation of ethylene on Ag as well as the dehydrogenation, hydrogenolysis, and dehydrocyclization of hydrocarbons on Pt.^{8, 9, 10} Most hydrogenation reactions on transition metal catalysts, however, are structure insensitive.

To investigate the catalytic properties of the nanoparticles and establish the viability of this array as a model catalyst system, ethylene hydrogenation was used as a test reaction. This structure-insensitive reaction¹¹ has been extensively studied. This reaction is highly exothermic and readily catalyzes at room temperature ($\Delta G^\circ = -24.1$ kcal/mol at $T = 300$ K). The fact that the reaction has a high turnover makes it an ideal reaction to probe with the nanoparticle array, given the surface area of these samples (mm^2).

In this chapter, results from the characterization and ethylene hydrogenation reaction on alumina-supported Pt nanoparticle samples fabricated by electron beam lithography are presented. The nanoparticles were characterized with AFM, SEM, XPS, and AES. A novel cleaning method for catalyst activation was established for the Pt nanoparticles. The kinetic data for the ethylene hydrogenation reaction on the Pt nanoparticle arrays was compared with data obtained from the reaction on a Pt(111) single crystal.¹² The determination of surface area is also reported in this chapter.

Surface area determinations for supported catalysts usually involve the chemisorption of gases. For high surface area catalysts, gases such as CO and H₂ chemisorption are monitored for their uptake on the metal surface.¹³ For low surface area systems, such as single crystal model catalysts, temperature programmed desorption (TPD) is utilized. In this chapter, the structure-insensitive ethylene hydrogenation reaction itself is used to determine *in situ* the active metal surface area of the nanoparticle array model catalyst.

4.2 Experimental

4.2.1 Fabrication and Characterization

The electron beam lithography fabrication process as well as the characterization techniques of AFM, SEM, XPS, and AES have been described in Chapter 2.

4.2.2 NO₂ Cleaning

For single crystal activation, ion sputtering has proven to be an effective cleaning method. Ion sputtering was determined to be a destructive cleaning method for the Pt nanoparticle array model catalysts, as the Pt array pattern was transferred into the Al₂O₃ layer during Ne⁺ sputtering.^{14, 15} For high surface area catalysts, exposure to reducing and oxidizing environments, coupled with heat, is successful for cleaning and thus activating the catalyst. No matter the combination of pressures and temperatures, cycles of oxygen and hydrogen at elevated temperatures also proved to be ineffective for cleaning the nanoparticle array model catalysts. The sample was cleaned of surface carbon by dosing it at 1×10^{-6} Torr of NO₂ at 300°C for 20 minutes. This process,

however, left chemisorbed oxygen on the Pt surface. The oxygen was removed by dosing 10 L of CO (1×10^{-7} Torr of CO for 100 s). Any CO or CO₂ that was left on the surface after this step was removed by flashing the sample to 300°C. This method was repeated for a sample introduced to the UHV chamber for the first time. Analysis by Auger spectroscopy showed that this procedure removed 99+% of the typical carbon and oxygen contaminants from the Pt foil surface (Figure 4.1). This procedure also proved effective for cleaning the nanoparticle array model catalyst, as shown in the kinetic study of ethylene hydrogenation. Some oxygen is always present due to the oxide layer on the wafer.

4.2.3 UHV Chamber with High-Pressure Reaction Cell

The general design of the UHV chamber with the high-pressure reaction cell has been described in Chapter 2. The catalyst was cleaned by procedures described above before being used in the ethylene hydrogenation reaction. The sample was allowed to cool to the reaction temperature before being exposed to the reactant gas. The reactant gas mixture of 10 Torr C₂H₄, 100 Torr H₂, and 800 Torr Ne make-up gas was pre-mixed in a gas manifold. The volume of the batch reactor was 209 mL. The flow rate was 100 mL/min, and the gas in the reaction cell was refreshed every 14 min. It was necessary to bring the reactant gas mixture to ambient pressure because the recirculation pump (Metal Bellows, MB-21) did not operate at pressures less than 400 Torr. Using pressures above 1 atm ensured the purity of the reactant gas mixture throughout the experiment. During the reaction, the reactant and product mixture was sampled every 2.5 min using an automatic 6-way sampling valve. This valve was on the reaction loop and attached to a

gas chromatograph (Hewlett-Packard 5890 series II). The hydrocarbons were separated with a 30-m alumina capillary column (J&W Scientific) and monitored by a flame ionization detector.

4.3 Results and discussion

4.3.1. Characterization of the Pt Nanoparticle Arrays

XPS, AFM, and SEM were used to characterize the model catalyst after fabrication. The XPS measurements established that the nanoparticles were in fact Pt and were resting on a layer of alumina (Figure 4.2). The AFM and SEM measurements were used to determine the particle height, periodicity, and diameter of the particles. The AFM data established the height and spacing of the nanoparticles. The true diameter of the nanoparticles cannot be determined with the AFM due to the curvature of the AFM tip being convoluted in the image. The height of the nanoparticle sample studied was (15 ± 2) nm with an interparticle spacing of (100 ± 1) nm (Figure 4.3). The SEM image shows that the Pt particles have a diameter of (28 ± 2) nm and that the periodicity is (100 ± 1) nm (Figure 4.4). AES was used to monitor the cleanliness of the catalyst before proceeding with the reaction. Typical contaminants include carbon (278 eV) and oxygen (510 eV) for a dirty sample. The spectra also show Pt peaks, thus confirming that the nanoparticles are Pt. The AES data confirmed that the cleaning cycle was effective in removing surface contaminants from the nanoparticle arrays. AFM and SEM measurements of the nanoparticle arrays after repeated cleaning cycles showed no change to the sample.

4.3.2 Ethylene Hydrogenation Reaction Rate Studies

The reactivity of the Pt nanoparticle catalyst, with 28-nm diameter particles, 15-nm height, and 100-nm spacing, was studied with the structure-insensitive ethylene hydrogenation reaction. Because the reaction is structure-insensitive, the nanoparticle data could be compared to Pt(111) single crystal data.

A blank reaction was run with a Si(100) wafer, coated with a 15-nm alumina film, in order to determine if any background reaction would be observed. There was no significant reaction seen; thus, the gold-plating of the rotatable manipulator on which the sample rests was successful in eliminating any background reaction.

The cleaning method is necessary for activation of the nanoparticle array model catalyst. If the sample is cleaned by the conventional methods of ion sputtering or hydrogen/oxygen cycles, the catalyst is not active for the reaction and no product is seen. Only after the cleaning procedure described is used does the nanoparticle array become active for catalytic reactions.

A product accumulation curve (ethane) was first determined in order to establish a conversion rate for the reaction (Figure 4.5). The reaction conditions were 10 Torr C₂H₄, 100 Torr H₂, 800 Torr Ne, and a temperature of 60°C. The conversion rate for ethylene to ethane was ~6% per run, with each run lasting 150 s. Kinetic data was collected to determine the activation energy for the ethylene hydrogenation reaction on the Pt nanoparticle array model catalyst system. Using a 10:1 hydrogen to hydrocarbon ratio (100 Torr H₂ and 10 Torr C₂H₄, along with 800 Torr Ne make-up gas), the reaction was run at temperatures from 40°C to 150°C. From an Arrhenius plot, the activation energy

was determined to be (10.2 ± 0.2) kcal/mol (Figure 4.6). The pressure order of each of the reactant gases was then investigated. By holding the ethylene pressure constant at 10 Torr, fixing the reaction temperature at 100°C, and varying the hydrogen pressure from 25 to 200 Torr (along with Ne make-up gas), the pressure order of H₂ was calculated to be (1.2 ± 0.4) (Figure 4.7). When the hydrogen pressure was fixed at 100 Torr, with the temperature set at 100°C and varying the ethylene pressure from 10 to 40 Torr (and Ne make-up gas), the C₂H₄ pressure order was determined to be (-0.88 ± 0.05) (Figure 4.8). From the comparison chart of model catalyst kinetic parameters, it can be seen that the Pt nanoparticle array data is in excellent agreement with the Pt(111) single crystal data (Table 4.1).

4.3.3 Active Metal Surface Area Determination

The NO₂ cleaning method is important for more than just activating the nanoparticle array model catalyst. The cleaning procedure allows for the entire metal surface area of the nanoparticle array model catalyst to be active for the reaction. Without cleaning the sample, the array would be dirty and fewer sites would be available for catalysis.

Because the ethylene hydrogenation reaction is structure insensitive, a rate equation established for a Pt(111) single crystal can be utilized¹²:

$$Rate = (8 \pm 4) \times 10^8 \times \exp[-(10.8 \pm 0.1) / RT] P_{ethylene}^{(-0.60 \pm 0.05)} P_{hydrogen}^{(1.31 \pm 0.05)}$$

where R is the gas constant ($= 1.987 \times 10^{-3}$ kcal/K/mol), T is temperature in K, P is pressure in atm, and rate (turnover frequency, TOF) has units of molecules/Pt atom/s. Using the reaction conditions of 10 Torr C₂H₄, 100 Torr H₂, and running the experiment

at 100°C, a TOF is determined to be (354 ± 177) molecules/Pt atom/s. Combined with an initial conversion rate of 43 nmol/s from the accumulation curve, an active metal surface area was calculated to be (4.9 ± 2.5) mm².

Looking at the nanoparticle arrays from a purely geometrical perspective, it was assumed that the nanoparticles were cylinders that were 15 nm high, 28 nm in diameter, and 100 nm in pitch (interparticle spacing). The particles cover a 6 mm \times 6mm area; therefore, there are 3.60×10^9 particles. This gives a geometrical active metal surface area of 7.0 mm². The calculated active metal surface area compares well with the geometrical active metal surface area within experimental error. From the kinetic data obtained from Pt nanoparticle array model catalysts with 100-nm interparticle distance vs. 150-nm interparticle distance, there was a proportionality between the initial conversion rate and the active metal surface area. For the 100-nm spaced sample of 7.0 mm² active metal surface area, an initial conversion rate of 43 nmol/s was observed. For the 150-nm spaced sample with an active metal surface area of 3.1 mm², an initial conversion rate of 23 nmol/s was observed.

The ethylene hydrogenation reaction can therefore be used as a means to determine the active metal surface area of the nanoparticle array model catalyst. The method can be utilized to simply determine the surface area of a clean catalyst and determine the active metal surface area of a dirty catalyst (titrate the surface for remaining active sites).

4.4 Conclusion

Platinum nanoparticle array model catalysts were successfully fabricated using electron beam lithography and characterized with surface science techniques to ensure composition and dimensions of the samples, such as AFM, SEM, and XPS. The lithography technique allowed for the creation of Pt nanoparticles that were 15 ± 2 nm in height, 28 ± 2 nm in diameter, and with an interparticle spacing of 100 ± 1 nm. The model catalyst was used to study the kinetic parameters of the ethylene hydrogenation reaction. The activation energy and the pressure orders of the H_2 and the C_2H_4 for ethylene hydrogenation over the Pt nanoparticle array compared very well with data from running the reaction on a Pt(111) single crystal. This proved that the nanoparticle arrays are a viable model catalyst system for study.

A novel method for cleaning and thus activating the nanoparticle arrays was determined. The method was both effective in cleaning the model catalysts as well as safe to the sample, as determined by AES. The structure-insensitive reaction of ethylene hydrogenation over the nanoparticle catalysts proved to be a viable means to calculate the active metal surface area. This enables a method to determine the active metal surface area of the nanoparticle arrays under reaction conditions and within the sample experimental set-up. It can also provide information as to the remaining active metal surface area for a sample that may be dirty, partially titrated by a reaction, or for poisoning studies. The next chapter will examine the effects of CO-poisoning of ethylene hydrogenation over the Pt nanoparticle array model catalyst.

Table 4.1. Comparison chart of kinetic parameters for ethylene hydrogenation reaction over Pt(111) single crystal and Pt nanoparticle array model catalysts.

Sample	Activation Energy (kcal/mol)	Pressure order of H ₂	Pressure order of C ₂ H ₄
Pt(111) single crystal	10.8	1.31	-0.6
Pt nanoparticle array	10.2 ± 0.2	1.2 ± 0.4	-0.88 ± 0.05

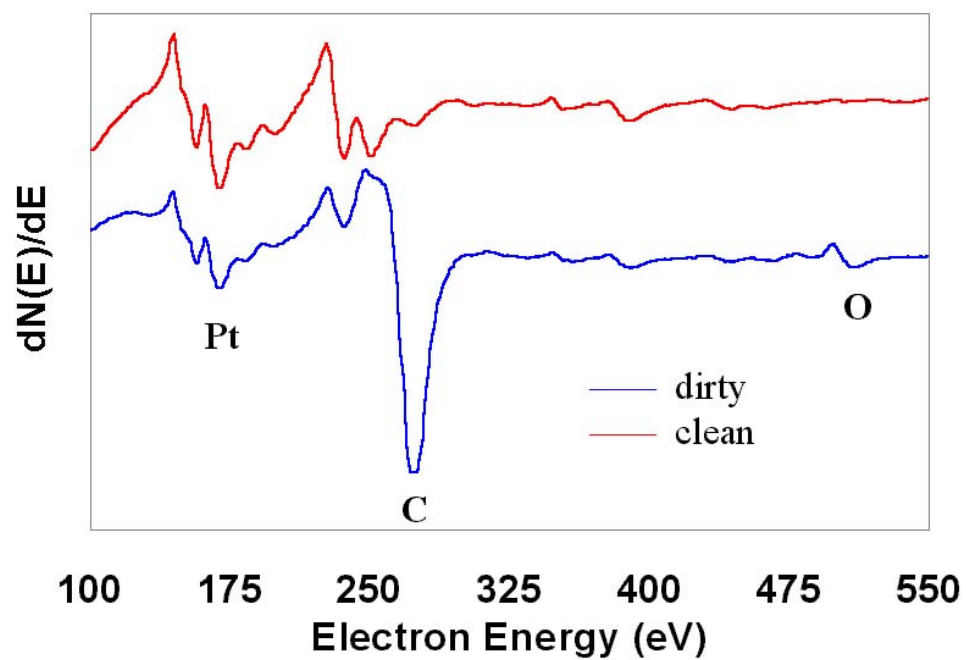


Figure 4.1. AES spectra of clean and dirty Pt foil surface. The NO₂ cleaning procedure removed 99+% of the typical C and O contaminants on the surface. The Pt nanoparticles showed similar results, thus proving the cleaning procedure effective, safe, and reproducible.

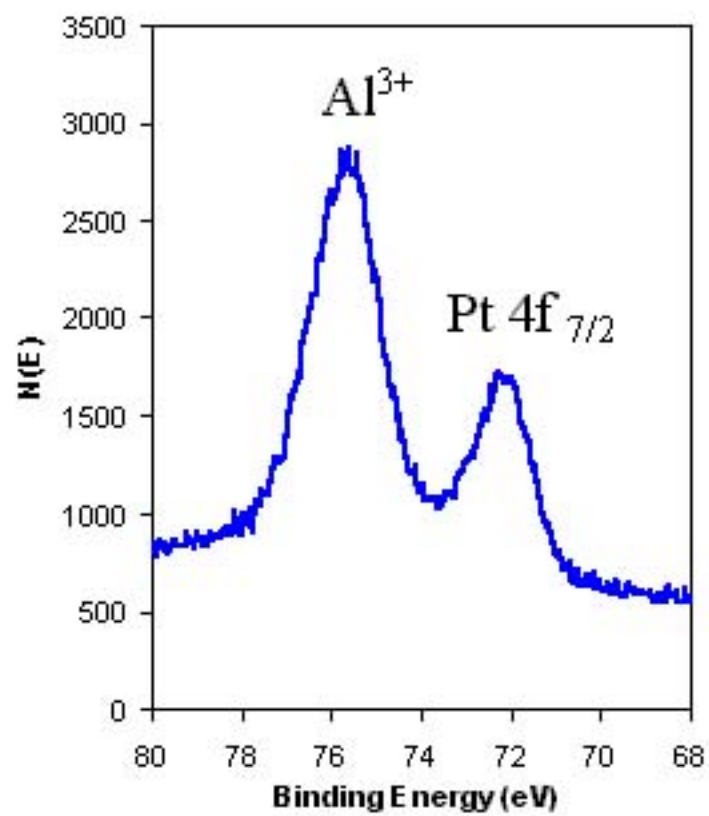


Figure 4.1. XPS of Pt nanoparticle array model catalyst showing Pt particles and alumina insulation layer.

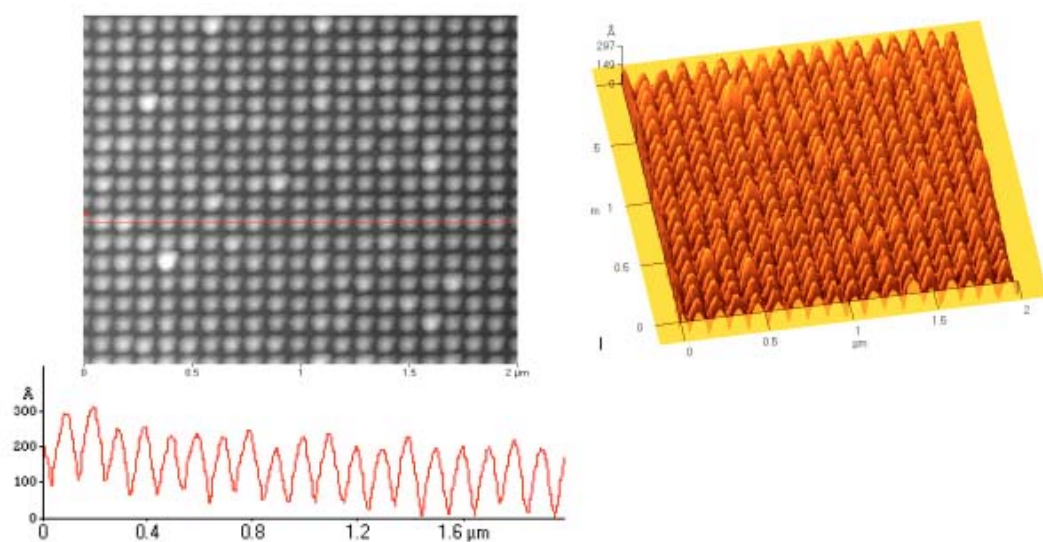
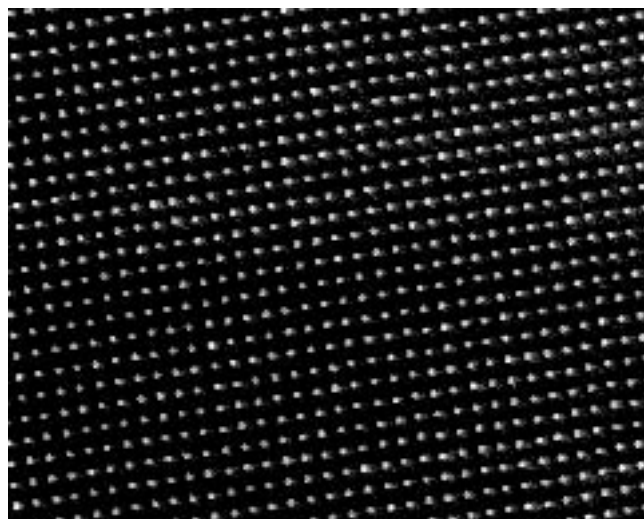


Figure 4.2. AFM line profile and topography showing that the nanoparticle height is (15 ± 2) nm with an interparticle spacing of (100 ± 1) nm. The size of the nanoparticles appears larger in the topography image than they really are due to the curvature of the AFM tip being convoluted in the image.



— 200 nm

Figure 4.3. SEM image of the nanoparticle array showing a diameter of (28 ± 2) nm and a periodicity of (100 ± 1) nm.

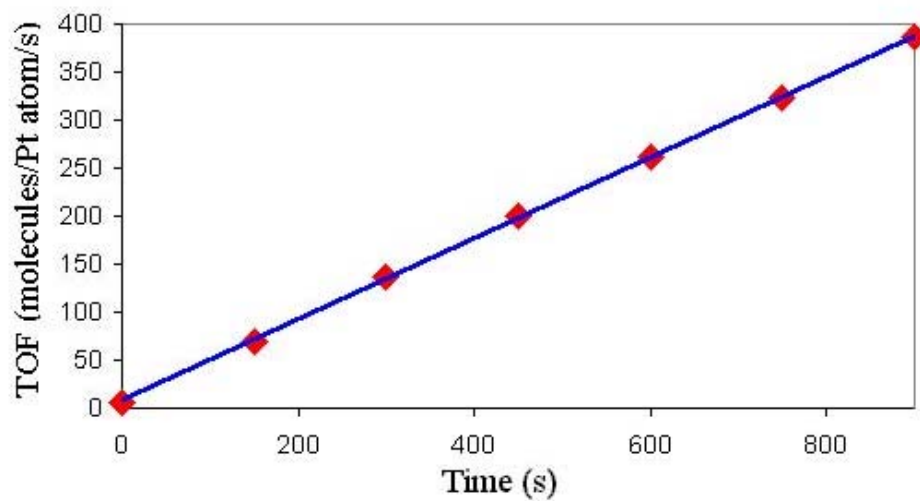


Figure 4.4. Product accumulation curve for conversion of ethylene to ethane. The reaction conditions are 10 Torr C_2H_4 , 100 Torr H_2 , 800 Torr Ne, and a temperature of 60 $^\circ\text{C}$.

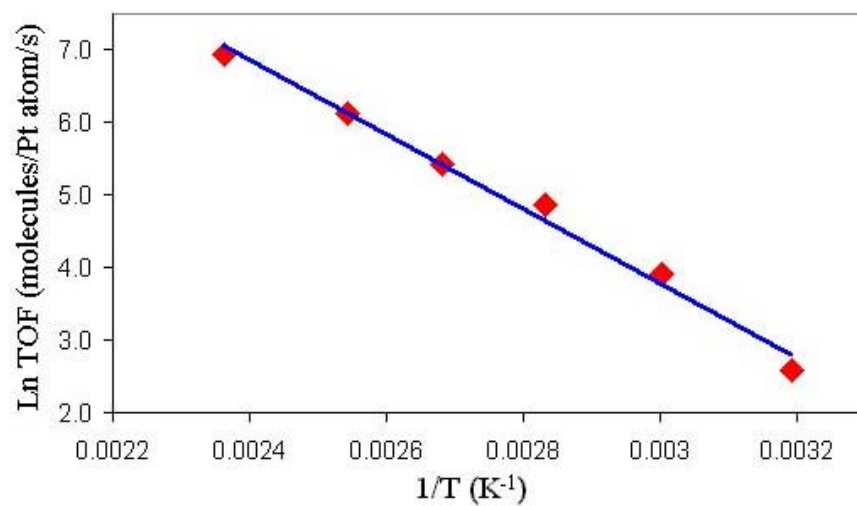


Figure 4.5. Arrhenius plot to determine the activation energy of ethylene hydrogenation over the Pt nanoparticle array. Reaction conditions were 10 Torr C₂H₄, 100 Torr H₂, and 800 Torr Ne.

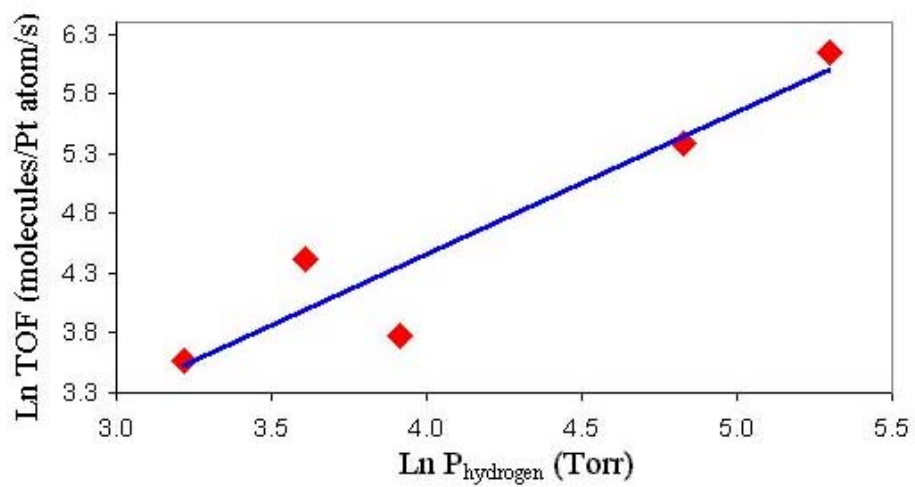


Figure 4.6. Pressure order for H₂ in ethylene hydrogenation reaction over Pt nanoparticle array model catalyst. Reaction conditions were 10 Torr C₂H₄ and 100°C.

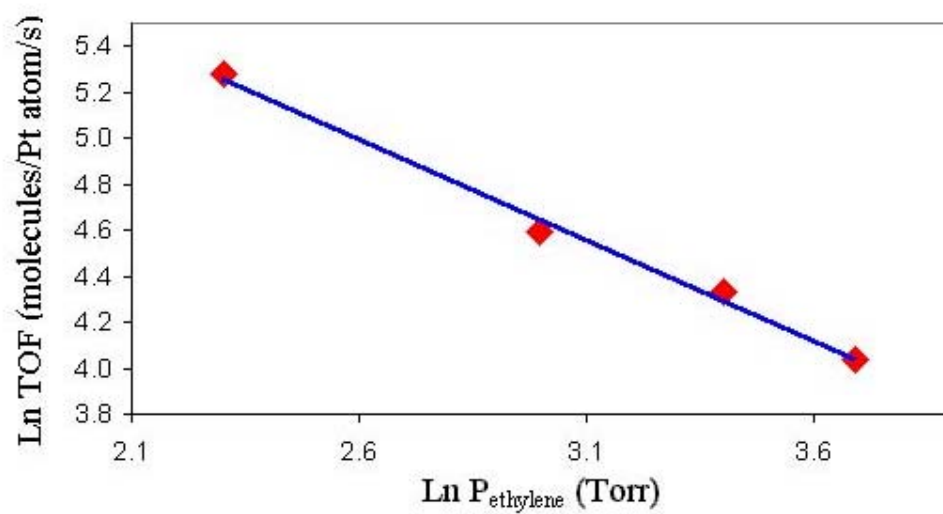


Figure 4.7. Pressure order for C_2H_4 in ethylene hydrogenation reaction over Pt nanoparticle array model catalyst. Reaction conditions were 100 Torr H_2 and $100^\circ C$.

References

-
- ¹ Poppa, H. *Vacuum* **1984**, *34*, 1081.
- ² Wong, K.; Johansson, S.; Kasemo, B. *Faraday Discuss.* **1996**, *105*, 237.
- ³ Jacobs, P.W.; Ribeiro, F.H.; Somorjai, G.A.; Wind, S.J. *Catal. Lett.* **1996**, *37*, 131.
- ⁴ Che, M.; Bennett, C.O. *Adv. Catal.* **1989**, *36*, 55.
- ⁵ Henry, C.R. *Surf. Sci. Rep.* **1998**, *31*, 231.
- ⁶ Boudart, M.; Djega-Mariadassou, G. *Kinetics of Heterogeneous Catalytic Reactions*. Princeton University Press, Princeton, New Jersey, 1984.
- ⁷ Boudart, M. *Adv. Catal.* **1969**, *20*, 153.
- ⁸ Somorjai, G.A. *Introduction to Surface Chemistry and Catalysis*. John Wiley & Sons, New York, 1994.
- ⁹ Joyner, R.W.; Lang, B.; Somorjai, G.A. *Proc. Roy. Soc. (London)* **1972**, *331*, 335.
- ¹⁰ Herz, R.K.; Gillespie, W.D.; Peterson, E.E.; Somorjai, G.A. *J. Catal.* **1981**, *67*, 371.
- ¹¹ Horiuti, J.; Miyahara, K. *Hydrogenation of Ethylene on Metallic Catalysts*, National Standard Reference Data System-National Bureau of Standards (NSRDS-NBS), **1968**, 13.
- ¹² Zaera, F.; Somorjai, G.A. *J. Am. Chem. Soc.* **1984**, *106*, 2288.
- ¹³ Anderson, J.R. *Structure of Metallic Catalysts*. Academic Press: London, 1975.
- ¹⁴ Eppler, A.S.; Zhu, J. Anderson, E.H.; Somorjai, G.A. *Top. Catal.* **2000**, *13*, 33.
- ¹⁵ Zhu, J.; Somorjai, G.A. *Nano Lett.* **2001**, *1*, 8.

Chapter 5

CO Poisoning of Ethylene Hydrogenation over Pt Catalysts: A Comparison of Pt(111) Single Crystal and Pt Nanoparticle Activities

5.1 Introduction

While previous chapters have demonstrated the value of electron beam lithography for fabricating catalysts that resemble the industrial catalyst, are robust and thermodynamically stable, are suitable for catalysis, and are a viable model catalyst system, there is still another measure for the usefulness of a catalyst. A catalyst must remain active for a number of years in order to be considered successful. Deactivation is therefore a prime concern when developing industrial catalysts. During a reaction, reactants, intermediates, products, or unwanted species can cover the catalyst surface.

The species can block the active sites of the catalyst, thus changing the properties of the catalyst over time.¹ Infrared absorption spectra of adsorbed carbon monoxide on several transition metals exhibit different spectral features when the CO adsorbs at different sites on the metal surface.^{2, 3, 4, 5, 6, 7} Carbon monoxide is therefore often used as a probe molecule to determine the availability of adsorption sites during a catalytic reaction.⁸ It is well known that CO adsorption can poison hydrocarbon reactions. In this chapter, the ethylene hydrogenation reaction over Pt model catalysts in the presence and absence of CO is investigated and a mechanism that governs the CO-poisoned reaction is proposed.

5.2 Experimental

5.2.1 Pt(111) Single Crystal Model Catalysts: Characterization and Reaction Rate Studies

The experimental apparatus consists of an ultra-high vacuum (UHV) chamber coupled with a high-pressure (HP) reaction cell. The catalyst was cleaned and characterized in the UHV chamber, and the HP reaction cell was used to monitor the catalytic reaction via gas chromatography (GC). A detailed description of the experimental set-up can be found elsewhere.⁹

The Pt(111) single crystal was cleaned in UHV by cycles of Ar⁺ sputtering, O₂ treatment, and annealing.¹⁰ After the single crystal was cleaned, the HP reaction cell was closed and the gas mixture was introduced. The reaction gas mixture for the Pt(111) single crystal included 10 Torr C₂H₄, 1 Torr CO, 100 Torr H₂, and Ar make-up gas to

bring the total gas pressure to 760 Torr. The reaction was then monitored over time for product accumulation with a GC.

5.2.2 Pt Nanoparticles on Alumina: Fabrication, Characterization, and Reaction Rate Studies

The details of the electron beam lithography fabrication process for the Pt nanoparticle array model catalyst has been detailed in previous chapters. Briefly, a highly-collimated electron beam is used to expose a thin layer of polymethylmethacrylate (PMMA), which is spin-coated on a Si(100) wafer that is coated with 15 nm of alumina (Al_2O_3). The electron irradiation decomposes the polymer backbone, making it possible to dissolve the exposed polymer in a developing solution. A 15-nm thick Pt film was deposited on the surface by electron beam evaporation. The remaining PMMA was removed with acetone and ultrasonication. The alumina-supported Pt nanoparticle array model catalyst has a (100 ± 2) nm interparticle spacing with particle diameters of (28 ± 2) nm. The sample was characterized by field emission scanning electron microscopy (FESEM), atomic force microscopy (AFM), and X-ray photoelectron spectroscopy (XPS).

The Pt nanoparticle system was cleaned with NO_2 , followed by dosing the sample with CO and flashing the temperature to 573 K. This removes the major impurities on the surface, such as oxygen and carbon. This procedure has been established to be safe and effective for cleaning the Pt nanoparticles.¹¹ The catalysis study was performed in a similar UHV chamber with an HP reaction cell. The details of this experimental set-up have been described in Chapter 2. The reaction gases were pre-mixed in a gas manifold

before being introduced into the HP reaction cell. The reaction gas mixture consisted of 10 Torr C₂H₄, 0.3 Torr CO, 100 Torr H₂, and Ne make-up gas to bring the total gas pressure to 760 Torr. The products were analyzed with a GC.

5.3 Results and Discussion

5.3.1 CO-Poisoned Ethylene Hydrogenation Reaction Rate Studies on Pt(111): Effects of Temperature

The poisoning effects of CO for the ethylene hydrogenation reaction over Pt(111) were investigated from 400 to 523 K. Arrhenius plots of the initial turnover frequency (TOF) as a function of 1/T for ethylene hydrogenation with (▲) and without (◆) CO over Pt(111) are shown in Figure 5.1. Turnover frequency (TOF) is defined as the number of ethane molecules generated per Pt surface atom per second. When CO is adsorbed, the TOF is reduced by 2-3 orders of magnitude, depending on the temperature. At 413 K, the reaction rate for ethylene hydrogenation over the Pt(111) single crystal in the presence of CO is reduced from 10¹ to 10⁻² molecules/Pt atom/s; at 473 K, the reaction rate for ethylene hydrogenation over the Pt(111) single crystal in the presence of CO is reduced from 10² to 10⁰ molecules/Pt atom/s. Activation energies obtained from the slopes in Figure 5.1 for ethylene hydrogenation over the Pt(111) single crystal in the presence and absence of CO are (20.2 ± 0.1) and (9.6 ± 0.4) kcal/mol, respectively. The measured activation energy for ethylene hydrogenation over Pt(111) in the absence of CO is consistent with previous studies, which reported an activation energy of 10.8 kcal/mol.¹²

The measured activation energy for ethylene hydrogenation on Pt(111) in the presence of 1 Torr CO, (20.2 ± 0.1) kcal/mol, is close in value to the desorption energy of CO on Pt(111). Carbon monoxide is known to form an incommensurate hexagonal overlayer on the surface, with a coverage of 0.60 ML, when the species is present in the mTorr range and above.¹³ At this coverage, the heat of adsorption of CO is (22 ± 4) kcal/mol.¹⁴ The proximity of this value with the ethylene hydrogenation activation energy suggests a possible correlation. Before the ethylene hydrogenation reaction can turnover on the single crystal, the CO that preferentially bound to the surface must be completely removed from the catalyst surface. The fact that the measured activation energy is within the range of CO desorption supports this step-wise process.

5.3.2 CO-Poisoned Ethylene Hydrogenation Reaction Rate Studies on Pt Nanoparticles Supported on Alumina: Effects of Temperature

The ethylene hydrogenation reaction over the Pt nanoparticles, with and without CO, was studied over the temperature range of 313 to 523 K. The activity of the Pt nanoparticles with 0.3 Torr CO is less than 5% of the activity without CO at the same temperature, as defined by the turnover frequency of converting ethylene to ethane molecules. At 413 K, the reaction rate for ethylene hydrogenation over the Pt nanoparticle array model catalyst in the presence of CO is reduced from 10^2 to 10^1 molecules/Pt atom/s. The reaction without CO was investigated from 313 to 423 K. Reactions conducted above 423 K proceeded too quickly to permit an accurate measurement of the reaction rate. Conversely, because the catalytic activity of the Pt nanoparticles was greatly inhibited in the presence of CO, the poisoning reaction was

studied from 373 to 523 K in order to get results that were distinguishable from the background reaction in the experimental timeframe.

Arrhenius plots for the ethylene hydrogenation reaction with (\blacktriangle) and without (\blacklozenge) CO over the Pt nanoparticle array model catalyst are shown in Figure 5.2. The graph shows that the activation energy for ethylene hydrogenation without CO, (10.2 ± 0.2) kcal/mol, is virtually identical to the activation energy for the reaction with 0.3 Torr CO, (11.4 ± 0.6) kcal/mol. The same effects on the ethylene hydrogenation reaction over the Pt nanoparticle array model catalyst are seen for reactions poisoned with either 0.6 or 0.3 Torr CO. The reaction rate at 413 K is reduced by almost two orders of magnitude and the activation energy remains the same.

The activation energy difference between the Pt(111) single crystal and the Pt nanoparticle array model catalyst for a reaction poisoned by CO is significant. Because the activation energy is largely unchanged for the nanoparticle array in the presence of CO, concentrations of Pt sites must still be available for ethylene hydrogenation. It is known that CO hydrogenation is enhanced at oxide-metal interfaces.¹⁵ Therefore, these interface sites could remain free of CO in order to continue hydrogenating the ethylene. With increasing CO pressure, fewer CO free sites are available. On the single crystal, CO poisons all available Pt sites. In this case, CO molecules must desorb in order for hydrogenation to take place on the metal surface. This helps explain why the activation energy for ethylene hydrogenation on Pt(111) in the presence of CO is equal to that of the heat of desorption of carbon monoxide.

The main difference between the Pt(111) single crystal and the Pt nanoparticle array is the oxide-metal interface. Hydrogenation can take place at either of two sites.

First, there are metal sites that exist on both model catalyst systems and are prone to CO poisoning. Then there is the interface site, which appears to be less prone to CO poisoning due to electronic interactions. A difference in reactivity between these interface sites and metal sites may exist, as shown by the differences in the activation energy and turnover rate of the ethylene hydrogenation reaction with CO on both model catalyst systems. The difference could also be the result of the relative mobilities of species on the surface. Scanning tunneling microscopy (STM) results have shown that ordered structures appear for the ethylene hydrogenation reaction over Rh(111) single crystal catalysts when CO molecules are introduced into the system.¹⁶ The adsorption of CO on vacant hollow sites prevents the diffusion of ethylidyne. Because the surface becomes full of these immobile adsorbates, the ethylene from the gas phase has no room to adsorb, thus preventing hydrogenation. Mobility is necessary to free-up active hydrogenation sites. It is possible that the CO molecule retains its mobility at the oxide-metal interface sites on the Pt nanoparticle array model catalyst, which would keep these sites catalytically active for hydrogenation. The Pt nanoparticle array also has an alumina support, which can play a factor in diffusion and spillover effects of CO. Carbon monoxide could induce a reconstruction of the Pt nanoparticle surface, creating domain boundaries, which would then increase CO diffusion. The Pt nanoparticle arrays could also be exposing a different crystalline face at the interface that is not prone to CO poisoning, thus allowing the reaction chemistry to take place at another type of site. The strength of the adsorption of the CO molecule on the catalyst surface, ΔH_{ads} , is related to the mobility of the molecule on the catalyst surface, with weakly-bound species enjoying

greater mobility. The residence time of CO at these interfacial sites is small if the molecule is very mobile, and this would keep the sites available for reaction.

5.3.3 CO-Poisoned Ethylene Hydrogenation Reaction Rate Studies on Pt Nanoparticles Supported on Alumina: Effects of Pressure

The dependence of Pt nanoparticle model catalyst activity on CO pressure was also studied at 100 °C, the result of which is shown in Figure 5.3. The order of the pressure of CO was found to be (-0.9 ± 0.3) . The CO pressure dependence is inversely proportional, meaning that the reaction is slower for larger amounts of CO. From the pressure orders of hydrogen and ethylene as shown in Chapter 4, it qualitatively makes sense that CO can inhibit the turnover of ethylene to ethane. Since both species are roughly -1 order, they are competing for sites. The difference in sticking coefficients, saturation coverages, and bonding strengths all support the proposed mechanism purported for CO-poisoned ethylene hydrogenation. For a more in-depth physical understanding of the values of the pressure orders for all species, the literature can provide the necessary detail.^{17, 18, 19}

5.4 Conclusion

CO poisoning of the ethylene hydrogenation reaction has been studied on Pt(111) and Pt nanoparticle array model catalysts. Rate studies for Pt(111) show that the reaction is poisoned by CO, with the activation energy increasing from 10.8 to 20.2 kcal/mol. This poisoned activation energy is near the desorption energy of CO. Rate measurements for the CO-poisoned ethylene hydrogenation over the Pt nanoparticle arrays show a

decrease in activity, but not a meaningful increase in activation energy. The activation energies for the ethylene hydrogenation reaction over the Pt nanoparticles with and without CO are 11.4 and 10.2 kcal/mol, respectively. The oxide-metal interface sites might therefore remain active for ethylene hydrogenation, which in turn suggests these sites remain free of adsorbed CO. To get a molecular understanding of the role of CO in the reaction, sum frequency generation vibrational spectroscopy (SFG) was employed to study CO on the surface of the Pt(111) single crystal and the Pt nanoparticles, the results of which are detailed in the next chapter.

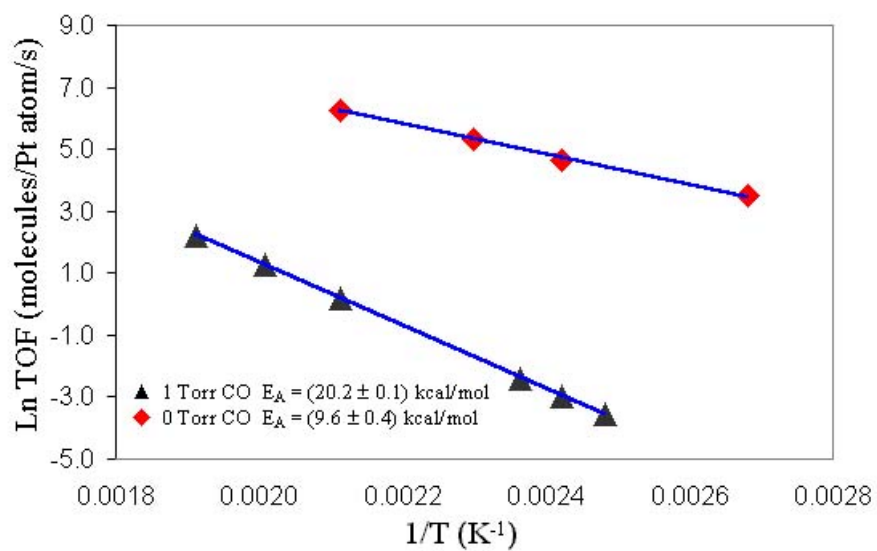


Figure 5.1. Logarithmic plots of turnover frequency (TOF) vs. $1/T$ for ethylene hydrogenation with (\blacktriangle) and without (\blacklozenge) CO over Pt(111). The activation energies obtained from the slopes are (20.2 ± 0.1) and (9.6 ± 0.4) kcal/mol with and without CO present, respectively. Reaction conditions were 10 Torr C_2H_4 and 100 Torr H_2 .

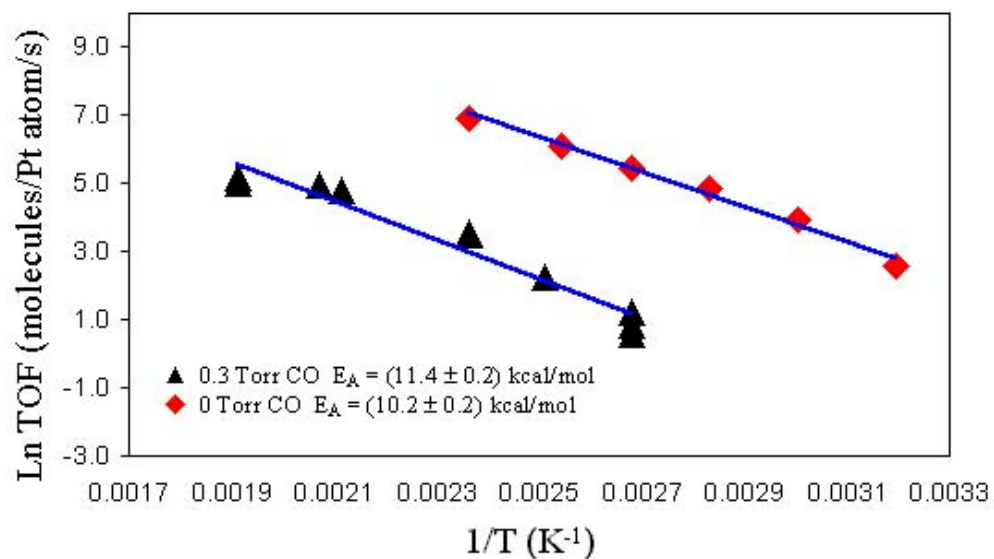


Figure 5.2. Arrhenius plots of the rate of ethylene hydrogenation vs. $1/T$ on platinum nanoparticle arrays with (▲) and without (◆) CO. The activation energies obtained from the slopes are (11.4 ± 0.6) and (10.2 ± 0.2) kcal/mol with and without CO present, respectively. Reaction conditions were 10 Torr C_2H_4 and 100 Torr H_2 .

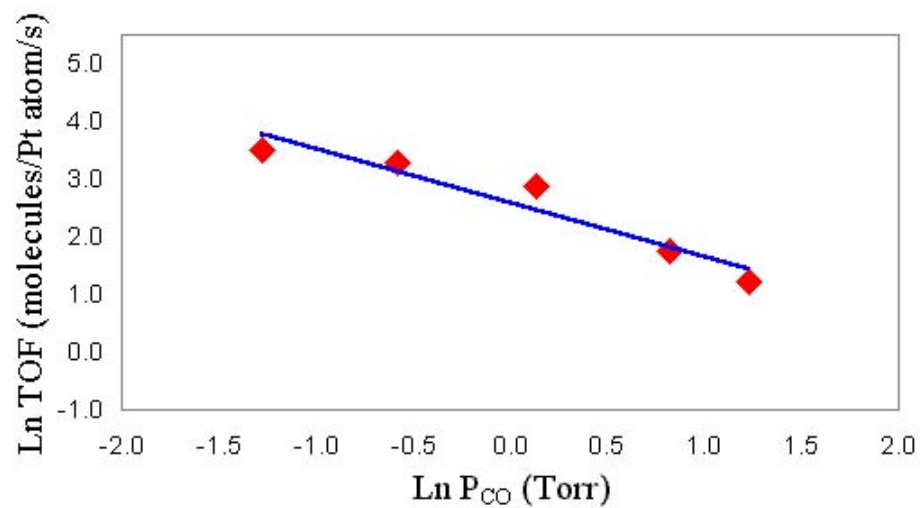


Figure 5.3. Pressure order for CO in poisoned ethylene hydrogenation reaction over Pt nanoparticle array model catalyst. Reaction conditions were 10 Torr C₂H₄, 100 Torr H₂, and 100°C.

References

-
- ¹ Ertl, G.; Knozinger, H.; Weitkamp, J., eds. *Handbook of Heterogeneous Catalysis*. Wiley-VCH, Weinheim, Germany, 1998.
- ² Hayden, B.E.; Bradshaw, A.M. *Surf. Sci.* **1983**, *125*, 787.
- ³ Trenary, M.; Uram, K.J.; Yates, J.T. *Surf. Sci.* **1985**, *157*, 512.
- ⁴ Kuhn, W.K.; Szanyi, J.; Goodman, D.W. *Surf. Sci.* **1992**, *274*, L611.
- ⁵ Hollins, P.; Pritchard, J. *Prog. Surf. Sci.* **1985**, *19*, 275.
- ⁶ Tushaus, M.; Schweizer, E.; Hollins, P.; Bradshaw, A.M. *J. Electron Spectrosc. Rel. Phenom.* **1987**, *44*, 305.
- ⁷ Crossley, A.; King, D.A. *Surf. Sci.* **1977**, *68*, 528.
- ⁸ Niemantsverdriet, J.W. *Spectroscopy in Catalysis: An Introduction*. Wiley-VCH, Weinheim, Germany, 2000.
- ⁹ Kung, K.Y.; Chen, P.; Wei, F.; Rupprechter, G.; Shen, Y.R.; Somorjai, G.A. *Rev. Sci. Instrum.* **2001**, *72*, 1806.
- ¹⁰ Chen, P.; Westerberg, S.; Kung, K.Y.; Zhu, J.; Grunes, J.; Somorjai, G.A. *Appl. Catal. A-Gen.* **2002**, *229*, 147.
- ¹¹ Grunes, J.; Zhu, J.; Anderson, E.H.; Somorjai, G.A. *J. Phys. Chem. B* **2002**, *106*, 11463.
- ¹² Zaera, F.; Somorjai, G.A. *J. Am. Chem. Soc.* **1984**, *106*, 2288.
- ¹³ Jensen, J.A.; Rider, K.B.; Salmeron, M.; Somorjai, G.A. *Phys. Rev. Lett.* **1998**, *80*, 1228.
- ¹⁴ Yeo, Y.Y.; Vattuone, L.; King, D.A. *J. Chem. Phys.* **1997**, *106*, 392.
- ¹⁵ Levin, M.E.; Salmeron, M.; Bell, A.T.; Somorjai, G.A. *J. Catal.*, **1987**, *106*, 401.

-
- ¹⁶ Hwang, K.S.; Yang, M.; Zhu, J.; Grunes, J.; Somorjai, G.A. *J. Mol. Catal. A* **2003**, *204-205*, 499.
- ¹⁷ Hansen, E.; Neurock, M. *J. Catal.* **2000**, *196*, 241.
- ¹⁸ Ofner, H.; Zaera, F. *J. Phys. Chem. B* **1997**, *101*, 396.
- ¹⁹ Rekoske, J.; Cortright, R.D.; Goddard, S.A.; Sharma, S.B.; Dumesic, J. *J. Phys. Chem.* **1992**, *96*, 1880.

Chapter 6

CO Poisoning of Catalytic Ethylene Hydrogenation on the Pt(111) Surface and CO Adsorption on Platinum Nanoparticle Arrays Studied by Sum Frequency Generation Vibration Spectroscopy (SFG)

6.1 Introduction

The deactivation of catalysts is always one of the major concerns in the development of efficient catalysts. As mentioned previously, during surface heterogeneous catalytic reactions, various reactants, intermediates, products or even unexpected foreign atoms and molecules may cover the catalyst surfaces.¹ These surface

substances could block the catalytic active sites or modify the electronic properties of the catalysts over time.² For example, if one or more of the reaction products are strongly adsorbed on the active sites, it could lead to self-poisoning. Undesired substances from the reaction mixture could adsorb on the catalyst surface, rendering the catalyst inactive. Not all the adsorbed species deactivate catalysts; some species promote the desired catalytic pathways by either reducing the activation energy or selectively blocking the undesired catalytic sites. To engineer better catalysts, it is crucial to understand what is the influence of the co-adsorbed species on the catalyst surface and their roles in catalytic reactions. In the past, most of the mechanistic studies of catalyst poisoning have been focused in using surface techniques, such as low-energy electron diffraction (LEED), Auger electron spectroscopy (AES), electron spectroscopy (UPS, XPS), temperature programmed desorption (TPD), high-resolution electron energy loss spectroscopy (HREELS), and infrared reflection spectroscopy (IRS).³ The infrared absorption spectra of adsorbed CO on several transition metals exhibit different spectral features, indicating the nature of the site and strength of the bond, when the CO adsorption sites are different.^{4, 5, 6, 7, 8, 9} Accordingly, CO has been widely used as a probe molecule to determine the availability of adsorption sites during catalytic reactions.¹⁰ But, the vibrational spectra of CO may be altered by the other co-adsorbed species on the surface, mentioned earlier, that can lead to complications in the interpretation of the spectra.¹¹ However, the typical surface techniques used to probe the mechanism of CO-poisoning are operated under vacuum condition and little is known about the behavior of adsorbates under high-pressure conditions. To fully understand the poisoning mechanism, it is desirable to monitor these species under reaction conditions.

As an *in situ* surface-specific vibrational spectroscopic tool, sum frequency generation vibrational spectroscopy (SFG) has been used to investigate CO adsorption on transition metals at high pressures and temperatures.^{12, 13, 14, 15} It has also been used to study the nature of surface intermediates during olefin hydrogenation reactions.^{16, 17, 18, 19} In most cases, it has been shown that the SFG technique is capable of monitoring surface vibrational spectra with submonolayer sensitivity. To investigate the CO poisoning effect, the co-adsorption of CO and ethylene were studied on the Pt(111) single crystal. Previous studies have shown that the adsorbed ethylene molecules form ethylidyne on the Pt(111) surfaces at room temperature, and that these strongly-bonded ethylidyne molecules are spectators in ethylene hydrogenation reactions.^{20, 21} The results presented in this chapter indicate that the adsorbed ethylidyne molecules could be partially displaced by introducing high pressures of CO. However, when the surface was covered with a monolayer of CO, ethylene molecule could not effectively adsorb on the Pt(111) surface even in the presence of high pressure ethylene. This translates into CO blocking the active sites and inhibiting the catalytic activity. The SFG study confirmed the GC data from Chapter 5, in that the measured apparent activation energy for the ethylene hydrogenation reaction in the presence of 3 Torr of CO was 20 kcal/mol, which is double that of the unpoisoned reaction (~10 kcal/mol).

For several years researchers have noted the enhancement of optical fields at small, silver particles. These effects are noted in Raman^{22, 23, 24, 25, 26}, hyper Raman²⁷, two-photon adsorption²⁸, second harmonic generation (SHG)^{22, 29, 30}, and four wave mixing³¹, with most experiments devoted to understanding surface enhanced Raman scattering (SERS). These experiments focus primarily on the electromagnetic

enhancement mechanism rather than the chemical mechanisms for the increased signals. The electromagnetic enhancement mechanism states that when electromagnetic waves interact with a metal particle much smaller than the wavelength of incident light, surface plasmons are excited, resulting in increased electromagnetic field intensities at the surface. The increased surface intensity thus leads to larger surface signals. However, the chemical enhancement mechanism is due primarily to the adsorbed molecule forming a type of surface complex with the metal. This new surface complex then contains new electronic energy levels with which electromagnetic waves may be resonant.^{32, 33, 34} Many researcher now believe both effects contribute to the observed enhancement, with the dominant effect dictated by the system of investigation.^{22, 24, 26, 35} In the SFG study of the Pt nanoparticles, the electromagnetic enhancement mechanism is favored, over a chemical one, since a pure electromagnetic argument accounts for the intensity increases observed. The SFG signal of CO adsorbed to the Pt nanoparticles exhibits an enhancement of $10^4\times$ compared to CO adsorbed on a smooth Pt film. Although the SFG signal originates from CO on the metal particles, polarization studies indicate the optical properties are heavily influenced by the oxide-layer on the Si(100) wafer. Even though the surface area is low for the Pt nanoparticle array, as shown in Chapter 4 ($< 5\%$ ML), there are large electromagnetic enhancements exhibited at the surface of small metal nanoparticles.

6.2 Experimental

6.2.1 SFG Configuration for Pt(111) and Pt Nanoparticles

The details of the laser system for both model catalyst systems was detailed in Chapter 2. For the Pt(111) single crystal, an ultrahigh vacuum–high pressure (UHV–HP) system with a base pressure less than 3×10^{-10} Torr was used for sample preparation. This allowed for the cleaning and characterization of the Pt(111) single crystal in UHV as well as the transfer, under UHV, to the high-pressure reaction cell for SFG measurements. The Pt(111) crystal was cleaned by cycles of Ar^+ sputtering, heating in O_2 and annealing. A detailed description of the UHV–HP system and cleaning procedures has been described in the literature.³⁶ The CO (> 99%, Scott specialty gases) was purified through a liquid nitrogen cold trap before being used; ethylene purchased from Matheson was used directly without further purification. After the last cycle of cleaning and annealing, the Pt(111) crystal was first exposed to saturation coverage of CO or ethylene, depending on the experimental requirements. The sample was then transferred to the high-pressure reaction cell where SFG spectra were collected at room temperature for the co-adsorption studies. During the ethylene hydrogenation reaction, both SFG spectra and gas phase composition (using a GC) were monitored at the same time.

For the nanoparticles, a small reaction cell was constructed to house the array; this system was mobile and was simply rolled next to the laser table. Care was taken in the alignment of the cell to the incoming and outgoing beams (reference marks were made for quick alignment). The cell itself was pumped by a turbomolecular pump that yielded a base pressure of 10^{-10} torr. A gas manifold was constructed for the pre-mixing of

reaction gases. The sample was cleaned via cycles of oxidizing and reducing atmospheres along with heating. At the time, this was thought to be a successful cleaning procedure. It has since been determined that this cleaning procedure is insufficient for the nanoparticle sample. Accordingly, the results of the SFG spectra have been corrected for typical surface contaminations (carbon and oxygen). The sample was attached to a ceramic BN heater, and the cell was equipped with a cooling line that introduced N₂ gas that was sent through a liquid nitrogen bath.

6.2.2 Alumina-Supported Pt Nanoparticle Arrays Fabricated by Electron Beam Lithography (EBL)

The details of the fabrication process and the characterization of the Pt nanoparticles has been detailed in previous chapters.

6.3 Results and Discussion

6.3.1 CO/Ethylene Co-Adsorption Study on Pt(111)

To investigate the influence of co-adsorbed ethylene to the CO bonding, the Pt(111) surface was first pretreated with 10 L of ethylene at 330 K, forming a saturation layer of ethylidyne ($\theta = 0.25$). Figure 6.1 shows the surface vibrational taken from the ethylidyne-pretreated surface at various CO pressures; Figure 6.1a covers the CO stretching region at various CO pressures while Figure 6.1b covers the CH stretching region. For comparison, the surface vibrational spectra of pure CO and ethylene on the Pt(111) surface are shown in Figure 6.2a and 6.2b, respectively. When the ethylidyne-

pretreated surface was exposed to 10^{-7} Torr of CO, a resonance feature with a very broad linewidth around 2020 cm^{-1} was observed (Figure 6.1a). This peak was about 75 cm^{-1} red-shifted from the IR absorption frequency of atop CO on a clean Pt(111) surface (Figure 6.2a). The vibrational signature of ethylidyne can be seen by the resonance feature around 2880 cm^{-1} (Figure 6.1b), which is assigned to the symmetric CH_3 stretching mode of the ethylidyne molecules. This resonance feature was similar to those observed for pure ethylidyne adsorbed on the Pt(111) surface (Figure 6.2b). The CO vibrational peak grew as the CO pressure increased, becoming sharper and getting shifted toward higher frequency. At the same time, the symmetric CH_3 stretching intensity decreased with increasing CO pressures. In the high CO pressure region (> 1 Torr), no clear resonance peak can be identified. However, some resonant features in the CH stretching region recovered after evacuating the high-pressure CO from the reaction cell, indicating that this process may be partially reversible.

The disappearance of the CH stretching peak may also indicate that high-pressure CO may displace the ethylidyne molecules from the Pt(111) surface. To determine the composition of surface species, TPD spectra were taken at various of CO dosages on the ethylidyne-pretreated Pt(111) surface (Figure 6.3). In the absence of CO, ethylidyne TPD spectra showed a hydrogen desorption peak (mass 2) around 530 K, which was slightly higher than previous observations for the ethylidyne dehydrogenation temperature at 500 K.^{21, 37, 38} A shoulder around 480 K was observed when ethylidyne molecules co-adsorbed with CO; at this temperature, desorption peaks at masses 28 and 27 were observed. In the presence of high pressure CO (> 1 Torr), the major hydrogen desorption peak was shifted to 550 K. The integrated intensity decreased by $\sim 25\%$,

indicating high-pressure CO only displaces some of the ethylidyne molecules on the surface.

The co-adsorption effect in the presence of high-pressure ethylene was also investigated. The Pt(111) surface was pretreated with 5 L of CO at 300 K, forming a saturation layer of CO on the surface ($\theta = 0.5$). The high-pressure cell was then slowly filled with ethylene. At 10^{-7} Torr of ethylene, a CO resonance peak around 2095 cm^{-1} was observed, as shown in Figure 6.4a. As the ethylene pressure increased, the atop CO peak position red-shifted to 2080 cm^{-1} , while the peak intensity remained roughly the same. In the CH stretching region, as seen in Figure 6.4b, a very weak peak around 2880 cm^{-1} with a shoulder around 2920 cm^{-1} was observed when 5 L of ethylene was added to the CO-pretreated Pt(111) surface. These resonance features did not change as the pressure of ethylene was increased up to 35 Torr. Because no spectral evolution was observed, it is suggested that ethylene molecules cannot absorb on the Pt(111) surface, even in the presence of high-pressure ethylene, when the surface is covered with a monolayer of CO. The collision frequency of ethylene is $\sim 10^7/\text{site/s}$ at 35 Torr. Under such a severe condition, a monolayer of CO remains detectable and stable on the surface, implying that CO can block the sites for ethylene adsorption, which in turn explains the poisoning of the ethylene hydrogenation reaction.

CO and ethylene adsorption on the Pt(111) surface has been well studied in UHV and high-pressure environments.^{12, 20, 39, 40, 41} However, little work exists on the co-adsorption of these two species.¹¹ It is known that CO can induce ordering when co-adsorbed with ethylene on the Rh(111) surface, forming a $c(4\times 2)$ structure in the temperature range of 220-400 K.⁴² It was believed that co-adsorbing oppositely oriented

dipoles would strongly promote the formation of ordered co-adsorbed structures.⁴³ However, no ordered structure was observed when CO and ethylene co-adsorbed on the Pt(111) surface. Ethylene molecules alone adsorb on the Pt(111) surface, forming di- σ bonded ethylene at temperatures below 230 K. This species is sp^3 hybridized and resides in an fcc three-fold hollow site on the Pt(111) surface with a saturation coverage of 0.25 ML, as determined by LEED.⁴⁴ As the temperature increases, the di- σ bonded ethylene molecules dehydrogenate into ethylidyne and hydrogen atoms. From TPD spectra, it was found that the surface hydrogen generated in the formation of ethylidyne desorbs at 300 K, leaving ethylidyne on the Pt(111) surface. Like di- σ bonded ethylene, ethylidyne is also adsorbed in an fcc three-fold hollow site. At temperatures higher than 450 K, ethylidyne molecules further dehydrogenate to form graphitic precursor (C_2H , CH , etc.) species on the Pt surface. At very high temperatures (> 730 K), graphite is believed to be the main species remaining on the metal surface.⁴⁵ Under high-pressure conditions, it was found that at 230-300 K, di- σ bonded ethylene is in equilibrium with gas-phase ethylene, which suppresses the rate of formation of ethylidyne.²⁷

CO molecules adsorb intact on the Pt(111) surface. Under UHV conditions, CO forms a $c(4\times 2)$ structure at saturation coverage ($\theta = 0.5$). Both atop and bridge CO molecules co-exist in this configuration, showing separate IR adsorption peaks at 2095 and 1850 cm^{-1} . As the temperature increases, CO undergoes an order-disorder transition, and a diffuse $c(4\times 2)$ pattern was observed by LEED. At high CO pressures, only the atop CO peak was observed at 2095 cm^{-1} by SFG. The disappearance of bridge-bonded CO peak was attributed to the strong temperature dependence of its linewidth, which reduced the SFG signal by one order of magnitude when the temperature was increased from 150

to 300 K.⁴⁶ Such spectral broadening effects made it difficult to detect the bridge-bonded CO by SFG at room temperature. The atop CO peak showed little dependence on pressure and could be seen even in the presence of 400 Torr of CO. Under high pressure and temperature conditions (400 Torr, 400°C), CO undergoes the Boudouard reaction, leaving carbon on the surface.²⁵

When the ethylidyne-pretreated Pt(111) crystal was exposed to 10^{-7} Torr of CO at 300 K and a peak at 2020 cm^{-1} appeared, the assignment was made of CO adsorbed on the atop site. The absolute SFG intensity was 7 times weaker than those observed on the clean Pt(111) surface. The peak width of this atop CO species ($2\gamma = 34 \text{ cm}^{-1}$) is much wider than the peak width of atop CO on the clean Pt(111) surface ($2\gamma = 16 \text{ cm}^{-1}$). This spectral consequence is explained by the inhomogeneous broadening effect. Since the surface was pretreated with ethylene that forms ethylidyne and hydrogen atoms on the surface, the adsorbed CO could experience different environments depending on the adsorption site. Assigning the peak to atop CO also meant that even in the presence of ethylidyne molecules, CO still occupied the atop position. This observation is different from those observed for Pd catalysts supported on silica, in which ethylidyne blocked the CO adsorption on the (111) sites in Pd/SiO₂ catalysts.⁴⁷

There are three distinct effects that can lead to the reduction in the CO stretching frequency (red shift) for adsorbed CO in the presence of ethylidyne²⁹: 1) reduction in dipole–dipole interaction; 2) vibrational Stark effect, where the frequency shift is proportional to the electric field exerted on CO by the co-adsorbed species; and 3) charge back-donation from the metal surface to the $2\pi^*$ orbital of adsorbed CO. Using isotopic dilution, it was concluded that this red shift was mainly due to the reduction of the

dipole-dipole coupling effect and not the weakening of CO bonding. However, it is known that the singleton frequency of CO, which is the CO absorption frequency in the absence of dipole-dipole interactions, on the Pt(111) surface is 2063 cm^{-1} .⁹ The reduction in dipole-dipole coupling effect should not introduce a frequency shift lower than 2063 cm^{-1} . It was found that the dipole–dipole coupling effect accounted for 15 cm^{-1} out of the observed 25 cm^{-1} shift in the ethylene pretreated Pt/SiO₂ catalysts.¹ The Stark effect is important when CO is co-adsorbed with a species that has a very large surface dipole moment. However, the surface dipole moment for ethylidyne molecules is relatively small (0.9 D on the Rh(111) surface). It was estimated that this surface dipole moment could generate a 30 cm^{-1} frequency shifts.²⁹ Therefore, the rest of the frequency shift should be attributed to the surface charge transfer. Ethylidyne is known to be an electron donor. When ethylidyne co-adsorbed with CO, the excess electron charge on the surface will weaken the CO bond through a d- π back donating mechanism.⁴⁸ As a result, the vibrational frequency of the atop CO co-adsorbed with ethylidyne could show a large red-shift. This result indicates that CO adsorption on the hydrocarbon-covered surface could lead to the weakening of CO bond, which is a prerequisite of catalytic CO hydrogenation. CO dissociation on the Pt(111) at high CO pressure and high temperature was observed in previous measurements. The observed CO peak frequency also showed a large red-shift, which was the result of the co-adsorption of CO with surface carbons.

As the CO pressure increases, the CO peak intensity increased, indicating an increase in the surface CO concentration. This also caused a frequency shift towards higher frequency due to the increase of CO–CO lateral interactions on the Pt(111) surface. In the same time, the CH₃ stretching intensity of ethylidyne decreased with

increasing CO pressure.⁴⁹ The atop CO peak intensity increases at the expense of the ethylidyne peak, indicating that CO may displace ethylidyne molecules on the surface. At high CO pressures, no dominant resonance feature in the CH stretching region can be seen. It was concluded that CO molecules completely displace ethylidyne on the platinum surface. However, if this is the case, an atop CO resonance peak at 2095 cm^{-1} should be observed. The absolute atop CO peak intensity at high CO pressures is almost 4 times weaker than those observed on the clean Pt(111) surface; the fact that the atop CO peak is at 2040 cm^{-1} indicates that there is still a considerable amount of hydrocarbons on the surface. TPD spectra showed that after exposure to 1 Torr of CO, only 25% of ethylidyne molecules were displaced, the majority still stayed on the Pt(111) surface. One possible explanation for the disappearance of the CH resonance feature at high CO pressures is that high-pressure CO may induce orientation disordering for the ethylidyne molecules. Since the SFG technique is very sensitive to polar ordering, orientation disorder can cause SFG intensity to drop significantly. SFG is measuring the average dynamic dipole moment along the surface normal, so any change in net orientation will alter the peak intensity. Ethylidyne is known to adsorb in the upright direction on the Pt(111) surface. Therefore, any orientation change of ethylidyne molecules will reduce the net dynamic dipole moment along the surface normal direction. This is supported by the partial recovery of the CH resonance feature after evacuating the high-pressure CO, when ethylidyne molecules can relax to their upright configuration, as observed in UHV. An alternative explanation for the disappearance of CH resonance feature could be attributed to the modification of optical response in the presence of strong vibrational dipole moment of the co-adsorbed CO.^{11, 28}

At high CO pressures, there are 2 resonance features in the CO stretching region; a dominant peak at 2040 cm^{-1} and a shoulder at 2020 cm^{-1} . This indicates that there may exist 2 types of atop CO chemical environments similar to those observed in the CO/H₂O co-adsorption experiment.⁵⁰ The more intense high-frequency peak can be assigned to the CO molecules that form CO islands, where the dipole-dipole interaction is strong. The low-frequency peak can be assigned to the isolated CO molecules that are adjacent to ethylidyne molecules. These assignments have not been confirmed.

When the Pt(111) surface was pretreated with CO, no noticeable change of vibrational spectra was observed as the pressure of ethylene was increased up to 35 Torr. This result indicates that in the presence of a monolayer of CO and at room temperature, ethylene cannot adsorb on the surface. This may lead to poisoning of the catalytic reactions that require ethylene adsorption.

6.3.2. CO-Poisoning of Ethylene Hydrogenation on the Pt(111) Surface

To understand how CO molecules poison the ethylene hydrogenation reaction, the Pt(111) surface was pretreated with 10^{-7} , 10^{-5} , 0.1, and 3 Torr of CO. Then 10 Torr of ethylene and 100 Torr of hydrogen and 650 Torr of argon were added to the high-pressure reaction cell. Under these conditions (high pressure of CO, > 0.1 Torr), no ethane produce was observed at room temperature. The CO poisoning effect can be clearly seen from Figure 6.5, where the ethylene hydrogenation reaction was terminated by the introduction of 3 Torr CO. The reaction product was only detected at higher temperatures ($> 400\text{ K}$). Figure 6.6 shows the vibrational spectrum in the CO stretching region under reaction conditions in the presence of 3 Torr of CO at various temperatures.

No change in the CO resonance features was seen at low temperatures. At higher temperatures, the CO peak red-shifts and decreases in intensity. Similar behavior was observed for pure CO adsorbed on the Pt(111) surface.²⁵ The reaction turnover rates above 423 K were used to determine the activation energy for the CO-poisoned ethylene hydrogenation reaction (Figure 6.7). The activation energy was calculated to be (20.5 ± 2) kcal/mol, which was much higher than the 10.8 kcal/mole activation energy needed for the ethylene hydrogenation on the Pt(111) surface in the absence of any CO.⁵¹

The adsorption of ethylene requires two platinum sites, which are blocked by the adsorbed CO. This site blocking effect may lead to the poisoning of the catalytic reactions that require ethylene adsorption. This clearly indicates that CO is blocking the sites needed for the ethylene hydrogenation reaction to occur. This result suggests that the activation energy for such reaction is the heat of desorption of CO, which is to remove CO from the surface to allow ethylene adsorption and then hydrogenation on the platinum surface. It should be mentioned that the reactivity of ethylene hydrogenation on the Pt(111) surface was completely poisoned only at high CO pressures. At low CO pressures (10^{-7} , 10^{-5} Torr), the ethylene hydrogenation rate was still detectable. One possible explanation is that high pressure hydrogen (100 Torr) may react with or displace CO, which is supported by the disappearance of CO resonance feature upon the introduction of high pressure hydrogen in this CO pressure region.

6.3.3 CO on Pt Nanoparticles

Figure 6.8 is the spectrum of CO (~1 atm) on a platinum film with ssp and ppp polarization combinations (1st s = sum frequency, 2nd s = visible, p = infrared). The peak

at 2100 cm^{-1} is due to top-site CO coordinated to one Pt atom. The intensity of the ppp spectrum is ~ 8 times more intense, as predicted by Fresnel's equations for surface intensities at a metal surface. Figure 6.9 is the SFG spectrum of CO on Pt nanoparticles. The CO peak is shifted by $\sim 15\text{ cm}^{-1}$.

The SFG intensity measured is a dependant on the particle size, shape, composition, interparticle spacing, and substrate. Size, shape, and composition effects are modeled with the idea that small particle surface plasmons are excited, thus enhancing the local fields. These local field are dependant on the size, shape and dielectric constant of the material. The particle spacing affects the coupling between particles as well as any dispersion effects of the array. Finally, the dielectric properties of the substrate influence the macroscopic fields at the surface, which is determined by the metal coverage. The enhancement at small metal particles is based on Mie resonance criteria.^{29, 52, 53, 54}

The surface coverage of the Pt nanoparticles is roughly 5% of a monolayer, which approaches the detection limits for typical vibrational spectroscopies. The spectra demonstrate the excellent signal-to-noise obtained with SFG, even with 1 atm of CO. There is only one peak in the SFG spectrum, and it is due to the top site CO at 2105 cm^{-1} , which is identical to the CO assignment on polycrystalline platinum surfaces.⁵⁵ This proves the power of SFG to study these nanocatalysts, and further studies should be investigated to gain insight into bonding and mechanisms under reaction conditions.

6.4 Conclusion

When CO adsorbed on the ethylidyne pretreated surface, its vibrational spectra red-shifted about 75 cm^{-1} to 2020 cm^{-1} , which is mainly due to the weakening of CO bond through d- π back donation from co-adsorbed ethylidyne molecules. As CO pressure increases, the resonance frequency of atop CO shift to 2040 cm^{-1} and the peak width decreases, indicating the formation of CO islands. At the same time, the CH_3 stretching mode of ethylidyne diminishes, which could be the result of induced orientation changes of ethylidyne molecules by high-pressure CO. In the CO pretreated Pt(111) surface, the presence of high pressure ethylene does not change the vibrational spectra in the CH stretching region, indicating that ethylene cannot adsorb on the surface that is covered by a monolayer of CO. During the studies of catalytic ethylene hydrogenation in the presence of CO, data showed that CO poisons the catalytic reaction by the site blocking effect up to 400 K, which is the temperature at which CO desorbs from the Pt(111) surface. CO poisons the catalytic reaction even above its desorption temperature, indicating that adsorbed CO is in equilibrium with gas phase CO, which blocks the ethylene adsorption site where hydrogenation occurs. The measured apparent activation energy was 20.5 kcal/mol instead of 10 kcal/mol. The mechanism for the poisoning of the reaction on the single crystal helps solidify the mechanism of why the nanoparticles can still show ethylene hydrogenation turnover in the presence of CO. The occupation of CO on the nanoparticles was elucidated with SFG. The promising results indicate that further SFG studies should be performed on these nanocatalysts. In order to further elucidate the fundamentals of ethylene hydrogenation, a 2nd-generation model nanocatalyst was developed. The next chapter will outline similar studies (poisoned and

unpoisoned ethylene hydrogenation) on Pt nanowires fabricated by size reduction lithography and nanoimprint lithography.

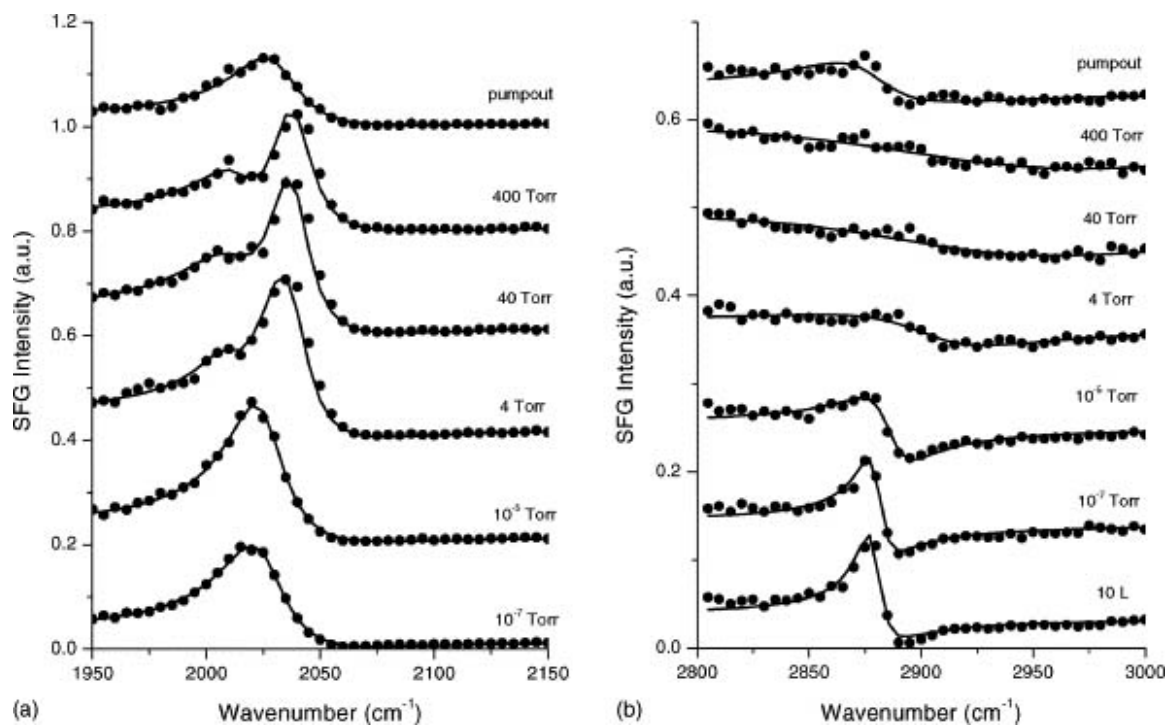


Figure 6.1. SFG spectra of the Pt(111) surface pretreated with 10 L of ethylene at 330K at various CO pressures. a) in the CO stretching region and b) in the CH stretching region. Circles are experimental data and the solid lines are fitted curves.

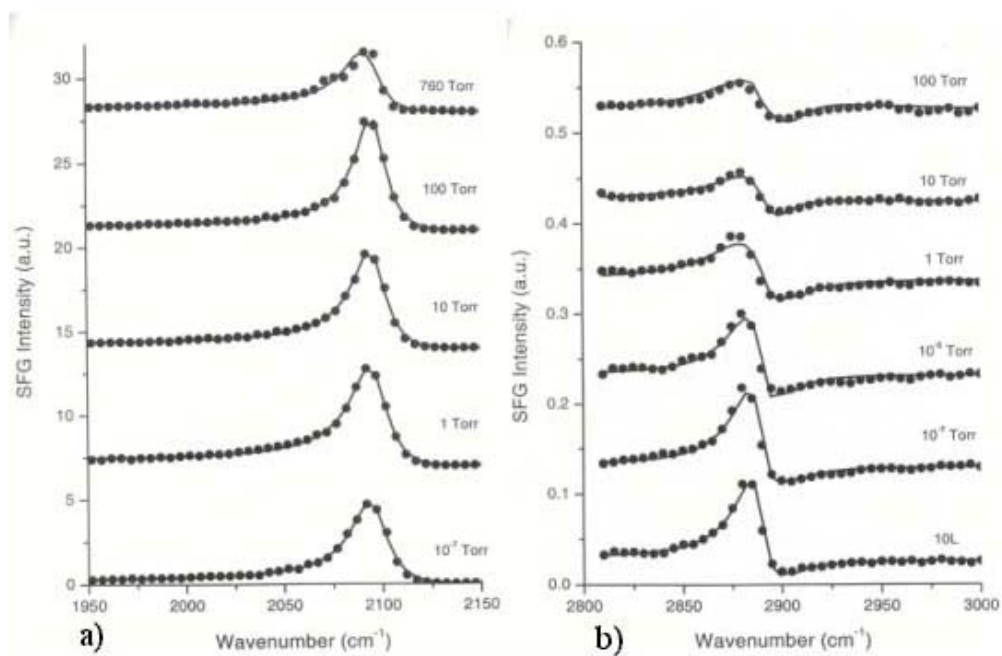


Figure 6.2. a) SFG spectra of pure CO at various CO pressures. B) SFG spectra of ethylidyne at various ethylene pressures.

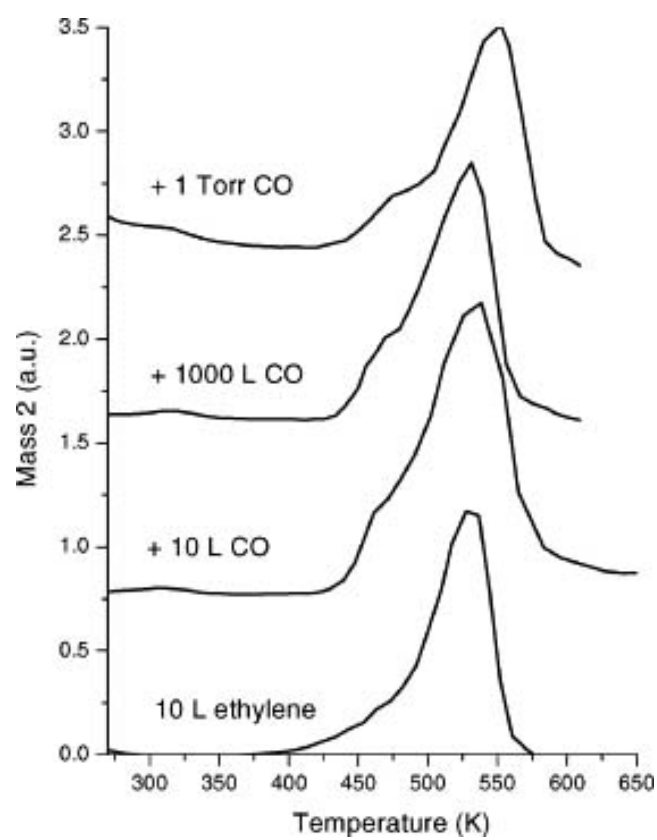


Figure 6.3. TPD (mass 2) spectra from the ethylene-pretreated Pt(111) at different CO dosages.

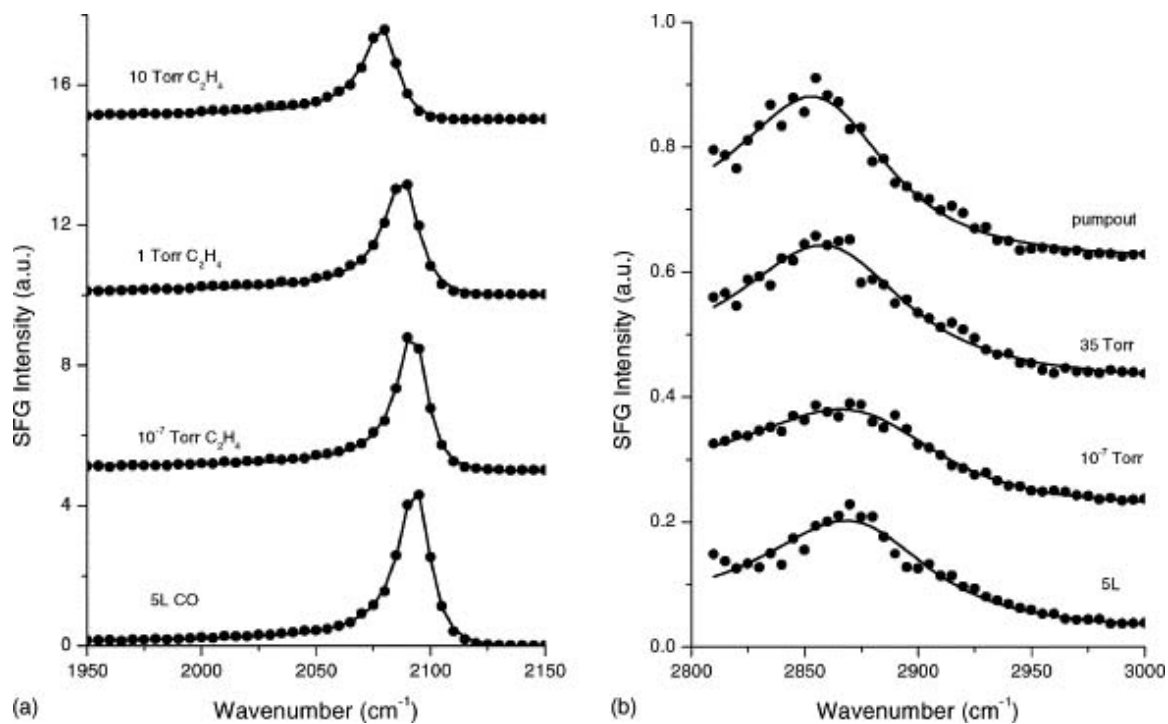


Figure 6.4. a) SFG spectra of the Pt(111) surface pretreated with 5 L of CO at 300 K in the CO stretching region at various ethylene pressures. b) SFG spectra of the 5 L CO-pretreated Pt(111) surface in the CH stretching region at 5 L, 10^{-7} Torr, 35 Torr of ethylene, and after evacuating gas phase ethylene (pressure $<10^{-8}$ Torr).

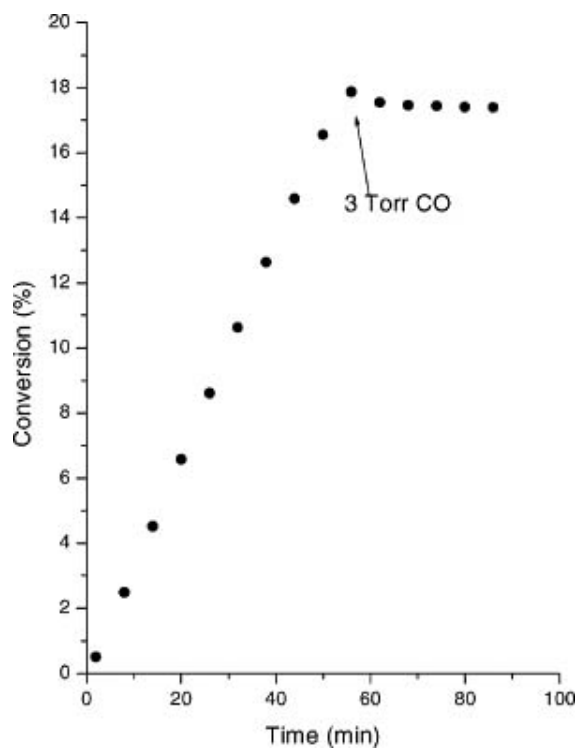


Figure 6.5. The conversion efficiency of the ethylene hydrogenation reaction: 10 Torr ethylene, 100 Torr hydrogen, and 650 Torr argon. No further ethane production was observed upon the introduction of 3 Torr of CO.

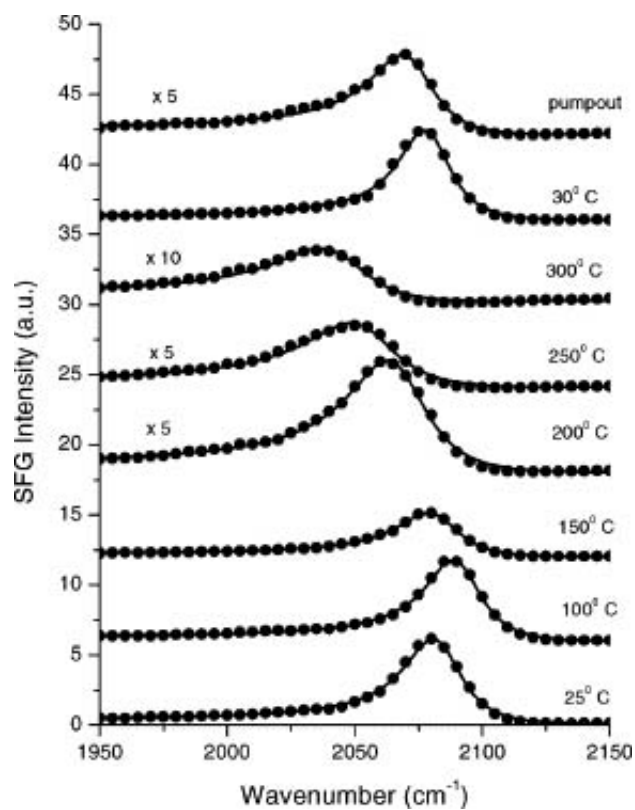


Figure 6.6. SFG spectra (CO stretching region) of the Pt(111) surface during the ethylene hydrogenation reaction in the presence of 3 Torr CO at various temperatures. Gas phase compositions are 3 Torr CO, 10 Torr ethylene, 100 Torr hydrogen, and 650 Torr argon.

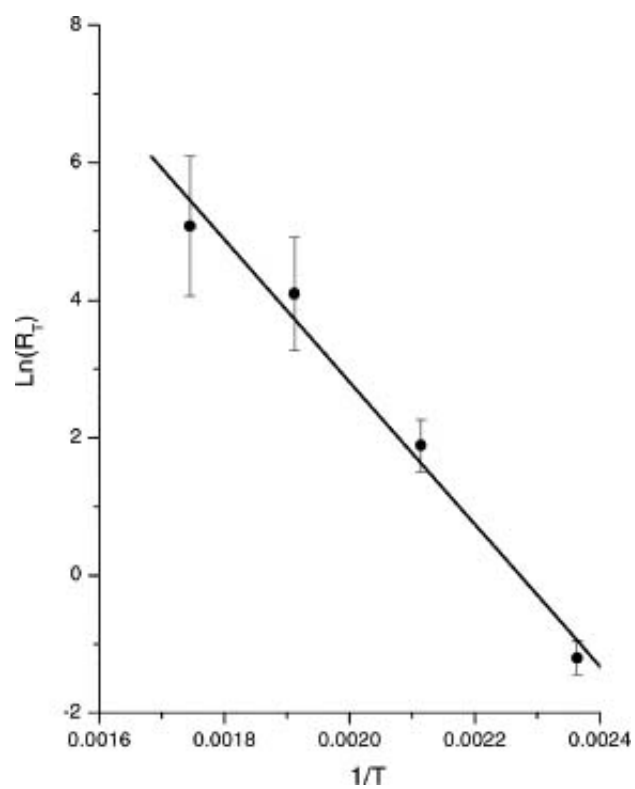


Figure 6.7. Using the reaction turnover rate at temperatures higher than 400 K, the measured activation energy of the CO-poisoned ethylene hydrogenation reaction was calculated to be (20.5 ± 2) kcal/mol.

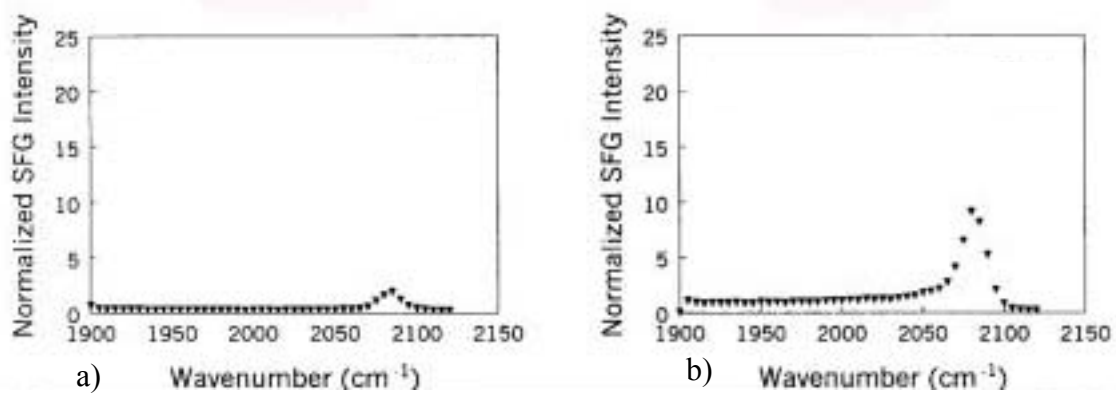


Figure 6.8. SFG spectra of CO adsorbed on a smooth Pt film. Shown are spectra taken with ssp (a) and ppp (b) polarizations.

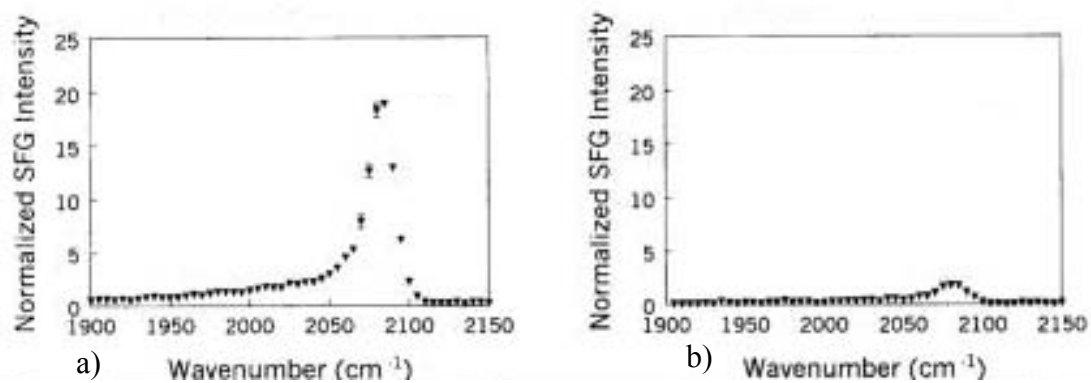


Figure 6.9. SFG spectra of CO adsorbed on Pt nanoparticles. Shown are spectra taken with ssp (a) and ppp (b) polarizations.

References

-
- ¹ Stoop, F.; Toolenaar, F.J.C.M.; Ponec, V. *J. Catal.* **1982**, *73*, 50.
- ² Ertl, G.; Knozinger, H.; Weitkamp, J., eds. *Handbook of Heterogeneous Catalysis*. Wiley-VCH, Weinheim, Germany, 1997.
- ³ Oudar, J.; Wise, H., eds. *Deactivation and Poisoning of Catalysts*. Dekker, New York, 1985.
- ⁴ Hayden, B.W.; Bradshaw, A.M. *Surf. Sci.* **1983**, *125*, 787.
- ⁵ Trenary, M.; Uram, K.J.; Yates, J.T. *Surf. Sci.* **1985**, *157*, 512.
- ⁶ Kuhn, W.K.; Szanyi, J.; Goodman, D.W. *Surf. Sci.* **1992**, *274*, L611.
- ⁷ Hollins, P.; Pritchard, J. *Prog. Surf. Sci.* **1985**, *19*, 275.
- ⁸ Tushaus, M.; Schweizer, E.; Hollins, P.; Bradshaw, A.M. *J. Elec. Spec. Rel. Phenom.* **1987**, *44*, 305.
- ⁹ Crossley, A.; King, D.A. *Surf. Sci.* **1977**, *68*, 528.
- ¹⁰ Niemantsverdriet, J.W. *Spectroscopy in Catalysis*. Wiley-VCH, Weinheim, Germany, 2000.
- ¹¹ Ainsworth, M.K.; McCoustra, M.R.S.; Chesters, M.A.; Sheppard, N. De La Cruz, C. *Surf. Sci.* **1999**, *437*, 9.
- ¹² Su, X.C.; Cremer, P.S.; Shen, Y.R.; Somorjai, G.A. *Phys. Rev. Lett.* **1996**, *77*, 3858.
- ¹³ Su, X.C.; Cremer, P.S.; Shen, Y.R.; Somorjai, G.A. *J. Am. Chem. Soc.* **1997**, *119*, 3994.
- ¹⁴ Harle, H.; Metka, U.; Volpp, H.R.; Wolfrum, J. *Phys. Chem. Chem. Phys.* **1999**, *1*, 5059.
- ¹⁵ Harle, H.; Lehnert, A.; Metka, U.; Volpp, H.R.; Willms, L.; Wolfrum, J. *App. Phys. B-*

-
- Lasers and Optics* **1999**, 68, 567.
- ¹⁶ Cremer, P.S.; Su, X.C.; Shen, Y.R.; Somorjai, G.A. *J. Am. Chem. Soc.* **1996**, 118, 2942.
- ¹⁷ Cremer, P.S.; Su, X.C.; Shen, Y.R.; Somorjai, G.A. *J. Phys. Chem.* **1996**, 100, 16302.
- ¹⁸ Cremer, P.S.; Su, X.C.; Somorjai, G.A.; Shen, Y.R. *J. Molec. Cat. A-Chem.* **1998**, 131, 225.
- ¹⁹ Su, X.C.; Kung, K.Y.; Lahtinen, J.; Shen, Y.R.; Somorjai, G.A. *J. Molec. Catal. A-Chem.* **1999**, 141, 9.
- ²⁰ Cremer, P.S.; Stanners, C.; Niemantsverdriet, J.W.; Shen, Y.R.; Somorjai, G.A. *Surf. Sci.* **1995**, 328, 111.
- ²¹ Zaera, F. *Langmuir* **1996**, 12, 88.
- ²² Chen, C. K.; Heinz, T. F.; Ricard, D.; Shen, Y. R. *Phys. Rev. B* **1983**, 27, 1965.
- ²³ Gersten, J. I. *J. Chem. Phys.* **1980**, 72, 5779.
- ²⁴ Mills, D. L.; Weber, M. *Phys. Rev. B* **1982**, 26, 1075.
- ²⁵ Nie, S.; Emory, S. R. *Science* **1997**, 275, 1102.
- ²⁶ Pemberton, J. E.; Bryant, M. A.; Sobocinski, R. L.; Joa, S. L. *J. Phys. Chem.* **1992**, 96, 3776.
- ²⁷ Golab, J. T.; Spague, J. R.; Carron, K. T.; Schatz, G. C.; Duyne, R. P. V. *J. Chem. Phys.* **1988**, 88, 7942.
- ²⁸ Das, P. C.; Metiu, H.; Puri, A. *J. Chem. Phys.* **1988**, 89, 6497.
- ²⁹ Berkovic, G.; Efrima, S. *Langmuir* **1993**, 9, 355.
- ³⁰ Chen, C. K.; Castro, A. R. B. d.; Shen, Y. R. *Phys. Rev. Lett.* 1981, 46, 145.
- ³¹ Chemla, D. S.; Heritage, J. P.; Liao, P. F.; Isaacs, E. D. *Phys. Rev. B* **1983**, 27, 4553.

-
- ³² Hallmark, V. M.; Campion, A. *J. Chem. Phys.* **1986**, *84*, 2933.
- ³³ Kambhampati, P.; Child, C. M.; Campion, A. *J. Chem. Soc. Faraday Trans.* **1996**, *92*, 4775.
- ³⁴ Kambhampati, P.; Child, C. M.; Foster, M. C.; Campion, A. *J. Chem. Phys.* **1998**, *108*, 5013.
- ³⁵ Lipkowski, J.; Ross, P.N., eds. *Adsorption of Molecules at Metal Electrodes*. VCH Publishers, New York, 1991.
- ³⁶ Kung, K.Y.; Chen, P.; Shen, Y.R.; Somorjai, G.A. *Rev. Sci. Instrum.* **2001**, *72*, 245.
- ³⁷ Salmeron, M.; Somorjai, G.A. *J. Phys. Chem.* **1982**, *86*, 341.
- ³⁸ Creighton, J.R.; White, J.M. *Surf. Sci.* **1983**, *129*, 327.
- ³⁹ Kung, K.Y.; Chen, P.; Wei, F.; Shen, Y.R.; Somorjai, G.A. *Surf. Sci.* **2000**, *463*, L627.
- ⁴⁰ Ertl, G.; Neumann, M.; Streit, K.M. *Surf. Sci.* **1977**, *64*, 393.
- ⁴¹ Ohtani, T.; Kubota, J.; Kondo, J.N.; Hirose, C.; Domen, K. *Surf. Sci.* **1998**, *415*, L983.
- ⁴² Blackman, G.S.; Kao, C.T.; Bent, B.E.; Mate, C.M.; Van Hove, M.A.; Somorjai, G.A. *Surf. Sci.* **1988**, *207*, 66.
- ⁴³ Mate, C.M.; Kao, C.T.; Somorjai, G.A. *Surf. Sci.* **1988**, *206*, 145.
- ⁴⁴ Starke, U.; Barbieri, A.; Materer, N.; Van Hove, M.A.; Somorjai, G.A. *Surf. Sci.* **1993**, *286*, 1.
- ⁴⁵ Yata, M.; Madix, R.J. *Surf. Sci.* **1995**, *328*, 171.
- ⁴⁶ Klunker, C.; Balden, M.; Lehwald, S.; Daum, W. *Surf. Sci.* **1996**, *360*, 104.
- ⁴⁷ Beebe, T.P.; Yates, J.T. *Surf. Sci.* **1986**, *173*, L606.
- ⁴⁸ Blyholder, G. *J. Phys. Chem.* **1964**, *68*, 2772.
- ⁴⁹ Chen, P.; Kung, K.Y.; Shen, Y.R.; Somorjai, G.A. *Surf. Sci.* **2001**, *494*, 289.

-
- ⁵⁰ Kizhakevariam, N.; Villegas, I.; Weaver, M.J. *J. Phys. Chem.* **1995**, *99*, 7677.
- ⁵¹ Zaera, F.; Somorjai, G.A. *J. Am. Chem. Soc.* **1984**, *106*, 2288.
- ⁵² Wokaun, A.; Bergman, J. G.; Heritage, J. P.; Glass, A. M.; Liao, P. F.; Olson, D. H. *Phys. Rev. B* **1981**, *24*, 849.
- ⁵³ Mills, D. L. *Nonlinear Optics*. 2nd ed., Springer-Verlag, New York, 1998.
- ⁵⁴ Liao, P. F.; Stern, M. B. *Opt. Lett.* **1982**, *7*, 483.
- ⁵⁵ Sheppard, N.; Nguyen, T. T. *Adv. Infrared Raman Spectros.* **1978**, *5*, 67

Chapter 7

Ethylene Hydrogenation and CO-Poisoned Ethylene Hydrogenation on Alumina-Supported Pt Nanowire Array Model Catalysts Fabricated by Size Reduction Lithography and Nanoimprint Lithography

7.1 Introduction

The metal-catalyzed hydrogenation of ethylene was discovered by Sabatier¹, and it was an important part of his Nobel Prize winning research. This was the first catalytic reaction for which a mechanism was proposed in 1934 by Horiuti and Polanyi², which postulated hydrogen molecule dissociation on the metal surface and the sequential

hydrogenation of ethylene to C_2H_5 and then to C_2H_6 . As extensively detailed in previous chapters, researchers since the late seventies have been engaged in molecular studies of the mechanism of this reaction on platinum and rhodium crystal surfaces, and a detailed picture of many of the elementary reaction steps has emerged. Using low energy electron diffraction (LEED) and sum frequency generation (SFG)-surface vibrational spectroscopy, the structure of adsorbates has been determined.^{3, 4, 5, 6, 7} Three species: π -bonded ethylene (C_2H_4), di- σ bonded ethylene (C_2H_4), and ethylidyne (C_2H_3), have been identified on the surface under reaction conditions (Figure 7.1). The latter two species are bound to the metal surfaces strongly enough to be stable even in vacuum. π -bonded ethylene is weakly bound and present on the surface only at high pressures of hydrogen and ethylene under the reaction conditions. Scanning tunneling microscopy (STM) studies⁸ and modeling⁹ indicate that the ethylidyne species are mobile on the surface at 300 K shuttling between 3-fold fcc and hcp sites with an activation energy of 0.1 eV. Ethylidyne also restructures the Pt(111) and Rh(111) surfaces as it forms, as has been detected by LEED surface crystallography studies. These structures are shown in Figure 7.2.¹⁰ This restructuring is also confirmed by density functional theory studies.¹¹

A mechanism for ethylene hydrogenation involving several elementary reaction steps can be proposed based on experimental observations, as displayed in Figure 7.3. In this mechanism, hydrogen molecules adsorb dissociatively on an ethylidyne-covered metal surface. Ethylidyne diffusion between fcc and hcp 3-fold hollow sites opens up holes in the ethylidyne overlayer where π -bonded ethylene weakly adsorbs on the metal. The ethylene is then stepwise hydrogenated through an ethyl intermediate to ethane. Isotope exchange experiments indicate that ethylidyne is a spectator.¹² π -bonded

ethylene hydrogenation turnover accounts for most of the ethane that forms. Its concentration is only 4% of a monolayer. This mechanism was elucidated from experiments on Pt, and chemical reaction studies have shown that ethylidyne formation and stepwise hydrogenation of π -bonded ethylene are also mechanistically probable on Rh.¹³

It has been discovered that CO, when introduced in the reaction chamber during ethylene hydrogenation, poisons the catalytic reaction. In this chapter, experimental evidence is presented for this poisoning effect and mechanisms that explain this interesting effect based on reaction rates using single crystal and nanocatalysts are proposed.

New model systems are being developed in academic research labs that better resemble the industrial catalyst. The goal is to gain fundamental insight into the workings of the catalyst and the catalytic process. Work on single crystals and nanoparticles has truly elucidated catalytic reactions. But certain limitations of these model systems make the need for new systems a key concern. Single crystals, while perfect for the surface scientist, do not mirror the industrial catalyst that is typically metal nanoparticles dispersed on a high surface area support. Electron beam lithography has proven to be an invaluable tool for producing these nanoparticles with uniform sizes, spacings, and being able to easily vary the metal and type of support. However, this high-cost, low-throughput process produces nanocatalysts with only mm^2 of active metal surface area. For industrially significant reactions, at least cm^2 is necessary. Electron beam lithography is not suited to pattern such a large area. For this reason, size reduction lithography (SRL) was developed and utilized. This parallel process yields a wafer-scale

mask, with resolution comparable to EBL. When coupled with nanoimprint lithography (NIL), catalysts with cm^2 surface area can be reproducibly fabricated. To test the viability of this new model catalyst system, ethylene hydrogenation and CO-poisoned ethylene hydrogenation were investigated over Pt nanowires. This also enables the comparison of data across three generations of model catalysts: single crystal, nanoparticles, and now nanowires. Based on the data, new insight is gained into those parameters that are key for catalytic activity and selectivity.

7.2 Experimental

7.2.1 Size Reduction Lithography (SRL)

The fabrication steps were performed in the UC Berkeley Microfabrication Laboratory (Microlab) and a field emission scanning electron microscope (JEOL JSM-6340F) was used to characterize the obtained features in every step of the process. The overall scheme is shown in Figure 7.4. A Si(100) wafer was used as the starting material. A 50-70 nm thermal oxide layer was grown on the Si wafers in a water stream and oxygen (Figure 7.4b). The optimal thickness of the thermal oxide was selected based on the following functional considerations. The layer should be thick enough to protect the substrate during the removal of the sacrificial poly-Si layer; a thin layer is desired to minimize pattern broadening when forming the hard mask for subsequent silicon etching. A thin layer of poly-Si was deposited by LPCVD at 600°C to act as the sacrificial layer (Figure 7.4c). For improved mechanical stability, the layer thickness was 100 nm for generating Si features with sizes less than 30 nm and 400 nm for larger Si nanowires. The

poly-Si layer was then patterned by photolithography with a GCA 6200 wafer stepper, the resolution of which was ~ 600 nm. The pattern was transferred from the photoresist layer to the poly-Si layer by plasma etching in a Lam Research 9400 TCP etcher (Figure 7.4d). The conditions were 50 sccm Cl_2 , 150 sccm HBr , pressure 15 mTorr, electrode temperature 50°C , 300 W top electrode power, and 150 W bottom electrode power with a bias of -160 V. This recipe etched poly-Si with a speed of ~ 7 nm/s and produced a nearly vertical sidewall profile with an angle $> 89.5^\circ$. The residual polymer layer was removed after the etch step in order to reduce feature broadening. The estimated residue polymer thickness was 20-30 nm. The post-etch step for the removal of the polymer was to dip the wafer in (100:1) HF for 10 s, strip the photoresist with oxygen plasma, dip the wafer again in 100:1 HF for 10 s, followed by dipping in piranha [(4:1) H_2SO_4 : H_2O_2] treated at 120°C . Low temperature oxide (LTO: SiO_2) was deposited by LPCVD over the patterned poly-Si layer (Figure 7.4e). The conditions were 5 sccm SiH_4 and 70 sccm O_2 at 450°C . The deposition rate was ~ 3 nm/min. The step coverage was $\sim 70\%$ for thin films (< 50 nm) and $\sim 60\%$ for thicker films, as shown in Figure 7.5, parts a and b, respectively. The thickness of the deposited LTO on the sidewall determined the minimum feature size. Anisotropic plasma etching was used to remove the LTO on the top of the sacrificial structure and open the poly-Si structure (Figure 7.4f). The conditions were 100 sccm CF_4 , pressure 13 mTorr, 200 W top electrode power, and 40 W bottom electrode power with a bias of -80 V. The etching speed was ~ 2 nm/s for LTO. This recipe also etches poly-Si and single crystal silicon with almost the same speed as for the LTO. The poly-Si sacrificial layer was then removed with either wet etching or plasma etching (Figure 7.4g). Wet etching was conducted in 1:2_w KOH aqueous solution

at 80 °C; the etching speed was ~17 nm/s for poly-Si and ~0.1 nm/s for LTO. Due to the etching non-uniformity, the complete removal of poly-Si is generally not achieved until 2 min, and this severely undercuts the LTO spacer at the 10-nm scale. Therefore, wet etching is not used for spacers smaller than 30 nm; plasma etching is used instead. The poly-Si plasma etching process is the same as the process for transferring the pattern from photoresist into the poly-Si layer; the etching selectivity of poly-Si to LTO is 22. The LTO pattern was then transferred to the thermal oxide layer by plasma etching with conditions of 100 sccm CF₄, pressure 13 mTorr, 200 W top electrode power, and 40 W bottom electrode power (Figure 7.4h). The resulting oxide pattern sidewall profile after this etching is not ideally vertical, showing some broadening for smaller spacers (< 30 nm, Figure 7.5c) and a noticeable undercut for larger spacers (> 50 nm, Figure 7.5d). The oxide pattern was transferred to silicon by plasma etching with conditions of 50 sccm Cl₂, 150 sccm HBr, pressure 15 mTorr, electrode temperature 50°C, 300 W top electrode power, and 150 W bottom electrode power (Figure 7.4i). Silicon nanowires with 20 nm diameters are routinely fabricated with this process, as shown in Figure 7.5, parts e and f.

To reduce the silicon nanowire size further, the resulting 20-nm silicon nanowires were oxidized at 800°C for 20 min followed by HF dipping to remove the oxide. This treatment reduced the silicon dimension to ~12 nm, as shown in Figure 7.6a. A high-resolution TEM image also shows the single crystalline nature of the Si nanowires. Further oxidation at 800°C for 10 min reduced the silicon dimension to ~7 nm, as shown in Figure 7.6b. The concave shape of the cross section of the Si nanowires is due to a lower oxidation rate for concave and convex surfaces (top and bottom) than for planar surfaces (middle).^{14, 15}

The size-reduction process can be repeated by alternating poly-Si and SiO₂ as the sidewall and sacrificial materials, doubling the pitch with each cycle. Figure 7.7 shows dense 70-nm nanowires with 80-nm spacing that were fabricated over a full 4-inch wafer after three size-reduction repetitions that started with 0.6 μm optical lithography-defined features.

7.2.2 Nanoimprint Lithography (NIL)

Two of the most important issues in nanoimprint lithography are 1) good separation between the mask and the polymer-coated substrate and 2) conformal contact between the mask and the substrate. This second concern is non-trivial considering the imprint is performed over several cm², while the features on the mask may only be 100 nm tall. A slight separation, on the order of microns, can result in failure.

The 4-inch Si(100) mask that was fabricated from SRL was broken into quarters to fit the press. The separation issue can be solved by functionalizing the mask surface to create a low energy surface. This is accomplished by forming a fluorine terminated self-assembled monolayer on the mask surface with (tridecafluoro-1,1,2,2-tetrahydrooctyl)-1-trichlorosilane, (FTS, United Chemical Technologies, Inc. CAS number 78560-45-9), which serves as a release layer (Figure 7.8). To functionalize the surface of the mask, the mask was first dipped into piranha solution (2 L of 98%w sulfuric acid mixed with 100 mL of 49%w H₂O₂ solution at 120°C) to oxidize the organic contaminants, during which the silicon surface also formed a thin layer of oxide and silanol groups. The mask was then placed into a 500-mL glass petri dish with one drop (~0.01 gram) of diluted 10%w FTS in anhydrous octane and incubated in a 60°C oven for 5 min. Higher concentration

FTS solution will result in polymer formation on the mask surface, which will inhibit patterning effort in the sub-50 nm regime. The functionalized surface was then characterized with water contact angle measurement. The measurement was done on a plain Si(100) surface without any patterning and the results are shown in Figure 7.9. The contact angle was 17.1° right after piranha cleaning and oxidation, indicating a hydrophilic surface; less than 3 min after exposing to the FTS vapor at 60°C , the contact angle increased to above 90° , indicating a hydrophobic layer was formed. After 5 min, the contact angle increased to about 105° and this agreed very well with literature value¹⁶, which suggested the formation of a complete monolayer. The monolayer is chemically inert, mechanically stable, and resistant to oxidation in the air to 200°C . The functionalized mask was successfully used over 60 times without the need to reapply the release layer, which testifies to its stability.

Conformal contact was a much more challenging issue to address. There are several obstacles to overcome in order to ensure making good contact: 1) dust particles on the mask or the substrate; 2) uniform pressure distribution across the entire area of contact; and 3) air bubbles trapped between the mask and the substrate. The substrate that will become the Pt nanowire model catalyst was coated with an oxide layer (silica and alumina) through electron beam evaporation as described earlier. This oxide-covered wafer is then coated with 15 K PMMA to serve as the imprint resist. The functionalized mask was brought into contact with the catalyst substrate in a class 100 clean room in the Microlab to ensure contact. To ensure uniform pressure, the two stainless steel surfaces in contact with the mask and the substrate were polished to the best finish possible (measure of smoothness). In addition, two silicon rubber patches were placed between

the press and the support to aid in the pressure distribution uniformity. Air bubble can be removed with a simple vacuum pump. The pressure was applied through a hydraulic press; a band heater around the stainless steel cylinder provided the heat. The system can exert a maximum force of 4 tons, with heating capabilities in static air up to 300°C (Figure 7.10).

After the mask had been rinsed in acetone in a clean room to remove dust particles, and after dry nitrogen had been blown over the mask and the substrate prior to clamping, the samples were then placed into the press. The mold and substrate were heated at a rate of 0.5°C/s with the vacuum pump turned on. Upon reaching 128°C, a pressure of 272 atm is applied for 5 min with continued heating and pumping. After 5 min, the heat and vacuum are turned off and a flow of air is turned on to cool the two objects. When the temperature cools to around room temperature, the mold and substrate are manually separated.

The mask and imprinted samples were characterized with SEM and AFM. PMMA is a radiation-sensitive polymer and melts under intense electron beam irradiation; therefore, high-resolution measurements from SEM will broaden the real dimensions (Figure 7.11). Figure 7.12 shows AFM images of both the mask and the PMMA film after nanoimprint lithography. The smallest dimension on the mask is about 20 nm; the height of the feature is about 80 nm. The imprinted PMMA faithfully reproduced all the features from the mask. All the dimensions on both images are exaggerated due to tip-sample convolution. The imprint quality of the samples is affected by the temperature, PMMA film thickness, and pressure applied. The thickness of the PMMA film is the most critical concern. Experiments with different PMMA thicknesses

show that the thinner the film, the poorer the quality of the imprint, with 150 nm being the division line between a thick and thin film. This behavior is related to the instability of thin films under thermal treatment, which has the tendency to de-wet the surface and form irregular structures. Thicker films are more stable in the thermal treatment. Temperature is also a big factor; with the PMMA glass transition temperature of 120°C, any temperature lower than that would result in little pattern transfer. However, too high a temperature will de-wet even a thick polymer film. Empirical results showed that any temperature above 160°C is considered high; the optimal temperature was 140°C. The pressure is not a strong factor in influencing the imprint quality. The pressure commonly used was 100 atm.

The resulting substrate has the negative impression of the mold; however, a residual polymer layer (60-80 nm) is present at the bottom of the imprinted channels. Before metal evaporation, the oxide or wafer must be exposed. Therefore, this residual polymer layer must be etched away. Oxygen plasma etching was performed with a Lam Research 9400 TCP etcher in the reactive ion-etching mode. The conditions for the oxygen plasma etching were 10 mTorr pressure, 100 sccm O₂ flow, top RF power of 100 W, bottom RF power of 25 W, and an etch time of 20 s. The average etch rate was ~80 Å/s, and the average bias was ~-95V. The etching rate for 15 K PMMA is proportional to the power on the top electrode, as shown in Figure 7.13. A low etching rate is desired for better process control. From Figure 7.13, it seems natural to simply decrease the top electrode power. However, decreasing the top electrode power also destabilizes the plasma, which makes the etching rate control difficult. The minimum power needed to sustain stable O₂ plasma was experimentally determined to be 100 W. Because feature

broadening is seen during the oxygen plasma etch of the residual PMMA, 45° shadow deposition of SiO₂ is utilized to shrink the size of the hole that the metal will pass through during the line-of-sight electron beam evaporation (Figure 7.14). Feature broadening is the result of the poor etch resistance of the PMMA. The main etchant for removing PMMA is the oxygen radical. Radicals reach the PMMA surface by diffusion. While the radicals react with the bottom PMMA much faster due to ion-assisted chemical reactions, they do attack the sidewalls of the PMMA structure as well (Figure 7.15). To minimize the effect of plasma related feature broadening, lower pressures, lower etching rates, and lower temperatures are desired. The shadow deposition process is an indirect solution to the problem. The conditions of the optimized shadow deposition were 45°, 5×10⁻⁶ torr SiO₂, deposition rate of ~1 Å /s, total of 150 Å deposited. The substrate was then rotated 180° and the above conditions were repeated to put down another 150 Å of silica. With this protected substrate, Pt was then deposited via electron beam evaporation.

7.2.3 Reaction Rate Studies for Poisoned and Unpoisoned Ethylene Hydrogenation over Alumina-Supported Pt Nanowires

The kinetics and surface science chamber has been described in previous chapters. The same cleaning procedure utilized for the Pt nanoparticles was employed for the Pt nanowires. For unpoisoned ethylene hydrogenation, the reaction conditions were 10 Torr C₂H₄, 100 Torr H₂, and a temperature range of 40°C to 100°C. For the poisoned reaction, the reaction conditions were 0.3 Torr CO, 10 Torr C₂H₄, 100 Torr H₂, and a temperature range of 130°C -250°C. The products were monitored via a GC as described in previous chapters.

7.3 Results and Discussion

7.3.1 Characterization of Alumina-Supported Pt Nanowires Fabricated by SRL and NIL

After metal deposition and liftoff procedures as described earlier, alumina-supported (and silica-supported) Pt nanowires remained with dimensions of 10 μm in length, (22 ± 2) nm in width, and 15 nm in height. These samples were characterized with AFM (Figure 7.16) and SEM (Figure 7.17). XPS results confirmed the Pt nanowires to be on a layer of alumina. The patterned surface area is $\sim 0.3 \text{ cm}^2$ over the 10 cm^2 surface, thus yielding the necessary active metal surface area for catalytic reactions.

7.3.2 Reaction Rate Studies for Poisoned and Unpoisoned Ethylene Hydrogenation on the Alumina-Supported Pt Nanowires

The measured activation energy for the Pt nanowires was $13.6 \pm 0.2 \text{ kcal/mol}$ (Figure 7.18). The unpoisoned activation energy is slightly higher than the values seen on the Pt(111) single crystal and the Pt nanoparticles ($\sim 10 \text{ kcal/mol}$). This is because of the formation of other species: mostly methane, but at elevated temperatures, some propane. These species are the result of carbon fragments (C_1 , C_2 , and C_3) that are left on the surface of the metal after our novel NO_2 cleaning method. The cleaning method that was deemed successful for cleaning the single crystal and nanoparticle samples was insufficient and incomplete for the nanowires. Because all of the carbon fragments do not get burned off before the reaction takes place, these species can easily pick up some of the dissociated hydrogen on the surface during the reaction and then desorb from the

surface and get detected. The levels of detection from run to run vary, which indicates that they are not the products of a steady reaction, where the levels would linearly increase over time in our batch reactor. Another factor that dissuades the notion of a secondary reaction pathway (ethane hydrogenolysis) is that this reaction does not turnover at such a low temperature regime. There is also not a proportionality between the ethane produced from ethylene hydrogenation and the methane produced via these carbon fragments. This indicates that one reaction is not taking products from the other reaction in a competition-type manner. Nonetheless, there are other species on the surface which, much like CO, serve to take away adsorption sites and reduce mobility of the reactants of interest (ethylene and hydrogen). Accordingly, the energy barrier becomes greater to overcome. It is not as severe as the CO-poisoning, where all CO must be completely removed from the metal's active sites before the reaction can take place.

The measured apparent activation energy for the poisoned reaction was (21.3 ± 0.2) kcal/mol (Figure 7.19). As a comparison, the poisoned and unpoisoned activation energies over the Pt nanowires are shown in Figure 7.20. The activation energy for the CO-poisoned ethylene hydrogenation falls in line with the Pt(111) data, where we are essentially seeing the desorption energy of CO. But by having this 3rd model system to study, it does clarify the results seen for the Pt nanoparticles.

Two things happen with the CO-poisoning on the Pt(111) single crystal. One is that the turnover rate is dramatically reduced. In other words, less product (ethane) per run is produced overall during the course of the experiment. The other result is a doubling of the activation energy. This is the result of CO preferentially binding to the metal surface, which serves to block available sites for the reactants to adsorb as well as

prevent the mobility of these species on the metal surface. Mobility is absolutely crucial in catalysis. So if the CO goes in and covers the surface, molecular hydrogen cannot adsorb on the metal surface and dissociate into H atoms and move around on the surface. Similarly, the ethylene cannot loosely (π -bond and di- σ bond) bind to the metal surface and move around in order to pick up hydrogen and step-wise hydrogenate into ethane and then desorb from the metal surface to be detected by gas chromatography. The reaction cannot turnover unless it is on the metal surface. The result of this is an increase in activation energy. In other words, the system must overcome a larger energy barrier before the reaction will proceed. Because the CO poisons the reaction, we must increase the energy of the system in order to remove the CO and allow for hydrogen and ethylene to react. The added energy in the system is seen in the temperature range studied. For unpoisoned ethylene hydrogenation, we look at the turnover rate from 100°C-200°C. For the poisoned reaction, we probe the reaction from 130°C-250°C. Even at the highest temperature during the poisoned reaction, the turnover is very small compared to the lowest temperature unpoisoned turnover number. The fact that the activation energy is ~20 kcal/mol tells us that the reaction will not turnover until the CO is removed from the surface. That value is within the range for the desorption energy of CO. As soon as the CO is removed and the reactant gases can bind to the surface and move around, the reaction proceeds and we detect product (ethane).

For the Pt nanoparticles, the unpoisoned activation energy is ~10 kcal/mol, and is in excellent agreement with Pt(111) data. The CO-poisoned reaction data, however, tells us an interesting story. Whereas the single crystal and nanowires show two results from poisoning by CO (reduction in turnover rate and increase in activation energy), the

nanoparticles only show the reduction in turnover rate. The activation energy rises only slightly (unpoisoned ~ 10 kcal/mol to poisoned ~ 11 kcal/mol). The explanation of this comes from having the empirical data from the single crystal and nanoparticles as a comparison. It is not just the presence of these metal-oxide interface sites, but the ratio of metal sites to interface sites that seem to ultimately tune the catalyst for a reaction. It is believed that these interface sites remain active for the reaction in the presence of CO. With the nanowires, the metal sites to interface sites ratio is ~ 20 ; on the nanoparticles, the metal sites to interface sites ratio is ~ 300 . This order of magnitude difference may be the key to attaining the selectivity that is desired. With the nanowires, the number of interface sites is too close to the number of metal sites. The closer to unity, the better CO can poison the sites. The ability to test this theory, however, resides with the nanowires. We have complete control in the fabrication process of the nanowires such that we can manipulate this ratio of metal-to-interface sites. This is accomplished by fabricating nanowires that are taller/shorter or thinner/wider. All of these serve to affect the number of metal sites. A comparison chart that summarizes the results for the Pt(111) single crystal, alumina-supported Pt nanoparticles, and alumina-supported Pt nanowires is shown in Table 7.1. Similar results were seen for Pt nanowires supported on different oxides (silica vs. alumina) as well as Pt nanowires of different diameters/linewidths (22 nm vs. 25 nm vs. 64 nm). The sample fabrication and treatment for all of these Pt nanowire arrays were identical. The same characterization techniques were utilized to confirm the composition and dimensions of these systems. Table 7.2 summarizes the results for these different Pt nanowire samples. The fact that no meaningful differences were seen for the poisoned and unpoisoned ethylene hydrogenation reaction over the Pt

nanowire samples showed that there were no significant contributions from the support or from the size of the wires in the size regime probed (22-64 nm). Size effects should dominate the reaction data when the diameter or linewidth of the Pt nanowires is sub-10 nm. The ratio value of metal-to-interface sites is roughly the same for all nanowire samples. Therefore the theory of controlling this ratio value is still supported by the empirical catalytic data. The results also follow the trend of surface area estimations from geometry of the samples. The single crystal has cm^2 surface area, while the nanoparticle array and all of the nanowire arrays have surface areas on the order of mm^2 .

7.4 Conclusion

A photolithography-based process has been developed to produce silicon nanowire arrays on silicon wafers. By combining the conformal deposition and anisotropic etching processes, 20-nm silicon nanowire arrays can be routinely produced. Oxidation and HF trimming further reduces the structure size into the interesting catalytic size regime (sub-10 nm). By using photolithography techniques, size reduction lithography permits us to make 10 nm spatial features starting from the 600 nm range, achieving more than an order of magnitude reduction. Nanoimprint lithography was demonstrated with a home built apparatus. The procedures and conditions for mask surface release functionalization, nanoimprint lithography, and oxygen plasma etching have been established. 22-nm Pt nanowires supported on Al_2O_3 have been fabricated, with enough surface area for further catalysis studies. Through the same procedures, 25-nm Pt nanowires on silica and 64-nm Pt nanowires on alumina were also fabricated.

The reaction data from the Pt nanowires, in comparison with previous reaction data on the Pt(111) single crystal and Pt nanoparticles, provides the insight we are seeking in understanding catalytic activity and selectivity. By tuning the catalyst, we should be able to tune a reaction. Now that these model systems have been optimized in their fabrication and shown to be viable catalysts from their reaction data, systematic investigations of hydrocarbon conversion reactions must be performed. By building up this empirical database, a recipe can be generated for selecting the desired reaction pathway (selectivity) of more industrially significant reactions, such as *n*-hexane reforming.

Table 7.1. Comparison chart of kinetic parameters for unpoisoned and poisoned ethylene hydrogenation reaction over Pt(111) single crystal, alumina-supported Pt nanoparticles, and alumina-supported Pt nanowires. The number of metal sites, interface sites, and the ratio of these two numbers are also listed. It is this ratio of metal-to-interface sites that control selectivity.

Pt Catalyst	Unpoisoned Ethylene Hydrogenation Activation Energy (kcal/mol)	Poisoned Ethylene Hydrogenation Activation Energy (kcal/mol)	Platinum Sites	Interface Sites	Ratio (Metal-to-Interface Sites)
Pt(111)	9.6 ± 0.4	20.2 ± 0.1	6.84×10^{14}	0	NA
Al ₂ O ₃ /Pt Nanoparticles	10.2 ± 0.2	11.4 ± 0.6	1.04×10^{14}	3.17×10^{11}	328
Al ₂ O ₃ /Pt Nanowires	13.6 ± 0.2	21.3 ± 0.2	9.21×10^{13}	3.81×10^{12}	24.2

Table 7.2. Comparison chart of kinetic parameters for unpoisoned and poisoned ethylene hydrogenation reaction over Pt nanowires of different sizes (22, 25, and 64-nm) and supports (silica and alumina). The number of metal sites, interface sites, and the ratio of these two numbers are also listed. It is this ratio of metal-to-interface sites that control selectivity.

Pt Sample (Diameter/ Spacing)	Unpoisoned Ethylene Hydrogenation Activation Energy (kcal/mol)	Poisoned Ethylene Hydrogenation Activation Energy (kcal/mol)	Platinum Sites	Interface Sites	Ratio (Metal- to- Interface Sites)
Al ₂ O ₃ /Pt Nanowires (22- nm/1200- nm)	13.6 ± 0.2	21.3 ± 0.2	9.21×10^{13}	3.81×10^{12}	24.2
SiO ₂ /Pt Nanowires (25- nm/1200- nm)	13.5 ± 0.1	22.2 ± 0.3	8.35×10^{13}	3.27×10^{12}	25.5
SiO ₂ /Pt Nanowires (64- nm/1200- nm)	13.0 ± 0.3	19.8 ± 0.3	1.43×10^{14}	3.29×10^{12}	43.5

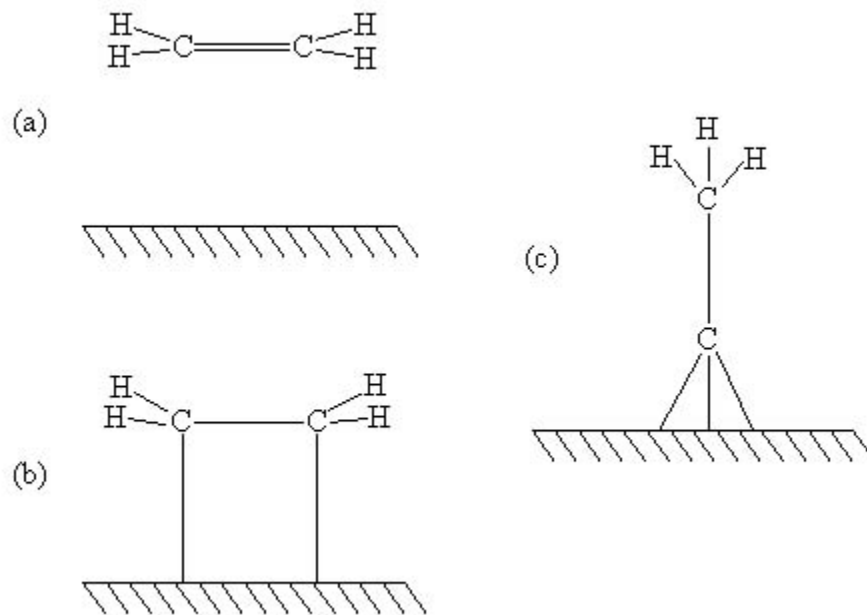


Figure 7.1. The three surface structures formed by adsorbed ethylene on Pt(111): a) π -bonded ethylene; b) di- σ -bonded ethylene; and c) ethynidyne.

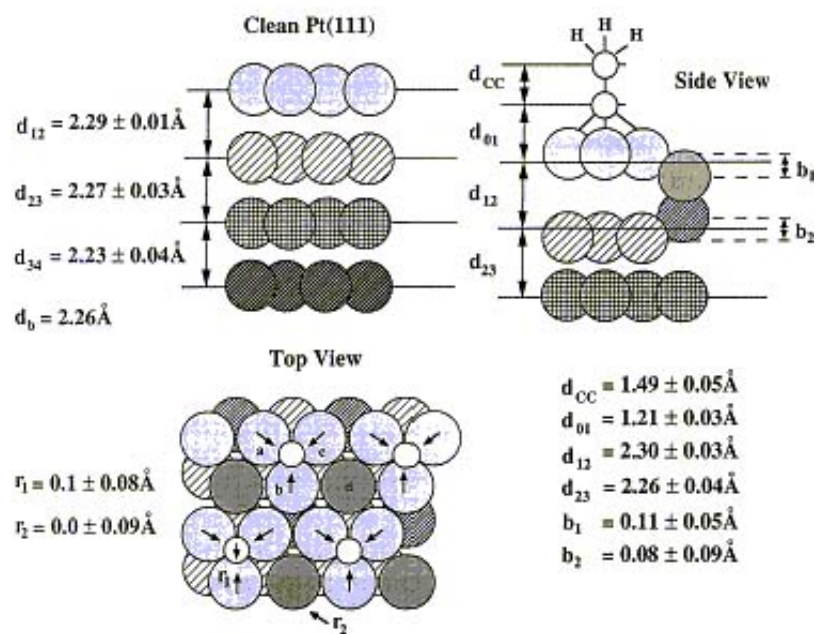


Figure 7.2. Structure of chemisorbed ethylidyne on Pt(111).

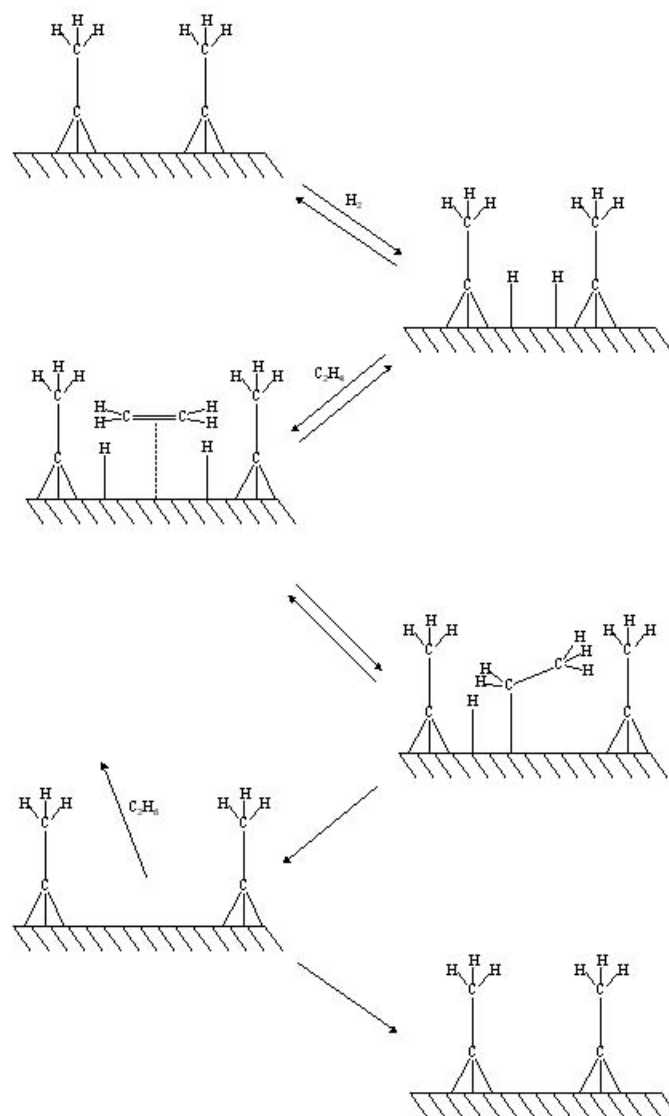


Figure 7.3. Proposed mechanism for ethylene hydrogenation on Pt(111).

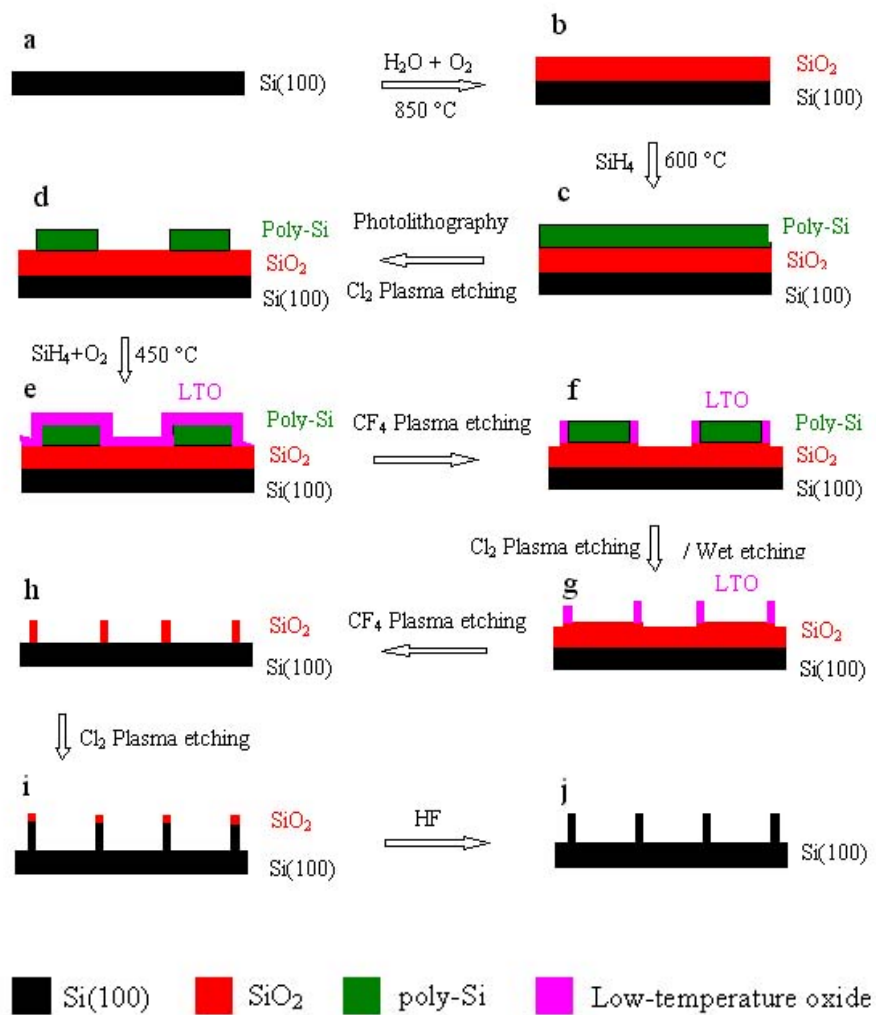


Figure 7.4. Schematic drawing of size reduction lithography process.

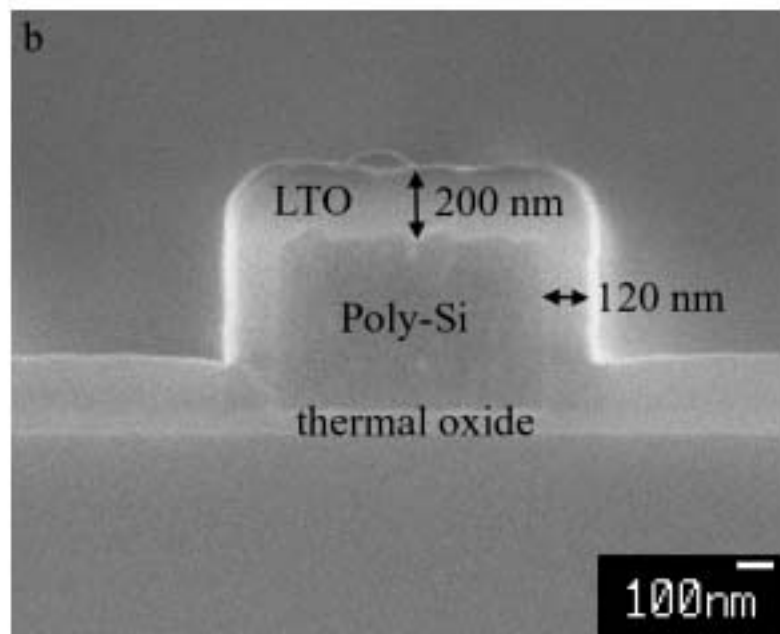
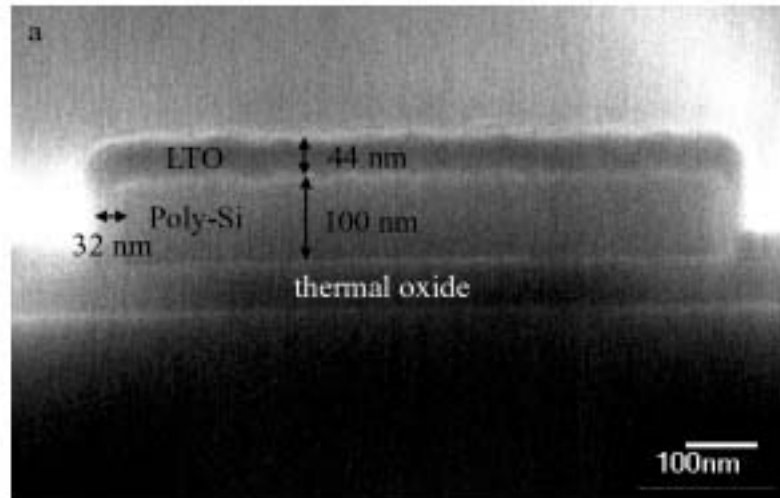


Figure 7.5

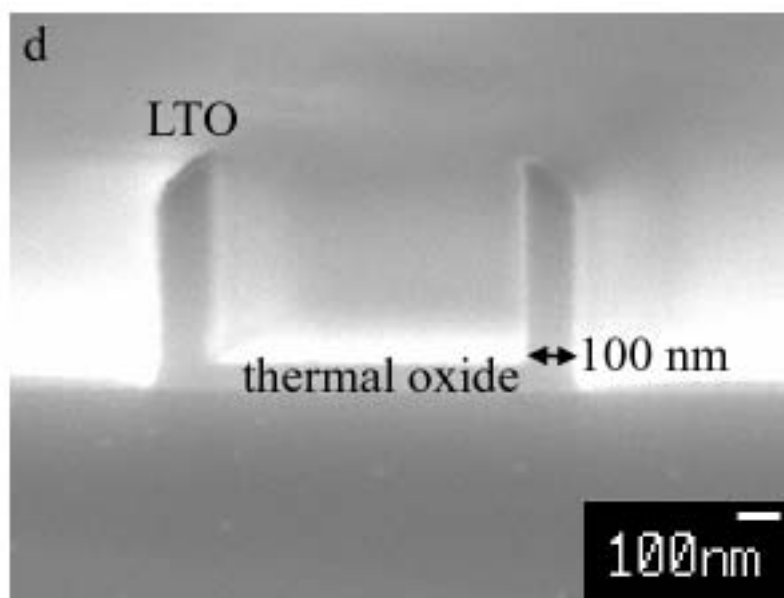
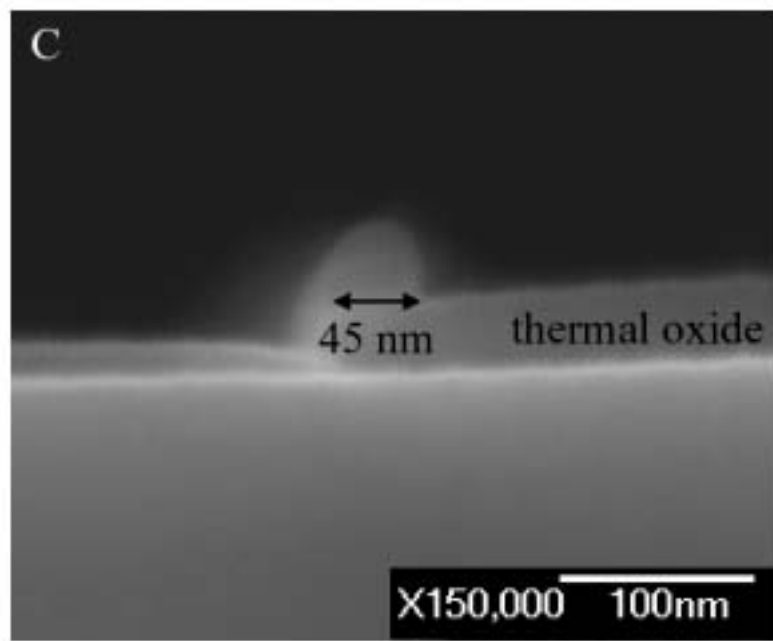


Figure 7.5. continued

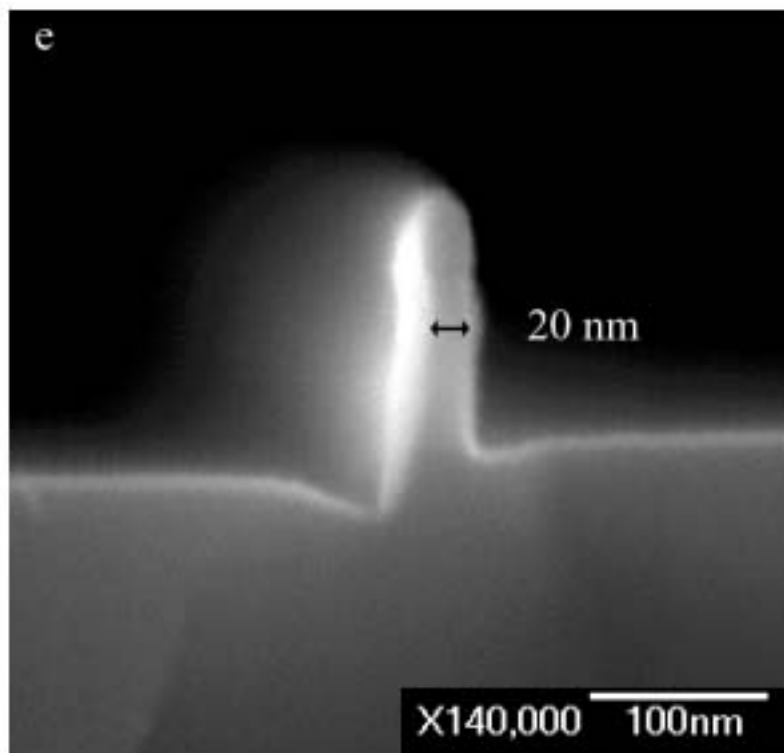


Figure 7.5 continued

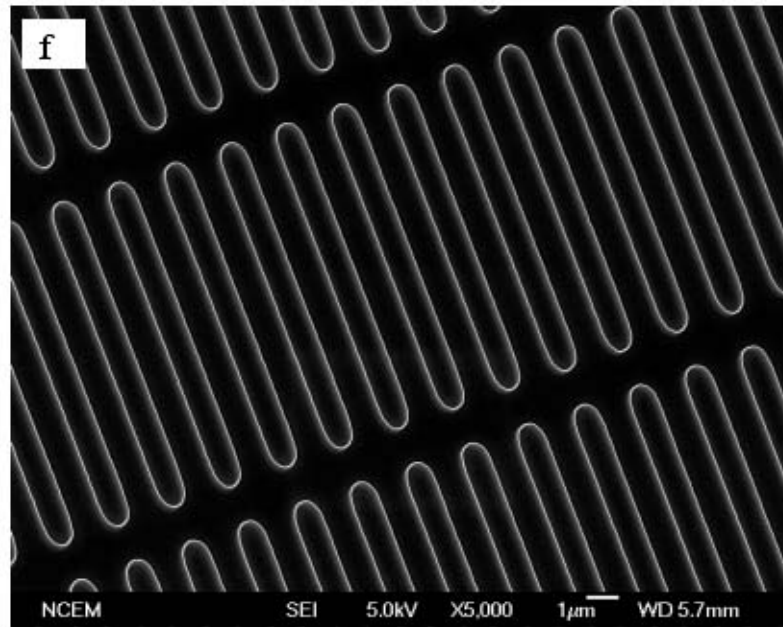


Figure 7.5. SEM characterization of the size reduction lithography process. a) Cross-sectional view after thin LTO deposition (44 nm); Cross-sectional view after thick LTO deposition (200 nm); c) Cross-sectional view after the top LTO layer and poly-Si layer have been etched away. The feature size broadens from 32 to 45 nm; d) Cross-sectional view after the top LTO layer and poly-Si layer have been etched away. There is a distinct undercut to the feature size at the bottom of the LTO hard mask; e) Cross-sectional view of 20-nm Si nanowire array; f) Top view of the 20-nm Si nanowire array.

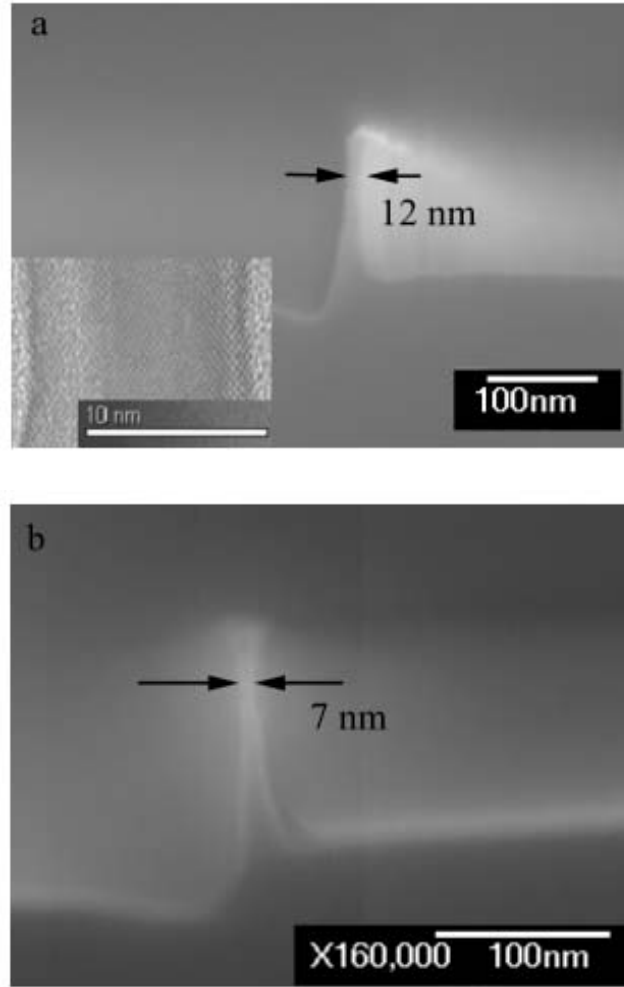


Figure 7.6. a) Cross-sectional view of 12-nm Si nanowire array made after thermal oxide trimming. The HRTEM inset image shows the single crystalline nature of the Si nanowires. b) Cross-sectional view of 7-nm Si nanowire array made after further thermal oxide trimming.

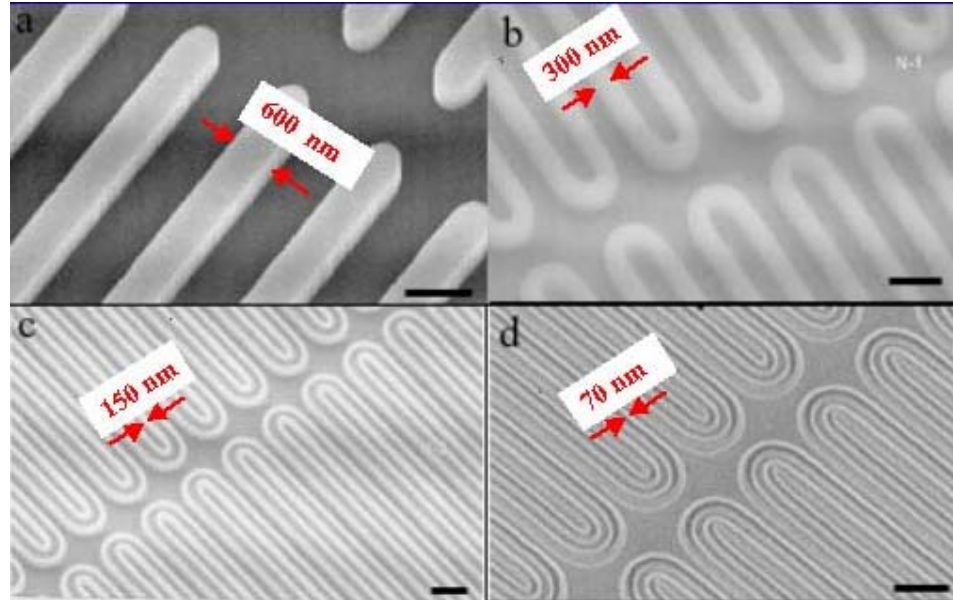


Figure 7.7. Pattern density increase by multiple size reduction lithography. a) after patterning sacrificial poly-Si layer; b) after LTO deposition, LTO spacer etch by CF_4 plasma, and removal of sacrificial poly-Si by KOH; c) after poly-Si deposition, poly-Si spacer etch by Cl_2 and HBr, and removal of LTO by HF; and d) after LTO deposition, LTO spacer etch by CF_4 plasma, and removal of sacrificial poly-Si by KOH. For an etch stop, nitride was deposited before starting size reduction lithography. $8 (=2^3)$ lines were generated from one line after 3 cycles of size reduction lithography. Linewidth was 70 nm and spacing was 80 nm in (d). The scale bars are all 1 μm .

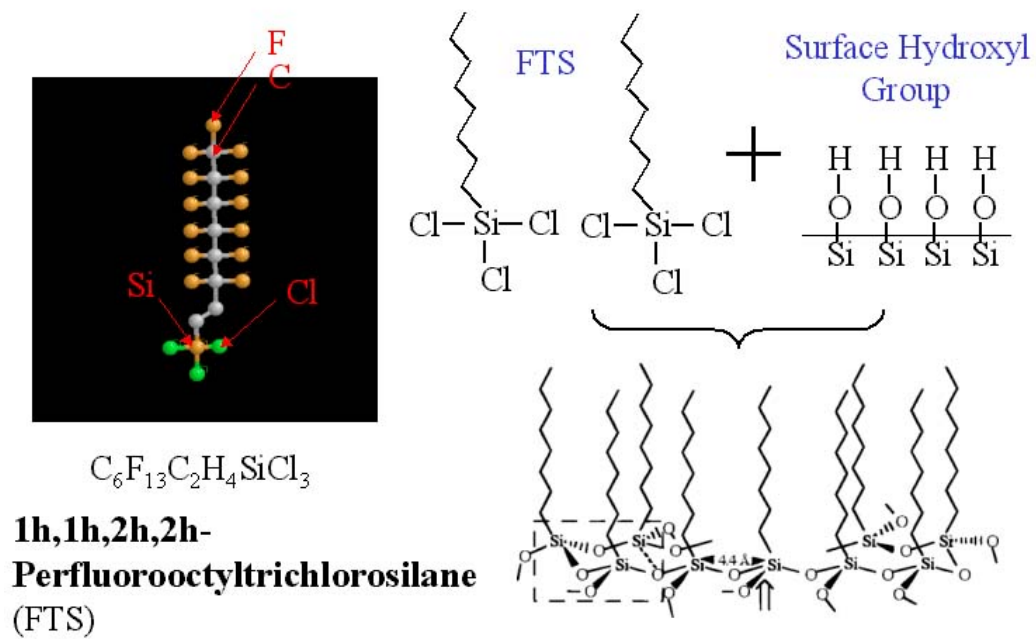


Figure 7.8. Formula and configuration of FTS molecule that is used to functionalize the surface of the Si mask to help with separation after NIL.

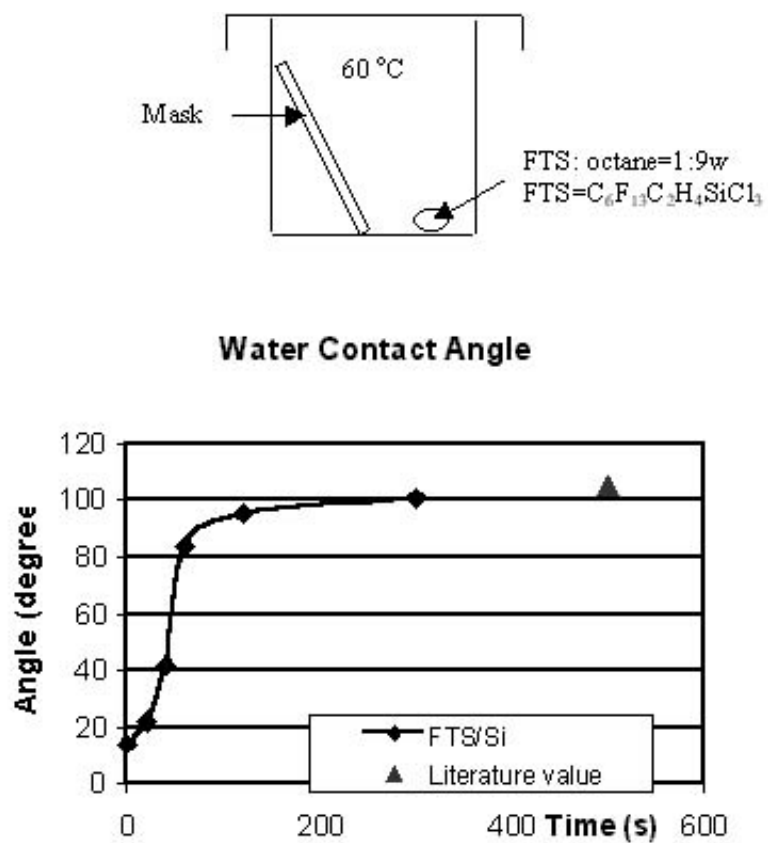


Figure 7.9. The setup for mask functionalization. Below is the water contact angle measurement on a plain Si(100) surface functionalized with FTS with time.

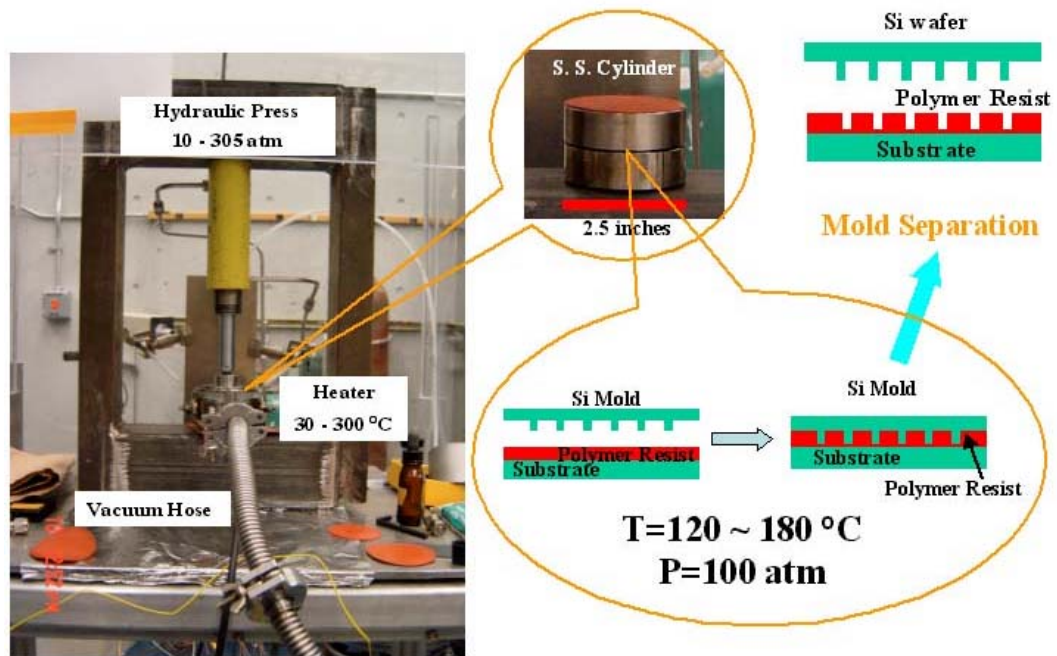


Figure 7.10. Experimental setup for NIL press.

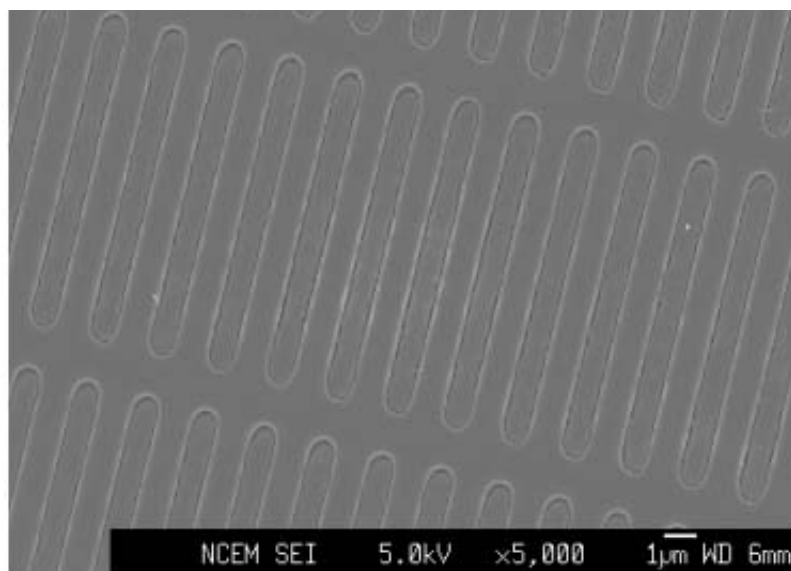


Figure 7.11. SEM of imprinted PMMA showing pattern replication from Si mold. Since the energy from the electrons in SEM can melt the PMMA, lower magnification/resolution was utilized to image the polymer pattern.

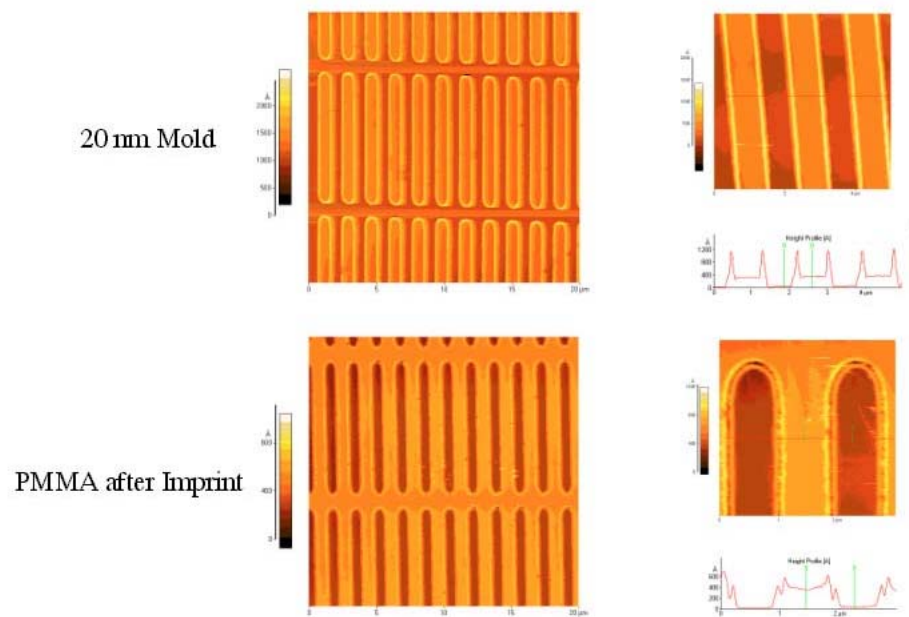


Figure 7.12. AFM images of mold and PMMA after nanoimprint lithography, showing pattern replication.

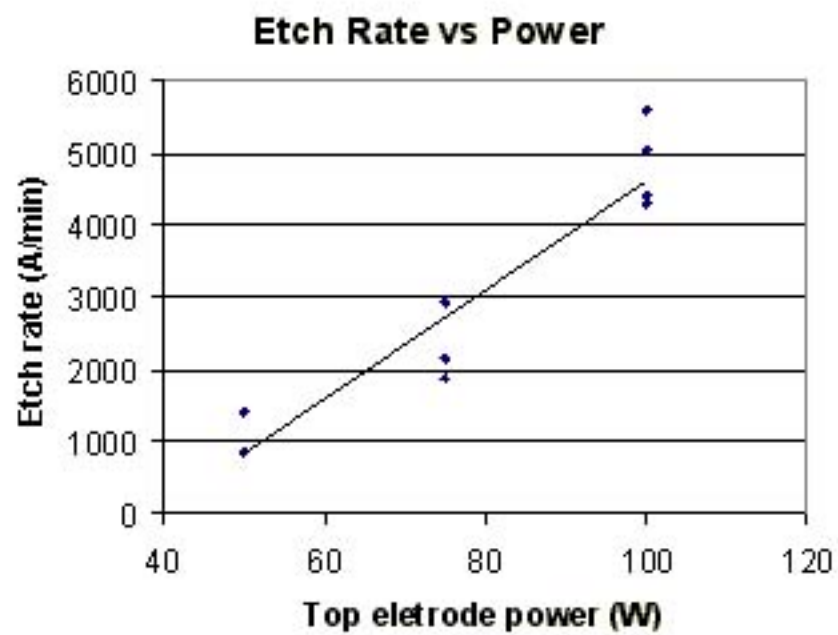


Figure 7.13. Etching rate of 15K PMMA under O₂ reactive ion etching.

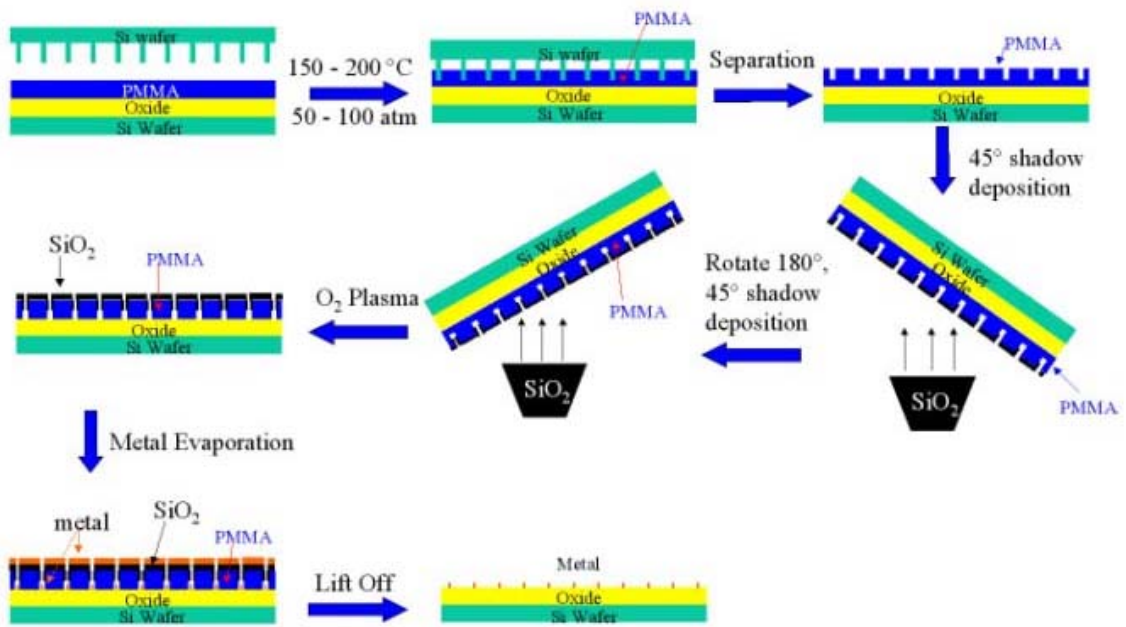


Figure 7.14. Schematic of shadow deposition process along with NIL and the evaporation of the metal. This process is used to reduce the effects of feature broadening during the residual PMMA layer etch step.

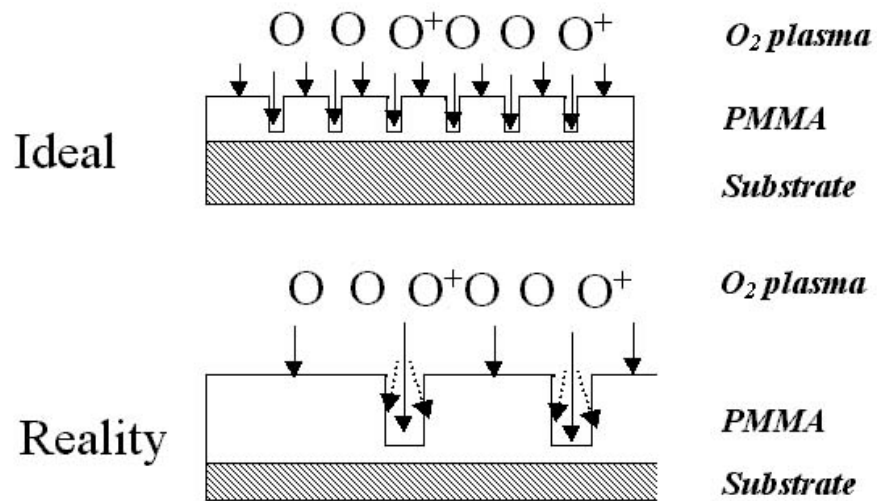


Figure 7.15. Schematic drawings to show the broadening of nanofeatures during O_2 reactive ion etching. Ideally, oxygen radicals (the main etchant for PMMA) should only etch vertically. In reality, oxygen radicals also attack the sidewalls, therefore, broadening the resultant feature.

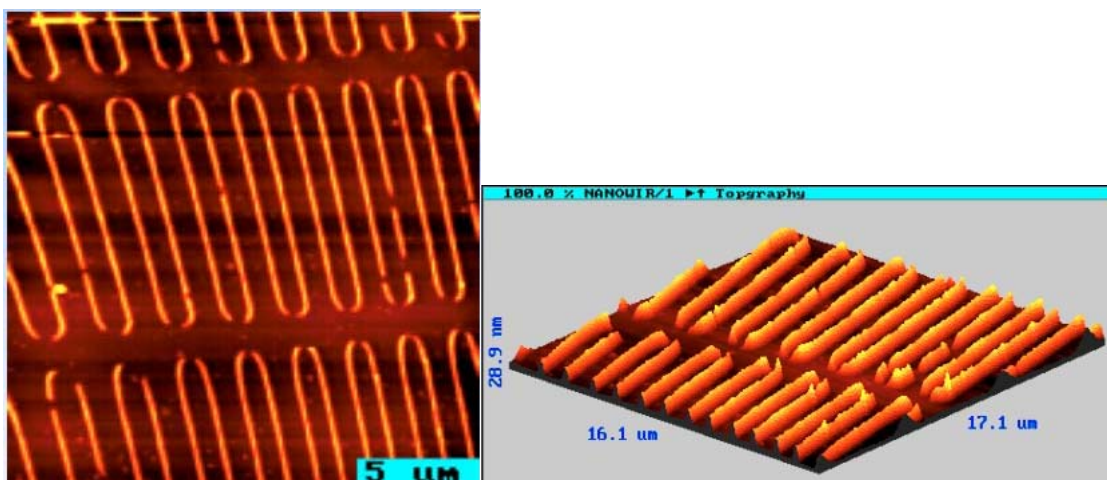


Figure 7.16. AFM images of the alumina-supported Pt nanowires with dimensions of 10 μm in length, (22 ± 2) nm in width, and 15 nm in height. a) top view; b) 3-D view.

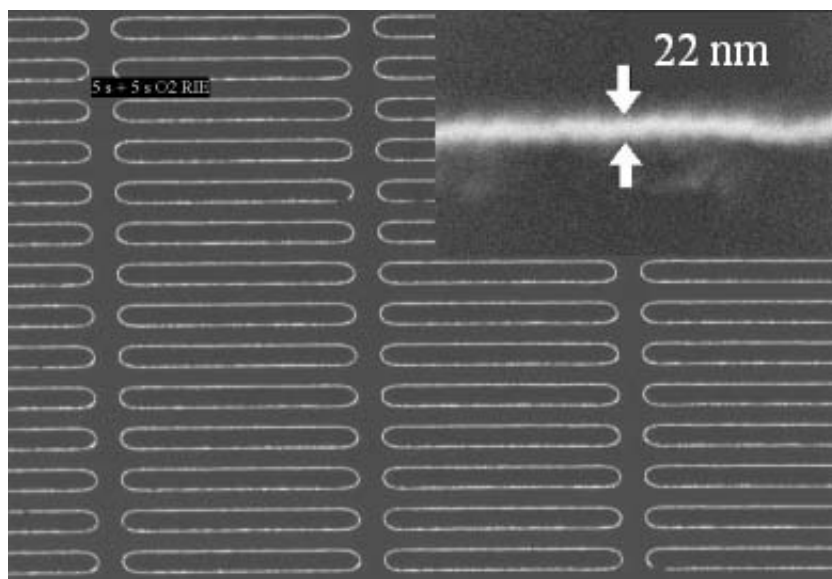


Figure 7.17. SEM image of the alumina-supported Pt nanowires with dimensions of 10 μm in length, (22 ± 2) nm in width, and 15 nm in height. The inset shows the diameter of the Pt nanowires.

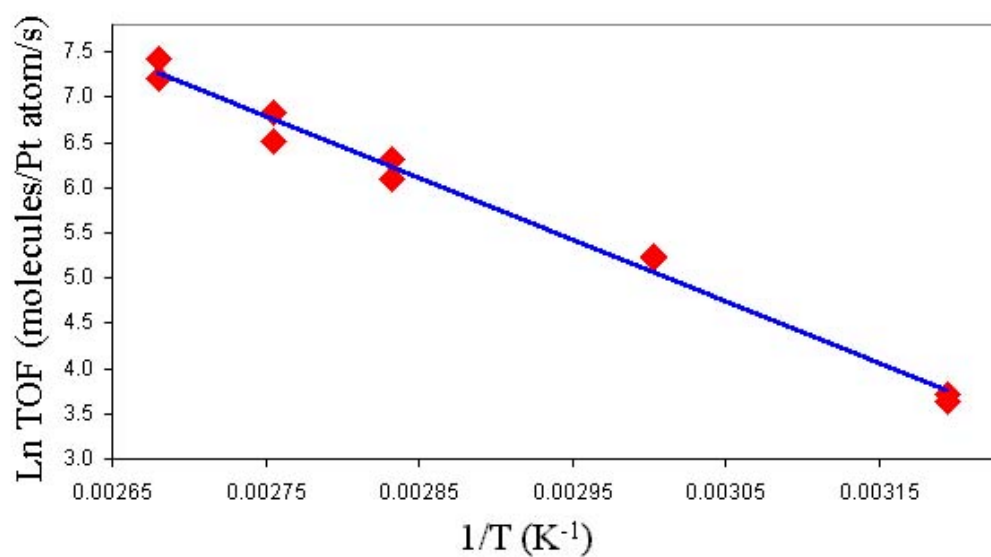


Figure 7.18. Arrhenius plot to determine the activation energy of ethylene hydrogenation over the Pt nanowire array. Reaction conditions were 10 Torr C_2H_4 , 100 Torr H_2 , and 800 Torr Ne.

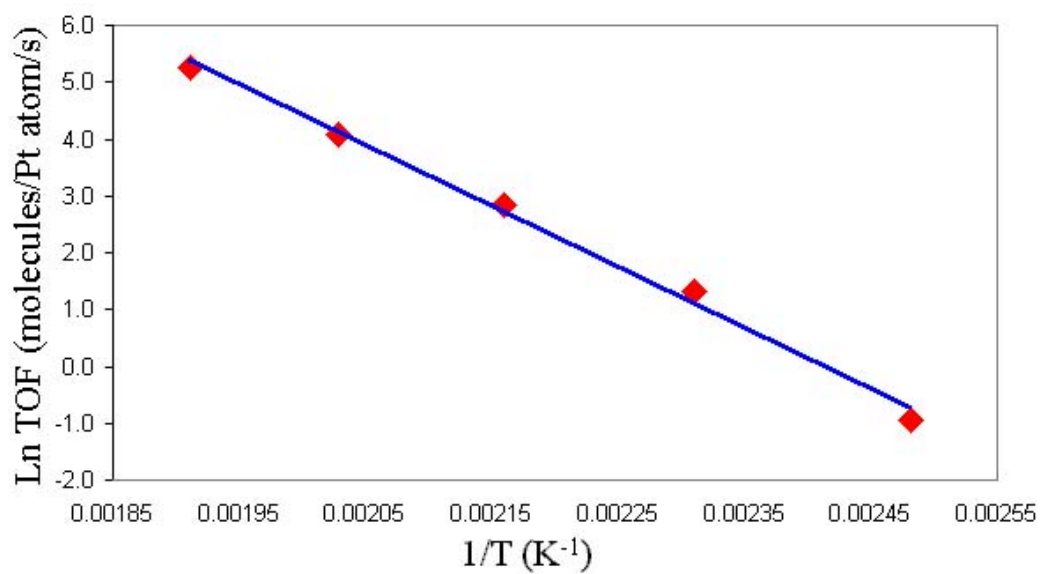


Figure 7.19. Arrhenius plot to determine the activation energy of CO-poisoned ethylene hydrogenation over the Pt nanowire array. Reaction conditions were 0.3 Torr CO, 10 Torr C₂H₄, 100 Torr H₂, and 800 Torr Ne.

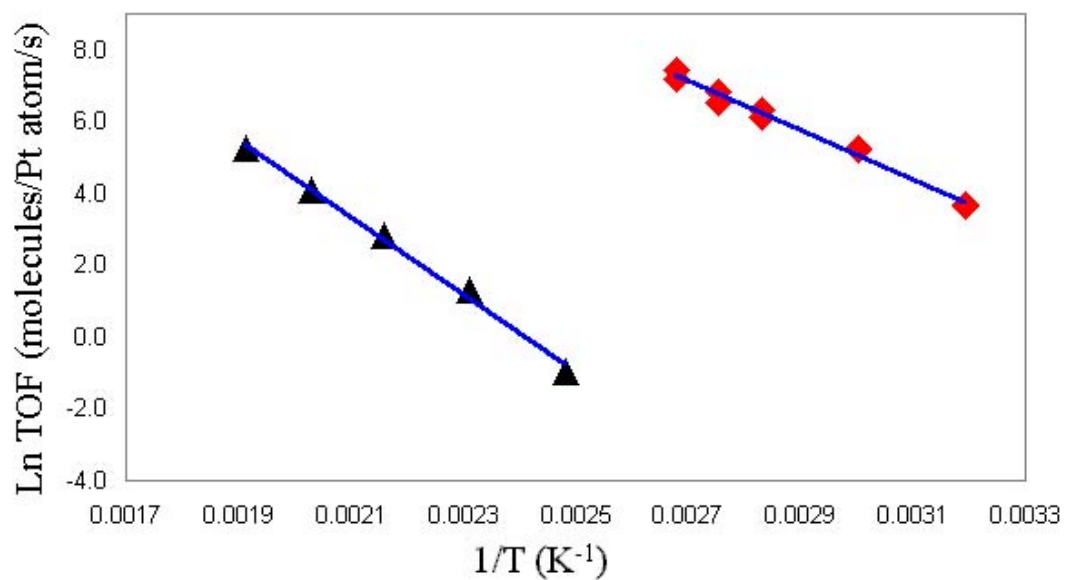


Figure 7.20. Arrhenius plots of the rate of ethylene hydrogenation vs. $1/T$ on Pt nanowire arrays with (▲) and without (◆) CO. The activation energies obtained from the slopes are (21.3 ± 0.2) and (13.6 ± 0.2) kcal/mol with and without CO present, respectively. Reaction conditions were 10 Torr C_2H_4 and 100 Torr H_2 .

References

-
- ¹ For a review, see: Horiuti, J.; Miyahara, K. *Hydrogenation of Ethylene on Metallic Catalysts*, National Standard Reference Data System-National Bureau of Standards (NSRDS-NBS), **1968**, 13.
- ² Polanyi, M.; Horiuti, J. *Trans. Faraday Soc.* **1934**, 30, 1164.
- ³ Cremer, P.S.; Su, X.C.; Shen, Y.R.; Somorjai, G.A. *J. Am. Chem. Soc.* **1996**, 118, 2942.
- ⁴ Doll, R.; Gerken, C.A.; Van Hove, M.A.; Somorjai, G.A. *Surf. Sci.* **1997**, 374, 151.
- ⁵ Cremer, P.S.; Stanners, C.; Niemantsverdriet, J.W.; Shen, Y.R.; Somorjai, G.A. *Surf. Sci.* **1995**, 328, 111.
- ⁶ Starke, U.; Barbieri, A.; Materer, N.; Van Hove, M.A.; Somorjai, G.A. *Surf. Sci.* **1993**, 286, 1.
- ⁷ Wander, A.; Van Hove, M.A.; Somorjai, G.A. *Phys. Rev. Lett.* **1991**, 67, 626.
- ⁸ Land, T.A.; Michely, T.; Behm, R.J.; Hemminger, J.C.; Comsa, G. *J. Chem. Phys.* **1992**, 97, 6774.
- ⁹ Nomikou, Z.; Van Hove, M.A.; Somorjai, G.A. *Langmuir* **1996**, 12, 1251.
- ¹⁰ Van Hove, M.A.; Somorjai, G.A. *J. Mol. Catal. A-Chem.* **1998**, 131, 243.
- ¹¹ Ge, Q.; King, D.A. *J. Chem. Phys.* **1999**, 110, 4699.
- ¹² Zaera, F.; Somorjai, G.A. *J. Am. Chem. Soc.* **1984**, 106, 2288.
- ¹³ Ellison, P.; Feinberg, M.; Yue, M.H. Saltsburg, H. *J. Mol. Catal. A-Chem.* **2000**, 154, 169.
- ¹⁴ Kao, D.B.; McVittie, J.P.; Nix, W.D.; Saraswat, K.C. *IEEE Trans. Electron Devices* **1987**, 34, 1008.

¹⁵ Kao, D.B.; McVittie, J.P.; Nix, W.D.; Saraswat, K.C. *IEEE Trans. Electron Devices* **1988**, 35, 25.

¹⁶ Ulman, A. *Chem. Rev.* **1996**, 96, 1536.